Simultaneous Multislice Functional Magnetic Resonance Imaging

by

Alan Chu

A dissertation submitted in partial fulfillment
of the requirements for the degree of
Doctor of Philosophy
(Biomedical Engineering)
in the University of Michigan
2016

Doctoral Committee:

Professor Douglas C. Noll, Chair
Professor Jeffrey A. Fessler
Assistant Research Scientist Jon-Fredrik Nielsen
Associate Research Scientist Scott J. Peltier

2016

Acknowledgments

First and foremost, I'd like to thank Doug Noll for accepting me as a student and providing many years of help and guidance. He has incredible intuition in medical imaging, which translates to great teaching and clear explanations of very complex concepts. I was extremely fortunate to be able to learn from him. From a non-scientific standpoint, he also has exceeded all expectations I've had for a great mentor; even though he has accomplished so much in the medical imaging world, he understands the importance of a good work-life balance. Although busy, he makes it a priority to meet with his students and is always friendly and passionate about our work. In addition, he has been incredibly supportive of my clinical medicine pursuits.

I'd also like to thank the rest of my committee for helping me with research throughout the years. Jeff Fessler has been amazing in helping me understand image reconstruction better, and I was lucky to be able to learn from such an expert in the field. When I first joined the lab, Jon Nielsen was the one who taught me pulse sequence development on our scanner and has continued to provide great expertise in various different areas in MRI over the years. Scott Peltier has also provided tremendous help to me; he was the one I always went to in order to ensure my subject scans were done properly and if any scanner issues came up.

My fellow U of M fMRI Lab members, both past and present, also deserve a huge thanks for answering all the questions I asked them, and making imaging research more fun. Luis Hernandez-Garcia was always great for bouncing ideas off of, and his great sense of humor always brightens my day. Daehyun Yoon, Hesam Jahanian, and Yoon Chung Kim were the senior students when I first started out in

the lab and helped me tremendously when I was first learning the basics of MRI. I was also lucky to learn from someone as smart and incredibly productive as Feng Zhao. Matt Muckley definitely made lab life more fun. I can always count on him to provide great conversation on a wide array of topics such as beer, world history, and image reconstruction, just to name a few. Hao Sun is another super smart and productive member of our lab, and I learned a lot from him. The rest of the lab, including Kathleen Ropella, Sydney Williams, and Tianrui Luo, has also been a pleasure to work with. I'd also like to thank members of Jeff's lab: Mai Le, whom I had great times with during EECS 556, Gopal Nataraj, and Dan Weller.

Finally, I'd like to thank my family for their support and encouragement. My sister Alina always believes in me no matter what the odds are of success. Pete taught me what the important things are in life and made every day a better one with his good nature, loyalty, and infinite patience. I'll always miss him. Last but definitely not least, I thank my parents, Jason and Kathy Chu, for supporting me throughout my life. This work would not have been possible without their unwavering love and guidance. Any success I've had or will have in the future is because of them.

TABLE OF CONTENTS

LIST OF FIGURES

LIST OF TABLES

ABSTRACT

Simultaneous Multislice Functional Magnetic Resonance Imaging

by

Alan Chu

Chair: Douglas C. Noll

Functional magnetic resonance imaging (fMRI) is a valuable tool for mapping brain activity in many fields. Since functional activity is determined by temporal signal changes, undesired fluctuations from physiological motion are problematic. Simultaneous multislice (SMS) imaging can alleviate these issues by accelerating image acquisition, increasing the temporal resolution. Furthermore, some applications require a temporal resolution higher than what conventional fMRI will allow. Current research in SMS has focused on Cartesian readouts due to their ease in analysis and reconstruction. However, non-Cartesian readouts such as spirals have shorter readout times and better signal recovery.

This work explores the acquisition and reconstruction of both spiral and concentric ring readouts in parallel SMS. The concentric ring readout retains most of the benefits of spirals, but also increases the usability of alternative reconstruction techniques for non-Cartesian SMS such as generalized autocalibrating partially parallel acquisitions (GRAPPA). To date, non-Cartesian SMS imaging has only been reconstructed with sensitivity encoding (SENSE), but results in this work indicate GRAPPA-based

reconstructions have reduced root-mean-square-error compared to SENSE and good subjective image quality as well. Furthermore, using point spread function analysis, the concentric ring trajectory is found to have superior slice separation properties compared to a spiral one.

Since parallel imaging greatly magnifies the amount of data used for reconstruction, a novel coil compression method is developed, which outperforms conventional coil compression in fMRI, substantially decreasing the amount of reconstruction time needed for sufficient detection of functional activation. Results indicate that the proposed method can compress 3 simultaneous slice data using a 32-channel coil down to only 10 virtual coils without any adverse effects in functional activation, noise, or image artifacts. Competing methods require substantially more coils for preservation of the data, resulting in large reconstruction time savings for the proposed method.

This work also explores the use of Hadamard-encoded fMRI for increased temporal resolution. Because Hadamard-encoded SMS uses data from multiple time frames to separate slices, physiological noise correction is critical. However, even with physiological noise correction, results indicate Hadamard-encoded fMRI is not as reliable as conventional fMRI due to undesired temporal fluctuations, most notably from uncorrected physiological noise.

CHAPTER 1

Introduction

Functional magnetic resonance imaging (fMRI) has become the prevailing method for non-invasively mapping human brain activity. The technology is widely used in neuroscience and psychology to evaluate models of cognition and in clinical medicine to develop biomarkers for neurological and psychiatric diseases. In neurosurgery, fMRI has been increasingly used to help identify critical brain regions in patients prior to brain tumor or seizure foci resection.

In fMRI, standard clinical magnetic resonance imaging (MRI) scanners are used to repetitively acquire images of the brain over an interval of time lasting several minutes. These images track small changes in the brain that correlate with a stimulus or task the subject is instructed to perform during the scan. The majority of fMRI scans use blood oxygenation level dependent (BOLD) contrast, which uses the content of deoxyhemoglobin in the blood as the contrast agent [1]. As the subject performs the task or is exposed to the stimulus, active regions of the brain will have increased blood flow [2, 3], which decreases the concentration of deoxygenated hemoglobin in that region [4]. Deoxygenated hemoglobin causes transverse dephasing in the signal relative to oxygenated hemoglobin, so a decrease in deoxygenated hemoglobin results in decreased dephasing and an increased signal intensity. In other words, increased blood flow to active brain regions causes a decrease in deoxygenated hemoglobin, which changes the magnetic susceptibility of the blood, leading to a signal intensity change in the resulting images [5, 6, 7].

Since functional activity in fMRI is determined by temporal changes in the signal, cardiac pulsations and respiratory motion can corrupt the resulting functional activity maps because they also cause significant temporal fluctuations in the acquired fMRI signal [8, 9, 10, 11, 12]. In a typical fMRI scan, one whole-brain volume is acquired in approximately 2 seconds, resulting in a frame rate of around 0.5 Hz. This sampling rate is high enough for typical task-based fMRI experiments responsible for capturing functional paradigms occurring at around 0.02 to 0.06 Hz. However, human resting heart rates are usually around 1.0 to 1.6 Hz, and the resulting noise can alias down into the frequency of interest. In addition, motion from respiration can also create noise at 0.2 to 0.3 Hz. Similar to task-based fMRI, signal fluctuations occurring at frequencies less than 0.1 Hz are of interest in resting state fMRI. However, in resting state fMRI, the paradigm waveform is not known a priori; the acquired data is itself used to determine correlations between regions of the brain. Thus, physiological noise present in the data can spuriously increase or decrease the apparent correlation between two time courses. Methods have been developed to correct for physiological noise in fMRI including post-processing methods [13, 14, 15, 16] and navigator-based methods [12, 17]. More recently, work has been done to model respiration and cardiac fluctuations by developing impulse response functions [18, 19]. Regardless of the method used, accelerated fMRI acquisitions with a higher temporal resolution can increase the effectiveness of physiological noise correction. In addition, the increase in time points provides for greater statistical power in the data [20], and more options for bulk head motion correction.

Simultaneous multislice (SMS) imaging, also called multiband imaging, is a method that can be used to accelerate fMRI by acquiring multiple slices simultaneously, thereby covering the same region as a conventional acquisition in a smaller amount of time. Because the slices are acquired simultaneously, the raw data contains overlapped or aliased images, which must be separated during the image reconstruc-

tion process.

1.1 Aims

In Chapter 2, basic principles behind MRI are introduced in order to understand how SMS imaging works and why SMS imaging is potentially an excellent technique for accelerating fMRI. Existing methods for SMS imaging are covered, including both non-parallel and parallel SMS imaging methods.

In Chapter 3, Hadamard-encoded SMS fMRI is explored. Hadamard-encoded imaging is an SMS imaging method that does not require multiple coils in order to separate the simultaneous slices. This work aims to further develop Hadamard-encoded imaging for fMRI by evaluating the temporal resolution and SNR benefits in human subject scans.

Chapter 4 investigates parallel SMS fMRI using non-Cartesian readout trajectories. Spiral parallel SMS imaging is improved by further optimizing the readout z-gradient waveform along with the k_x-k_y trajectory, by developing improved reconstruction techniques in both the image and k-space domains, and by demonstrating practical utility in fMRI studies.

In parallel SMS imaging, the amount of acquired data is multiplied by the number of receive coils used, which represents a significant increase in the computational load during reconstruction. In Chapter 5, a novel SMS coil compression method is developed to reduce the time needed for reconstruction while preserving functional activation and image quality. The method is compared with existing methods in SMS imaging as well as with conventional non-SMS imaging.

Final remarks regarding the work presented in this dissertation are included in Chapter 6, along with a description of the contributions made and potential avenues for future work.

CHAPTER 2

Background

2.1 Two-dimensional and Three-dimensional MRI

In MRI, the complex signal acquired in coil u is

$$s_u(t) = \int\int\int \Big[c_u(x,y,z) m(x,y,z) e^{-t/T_2(x,y,z)} \\ e^{-i2\pi(k_x(t)x + k_y(t)y + k_z(t)z + \Delta f_0(x,y,z)t)} \Big] \,\mathrm{d}x\,\mathrm{d}y\,\mathrm{d}z, \tag{2.1}$$

where $m(x,y,z)$ is the three-dimensional object as a function of spatial position (x,y,z), $c_u(x,y,z)$ is the sensitivity of coil u to location (x,y,z), $T_2(x,y,z)$ is the transverse relaxation time constant of the object, $\Delta f_0(x,y,z)$ is the spatially-dependent B_0 inhomogeneity, t is time, and $\boldsymbol{k}(t) = \frac{\gamma}{2\pi}\int_0^t \boldsymbol{g}(\tau)\,\mathrm{d}\tau$, where γ is the gyromagnetic ratio, and $\boldsymbol{g}(t)$ is the spatially-dependent magnetic field gradient as a function of time. For the sake of simplicity in this dissertation, we will ignore the relaxation term $e^{-t/T_2(x,y,z)}$ in Equation (2.1).

In conventional multislice imaging, a single two-dimensional slice is acquired with each excitation and no z-gradient is used during readout. Setting $k_z(t) = 0$, assuming infinitely thin slices, and arbitrarily assigning x and y to denote the in-plane dimensions, the signal equation becomes

$$s_u(t) = \int\int c_u(x,y) m(x,y) e^{-i2\pi(k_x(t)x + k_y(t)y + \Delta f_0(x,y)t)} \,\mathrm{d}x\,\mathrm{d}y \tag{2.2}$$

for two-dimensional MRI. In reality, however, slices cannot be infinitely thin, so the summation over z in Equation (2.1) still occurs. This can lead to signal loss from through-plane dephasing.

Standard fMRI typically uses a single-shot, two-dimensional approach, where individual slices are acquired sequentially to provide whole-brain coverage in approximately 2 seconds. Given a desired spatial resolution, the minimum repetition time (TR) is limited by the number of slices. Conventional parallel imaging [21, 22, 23] has been demonstrated to successfully accelerate multislice MRI scans in-plane. These methods all use multiple receive coils to allow for undersampling of k-space within each slice. However, the amount of acceleration is limited with conventional parallel imaging in fMRI because of the need for an appropriate echo time (TE) for sufficient T_2^* contrast. Three-dimensional acquisitions are another approach for acceleration in fMRI [24, 25, 26]. However, three-dimensional acquisitions require much longer readout times, which increases its vulnerability to magnetic field inhomogeneities. In addition, the readout times can stretch well beyond the TE for gray matter, depending on the desired spatial resolution and coverage.

2.2 Simultaneous Multislice MRI

Simultaneous multislice (SMS) acquisitions are yet another approach to acceleration. In SMS imaging, multiple two-dimensional slices are both excited and acquired simultaneously, and the reconstruction process is used to separate the slices and transform the data into the image domain. If l is the number of simultaneous slices with each acquisition, and again assuming infinitely thin slices, Equation (2.1) becomes

$$s_u(t) = \sum_{v=1}^{l} \int \int c_{u,v}(x,y) m_v(x,y) e^{-i2\pi(k_x(t)x + k_y(t)y + \Delta f_{0,v}(x,y)t)} \, \mathrm{d}x \, \mathrm{d}y, \tag{2.3}$$

where $m_v(x, y)$ is one simultaneous slice as a function of spatial position (x, y) and $c_{u,v}(x, y)$ is the sensitivity of coil u to simultaneous slice v. Note that SMS imaging does not necessarily require multiple receive coils. When only one coil is used, the coil index u is removed from Equation (2.3) and the coil sensitivity $c_v(x, y)$ is assumed to be 1.

The simultaneous slices are excited using a radio frequency (RF) pulse that selectively tips down spins in certain planes along one particular imaging axis, usually the z-axis by convention. Using the small-tip regime[27][28], the SMS RF pulse can be implemented as a sum of l frequency-offset, Hamming-windowed sinc functions

$$\mathrm{RF}(t) = \sum_{v=1}^{l} e^{i2\pi\tilde{f}_v t} \operatorname{sinc}(f_{\mathrm{RF}} t)[0.54 + 0.46\cos(2\pi t/T)], \tag{2.4}$$

where T is the duration of the pulse, f_{RF} is the bandwidth of the sinc, and $\tilde{f}_v$ is the frequency-offset for simultaneous slice v. The value of $\tilde{f}_v$ controls how far the simultaneous slices are from each other, and a conventional constant slice-select z-gradient with rewinder is applied during the RF pulse. Figure 2.1 shows the SMS RF pulse created for a 3 simultaneous slice acquisition.

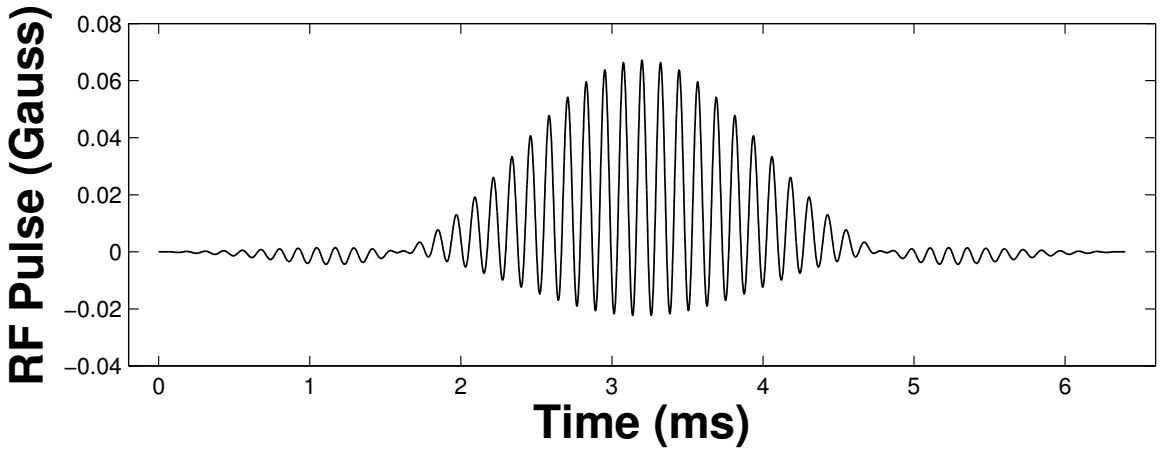

Figure 2.1: Example RF pulse for a 3 simultaneous slice acquisition created from a 6.4 ms Hamming-windowed sinc with 4 zero-crossings.

When SMS is applied to fMRI, multiple simultaneous-slice acquisitions are performed per TR to provide whole-brain coverage. Therefore, SMS imaging can be viewed as a combination of two-dimensional and three-dimensional imaging. SMS acquisitions provide an excellent avenue for acceleration in fMRI because the TE requirement does not limit the amount of acceleration as it does in conventional two-dimensional parallel imaging, and SMS does not suffer from the excessively long readout times of three-dimensional fMRI.

2.2.1 Non-parallel SMS Imaging

The earliest SMS methods did not require multiple receive coils. Souza et al. [29] developed an SMS method using Hadamard-encoded excitation as an alternative to 3-dimensional Fourier transform (3DFT) imaging. The aim was not acceleration, but to provide for more flexible slice placement over 3DFT imaging, and also to avoid the 3DFT Gibbs artifacts in the slice direction.

In Hadamard-encoded imaging of l simultaneous slices, l separate excitations are needed, each using a different RF pulse. During each excitation, the RF pulse imparts either a positive (1) or negative (-1) sign on each simultaneous slice according to a row of H_l, a Hadamard matrix of order l. For example, with an $l = 2$ simultaneous slice acquisition, $l = 2$ different RF pulses are needed to excite the slices according to the Hadamard matrix of order 2,

$$H_2 = \begin{bmatrix} 1 & 1 \\ 1 & -1 \end{bmatrix}. \tag{2.5}$$

In this case, one RF pulse would need to excite both slice 1 and slice 2 with positive signs. The equation for this RF pulse is just Equation (2.4) with $l = 2$. The other RF pulse needs to excite one slice with a positive sign and the other one with

a negative sign. The equation of this RF pulse is

$$\mathrm{RF}(t) = [e^{i2\pi\tilde{f}_1 t}\,\mathrm{sinc}(f_{\mathrm{RF}}t) - e^{i2\pi\tilde{f}_2 t}\,\mathrm{sinc}(f_{\mathrm{RF}}t)][0.54 + 0.46\cos(2\pi t/T)], \tag{2.6}$$

where slice 2 is the one with a negative sign. Therefore, one excitation gives a signal $\bar{s}_1(t) = \tilde{s}_1(t) + \tilde{s}_2(t)$, and the other excitation gives a signal $\bar{s}_2(t) = \tilde{s}_1(t) - \tilde{s}_2(t)$, where $\tilde{s}_1(t)$ is the signal from slice 1 and $\tilde{s}_2(t)$ is the signal from slice 2. Putting these together in a 2-element vector, we have

$$\begin{bmatrix} \bar{s}_1(t) \\ \bar{s}_2(t) \end{bmatrix} = \begin{bmatrix} \tilde{s}_1(t) + \tilde{s}_2(t) \\ \tilde{s}_1(t) - \tilde{s}_2(t) \end{bmatrix} = H_2 \begin{bmatrix} \tilde{s}_1(t) \\ \tilde{s}_2(t) \end{bmatrix} = \begin{bmatrix} 1 & 1 \\ 1 & -1 \end{bmatrix} \begin{bmatrix} \tilde{s}_1(t) \\ \tilde{s}_2(t) \end{bmatrix}. \tag{2.7}$$

With $l = 4$ simultaneous slices, 4 different RF pulses are used to produce 4 different excitations described by

$$\begin{bmatrix} \bar{s}_1(t) \\ \bar{s}_2(t) \\ \bar{s}_3(t) \\ \bar{s}_4(t) \end{bmatrix} = H_4 \begin{bmatrix} \tilde{s}_1(t) \\ \tilde{s}_2(t) \\ \tilde{s}_3(t) \\ \tilde{s}_4(t) \end{bmatrix} = \begin{bmatrix} 1 & 1 & 1 & 1 \\ 1 & -1 & 1 & -1 \\ 1 & 1 & -1 & -1 \\ 1 & -1 & -1 & 1 \end{bmatrix} \begin{bmatrix} \tilde{s}_1(t) \\ \tilde{s}_2(t) \\ \tilde{s}_3(t) \\ \tilde{s}_4(t) \end{bmatrix}. \tag{2.8}$$

For any Hadamard matrix, $(\frac{1}{l})H_l^* H_l = I_l$. Therefore, to separate the slices, simply perform the matrix multiplication

$$\begin{bmatrix} \tilde{s}_1(t) \\ \tilde{s}_2(t) \\ \tilde{s}_3(t) \\ \tilde{s}_4(t) \\ \vdots \end{bmatrix} = \left(\frac{1}{l}\right) H_l^* \begin{bmatrix} \bar{s}_1(t) \\ \bar{s}_2(t) \\ \bar{s}_3(t) \\ \bar{s}_4(t) \\ \vdots \end{bmatrix}. \tag{2.9}$$

Once the k-space data $\bar{s}_v(t)$ is recovered for each separate slice v, a standard trans-

formation into the image domain can be performed, ideally with B_0 inhomogeneity correction. It is also possible to perform the transformation into the image domain first, then add and subtract the aliased slices using the Hadamard matrix to separate them.

Hadamard-encoded SMS was later extended to fMRI for the purposes of reduced signal dropout from susceptibility-induced gradients [30]. In that work, 2 simultaneous "subslices" were acquired using Hadamard-encoding and compared to a conventional acquisition consisting of a non-SMS acquisition with slice thickness twice that of each individual Hadamard subslice. The idea is that the thinner subslices using Hadamard-encoding will have reduced signal dropout from susceptibility-induced field gradients, but since 2 subslices are excited simultaneously, the accompanying SNR loss from the thinner subslices is avoided. However, this is done at the expense of temporal resolution.

In Ref. [30], instead of encoding each subslice with a $+1$ or -1 sign, every other subslice is encoded with a ± 1 or $\pm i$ multiplication. For example, with 4 simultaneous subslices, the Hadamard-encoding matrix is

$$H_4 = \begin{bmatrix} 1 & i & 1 & i \\ 1 & -i & 1 & -i \\ 1 & i & -1 & -i \\ 1 & -i & -1 & i \end{bmatrix}.$$

This is done so that the transition zones of the slice profiles do not vary from time frame to time frame, as shown in Figure 1 of Ref. [30], which results in more uniform slice profiles after reconstruction. For 2 simultaneous subslices, the encoding would just alternate between $1 + i$ and $1 - i$ from frame to frame, as shown in the slice profiles plotted in Figure 2.2.

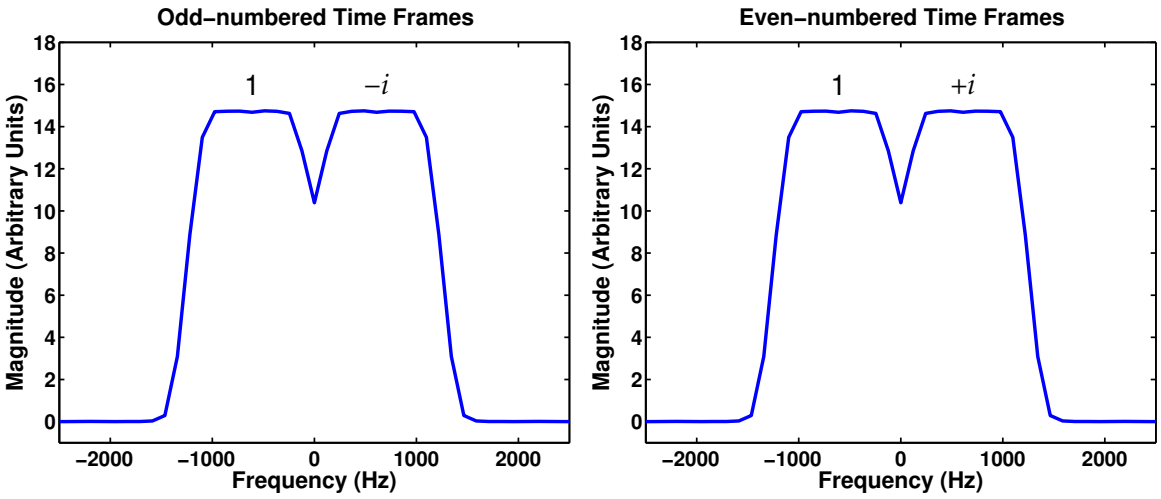

Figure 2.2: Slice profiles for Hadamard-encoded fMRI with 2 simultaneous slices.

In Ref. [30], simultaneously acquired subslices are modeled as

$$I_n = e^{i\phi} \sum_{m=1}^{M} S_{m,n} e^{i\theta_m}, \tag{2.10}$$

where n is the time frame number, $S_{m,n}$ is the magnitude of the mth subslice, θ_m is the phase difference between subslices arising from the susceptibility-induced field gradients, and ϕ is an overall phase shift. For 2 simultaneous subslices, a conventional acquisition is just

$$I_n^{\text{conv}} = e^{i\phi}(S_{1,n} + S_{2,n} e^{i\Delta\theta}),$$

where $\Delta\theta$ is the phase difference between subslices. The magnitude of the signal is

$$|I_n^{\text{conv}}| = \sqrt{S_{1,n}^2 + S_{2,n}^2 + 2S_{1,n}S_{2,n}\cos\Delta\theta}. \tag{2.11}$$

The Hadamard-encoded signal is modeled as

$$I_n^{\text{Hada}} = e^{i\phi}(S_{1,n} + i(-1)^n S_{2,n} e^{i\Delta\theta}), \tag{2.12}$$

making the magnitude

$$|I_n^{\text{Hada}}| = \sqrt{S_{1,n}^2 + S_{2,n}^2 - 2(-1)^n S_{1,n} S_{2,n} \sin \Delta\theta}. \tag{2.13}$$

Since the goal is to reduce signal dropout and not necessarily to recover the individual subslices, the authors propose the reconstruction process of low-pass filtering $|I_n^{Hada}|^2$ to get the time series

$$x_n = \sqrt{\mathcal{F}^{-1}\{W_n \mathcal{F}(|I_n^{Hada}|^2)\}}, \tag{2.14}$$

where $\mathcal{F}$ is the Fourier transform operator, and W_n is the spectrum of the low-pass filter. The low-pass filter removes the $-2(-1)^n S_{1,n} S_{2,n} \sin \Delta\theta$ term in Equation (2.13) to obtain

$$x_n = \sqrt{S_{1,n}^2 + S_{2,n}^2}. \tag{2.15}$$

Numerous other non-parallel methods have been created for SMS imaging. Ref. [31] introduced a method that uses a constant slice-select gradient during readout to shift simultaneously excited slices in the readout direction so that they are no longer overlapped in the final reconstruction. However, the readout slice-select gradient creates a skewing of the voxels, which manifests as an in-plane blur and tilted voxels. Ref. [32] developed phase-offset multiplanar (POMP) imaging, a method that also shifts simultaneously acquired slices so that they are not overlapped. Instead of using a gradient, the images are shifted in the phase encode direction using RF pulses that introduce a linear phase modulation across the phase encode direction. For each different phase encode line, a different RF pulse is used to add the appropriate amount of phase to each simultaneous slice to shift them apart. Both methods require a field of view large enough to accommodate multiple non-overlapping slices to prevent aliasing.

Ref. [33] proposed simultaneous multislice acquisition using rosette trajectories (SMART), an SMS method that uses rosette trajectories along with a readout slice-

select gradient that modulates each simultaneous slice to a different resonance frequency. This method took advantage of the tendency for rosette trajectories to destroy signal at off-resonance frequencies. Each slice is extracted by demodulating the data to the appropriate frequency such that the signal from the other slices is reduced. However, the signal from off-resonance slices is not entirely destroyed with this method, resulting in image artifacts and a decrease in SNR.

Simultaneous echo refocusing (SER) is yet another SMS method [34]. For 2 simultaneous slices, SER uses 2 consecutive RF pulses for each slice with an x-gradient blip in between. A single readout is then used to acquired echoes from both slices. The echoes are shifted in time due to the x-gradient blip applied between the RF pulses. While providing faster imaging than non-SMS EPI due to a reduced number of gradient switchings, SER still requires a longer readout to accommodate echoes from multiple slices staggered in time, as well as multiple consecutive RF pulses before each readout.

2.2.2 Parallel SMS Imaging

As parallel imaging became more widespread, differences in sensitivities from multiple receive coils were used to help separate the slices. For example, Equation (2.3) can be discretized to a sum of matrix vector products $\boldsymbol{s}_u = \sum_{v=1}^{l} \boldsymbol{Q}_v \boldsymbol{C}_{u,v} \boldsymbol{x}_v$, where $\boldsymbol{s}_u$ is the discretized signal for coil u, $\boldsymbol{x}_v$ is the lexicographically-ordered 2-dimensional discretized simultaneous slice v, $\boldsymbol{C}_{u,v}$ is a diagonal matrix containing the sensitivity of coil u to simultaneous slice v, and $\boldsymbol{Q}_v$ is the 2-dimensional Fourier transform operator, including B_0 inhomogeneity correction for slice v. For arbitrary readouts, $\boldsymbol{Q}_v$ can be implemented by a non-uniform fast Fourier transform (NUFFT) [35] with B_0 inhomogeneity correction [36]. Combining the equations for all coils into one, we

have

$$\begin{bmatrix} \boldsymbol{s}_1 \\ \boldsymbol{s}_2 \\ \vdots \\ \boldsymbol{s}_d \end{bmatrix} = \begin{bmatrix} \boldsymbol{Q}_1\boldsymbol{C}_{1,1} & \boldsymbol{Q}_2\boldsymbol{C}_{1,2} & \cdots & \boldsymbol{Q}_l\boldsymbol{C}_{1,l} \\ \boldsymbol{Q}_1\boldsymbol{C}_{2,1} & \boldsymbol{Q}_2\boldsymbol{C}_{2,2} & \cdots & \boldsymbol{Q}_l\boldsymbol{C}_{2,l} \\ \vdots & \vdots & \ddots & \vdots \\ \boldsymbol{Q}_1\boldsymbol{C}_{d,1} & \boldsymbol{Q}_2\boldsymbol{C}_{d,2} & \cdots & \boldsymbol{Q}_l\boldsymbol{C}_{d,l} \end{bmatrix} \begin{bmatrix} \boldsymbol{x}_1 \\ \boldsymbol{x}_2 \\ \vdots \\ \boldsymbol{x}_l \end{bmatrix}, \tag{2.16}$$

for d coils. Reconstruction of each slice becomes a matter of solving this linear equation for the $\boldsymbol{x}_v$ vector with an iterative algorithm such as Conjugate Gradient.

Larkman et al. [37] introduced a parallel imaging SMS method that separates slices entirely in the image domain. Aliased images for each coil are first transformed into the image domain, then the slices are separated using a simple matrix inversion. With their method, inhomogeneity correction is not performed, so that $\boldsymbol{Q}_v = \boldsymbol{Q}$ for all slices v. The problem is modeled as

$$\begin{bmatrix} \tilde{\boldsymbol{Q}}\boldsymbol{s}_1 \\ \tilde{\boldsymbol{Q}}\boldsymbol{s}_2 \\ \vdots \\ \tilde{\boldsymbol{Q}}\boldsymbol{s}_d \end{bmatrix} = \begin{bmatrix} \boldsymbol{C}_{1,1} & \boldsymbol{C}_{1,2} & \cdots & \boldsymbol{C}_{1,l} \\ \boldsymbol{C}_{2,1} & \boldsymbol{C}_{2,2} & \cdots & \boldsymbol{C}_{2,l} \\ \vdots & \vdots & \ddots & \vdots \\ \boldsymbol{C}_{d,1} & \boldsymbol{C}_{d,2} & \cdots & \boldsymbol{C}_{d,l} \end{bmatrix} \begin{bmatrix} \boldsymbol{x}_1 \\ \boldsymbol{x}_2 \\ \vdots \\ \boldsymbol{x}_l \end{bmatrix}, \tag{2.17}$$

where $\tilde{\boldsymbol{Q}}$ describes a non-specific transformation of k-space data into the object domain. The method is heavily dependent on coil geometry relative to slice orientation; if a coil has similar sensitivities to each simultaneous slice, the method is unable to separate the slices. Another problem is that B_0 inhomogeneity correction is not easily performed since the slice separation happens in the object domain.

The original formulation of parallel SMS imaging in Equation (2.16) also suffers from a heavy reliance on coil sensitivity differences between simultaneous slices. If the physical arrangement of the receive coils and slice prescription is such that the sensitivity for each coil is not sufficiently different between slices, then the problem in Equation (2.16) becomes very ill-conditioned. In this case, $\boldsymbol{C}_{u,v} \approx \boldsymbol{C}_{u,w}$ for $v \neq w$.

Note that $\boldsymbol{Q}_v$ is usually somewhat similar to $\boldsymbol{Q}_w$ for $v \neq w$ since the only difference between them is a different B_0 inhomogeneity correction for differing slices. Thus the system matrix in Equation (2.16) contains column-blocks that are similar to each other. This situation arises in a typical 8-channel head coil setup, where the coils are arranged around the head so that their sensitivities are very similar to different axial slices. From a sensitivity encoding (SENSE) [21] viewpoint, the coil sensitivities do not provide enough information to de-alias the simultaneously acquired images, and the resulting g-factor is too high.

The controlled aliasing in parallel imaging results in higher acceleration (CAIPIRINHA) [38] method addresses this issue by using RF pulses to modulate phase encode lines for certain slices, thereby shifting them relative to each other in the image domain for easier separation, very similar to POMP imaging. However, because multiple receive coils are used in CAIPIRINHA, a large FOV is not required as it is in POMP imaging. Nunes et al. [39] then extended SMS CAIPIRINHA to single-shot Cartesian trajectories by using a blipped z-gradient during readout instead of using the RF pulse for an interslice image shift. Their method is modeled as

$$s_u(t) = \sum_{v=1}^{l} e^{-i2\pi k_z(t) z_v} \int\int c_{u,v}(x,y) m_v(x,y) e^{-i2\pi(k_x(t)x + k_y(t)y + \Delta f_{0,v}(x,y)t)} \,\mathrm{d}x \,\mathrm{d}y, \tag{2.18}$$

which is discretized to

$$\begin{bmatrix} \boldsymbol{s}_1 \\ \boldsymbol{s}_2 \\ \vdots \\ \boldsymbol{s}_d \end{bmatrix} = \begin{bmatrix} \boldsymbol{M}_1\boldsymbol{Q}_1\boldsymbol{C}_{1,1} & \boldsymbol{M}_2\boldsymbol{Q}_2\boldsymbol{C}_{1,2} & \cdots & \boldsymbol{M}_l\boldsymbol{Q}_l\boldsymbol{C}_{1,l} \\ \boldsymbol{M}_1\boldsymbol{Q}_1\boldsymbol{C}_{2,1} & \boldsymbol{M}_2\boldsymbol{Q}_2\boldsymbol{C}_{2,2} & \cdots & \boldsymbol{M}_l\boldsymbol{Q}_l\boldsymbol{C}_{2,l} \\ \vdots & \vdots & \ddots & \vdots \\ \boldsymbol{M}_1\boldsymbol{Q}_1\boldsymbol{C}_{d,1} & \boldsymbol{M}_2\boldsymbol{Q}_2\boldsymbol{C}_{d,2} & \cdots & \boldsymbol{M}_l\boldsymbol{Q}_l\boldsymbol{C}_{d,l} \end{bmatrix} \begin{bmatrix} \boldsymbol{x}_1 \\ \boldsymbol{x}_2 \\ \vdots \\ \boldsymbol{x}_l \end{bmatrix}, \tag{2.19}$$

where each $\boldsymbol{M}_v$ is a diagonal matrix representing the z-gradient modulation to slice v. In other words, if the diagonal entries of $\boldsymbol{M}_v$ are represented by a discrete function

$m_v[n]$, then

$$\text{diag}\{\boldsymbol{M}_v\} = m_v[n] = e^{-i2\pi k_z[n] z_v}, \tag{2.20}$$

where $k_z[n]$ is a discretized $k_z(t)$. Compared to Equation (2.3), the only difference in Equation (2.18) is the $e^{-i2\pi k_z(t) z_v}$ term, which adds time-varying phase represented by each $\boldsymbol{M}_v$ in Equation (2.19). Similarly, the only difference between Equation (2.19) and Equation (2.16) is the $\boldsymbol{M}_v$ matrices. For a given z-gradient, the modulation will add $\gamma z_v \int_0^t g_z(\tau)\,\mathrm{d}\tau$ amount of phase to slice v at readout time t, where z_v is the distance of slice v to the z-gradient isocenter, and $g_z(t)$ is the z-gradient as a function of time. The reliance of the phase modulation on z_v causes the modulation to differ from slice to slice, so that $\boldsymbol{M}_v \neq \boldsymbol{M}_w$, for $v \neq w$.

The z-gradient modulation can be arbitrary, as long as slew rate and gradient amplitude limits are not breached. However, it is advantageous to choose a $g_z(t)$ function that makes the condition number of the system matrix in Equation (2.19) as low as possible. It may also be important to have the running integral of $g_z(t)$ periodically go to 0 to minimize through-plane intravoxel dephasing. In other words, the z-gradient should contain rewinders to ensure that too much phase does not accumulate along the z-direction. The method by Nunes et al. [39] did not use such rewinders, causing significant through-plane dephasing of the finite-thick slices. Setsompop et al. [40] then developed the blipped-CAIPI method, which uses alternating $g_z(t)$ blips to overcome this issue.

The closely related methods by Nunes et al. and Setsompop et al. can be described by Figure 2.3, which gives a more intuitive explanation as to why the readout z-gradient modulation is beneficial for SMS imaging. Figure 2.3 shows a 2 simultaneous slice acquisition with no readout z-gradient in the top row, and a 2 simultaneous slice acquisition with a blipped z-gradient in the bottom row. The individual slices are shown in the left and center columns; the left column shows the slice that occurs at z-isocenter, and the middle column shows the slice that occurs some distance away. The

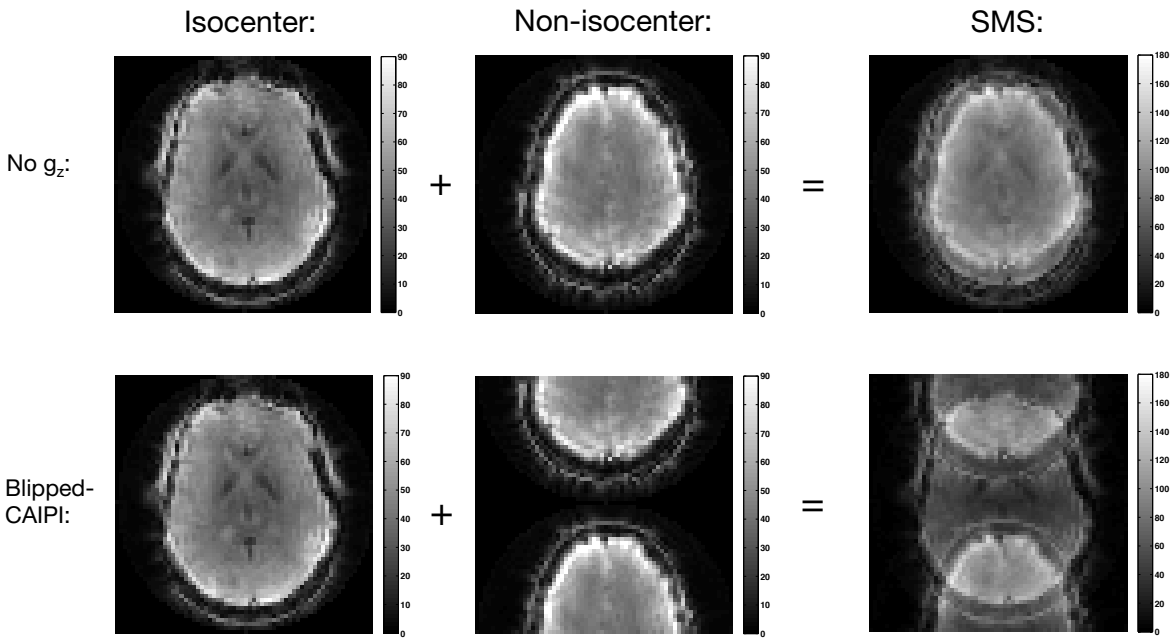

Figure 2.3: Two simultaneous slice acquisitions with no readout z-gradient (top row), and a blipped-CAIPI readout z-gradient (bottom row). The SMS acquisition is shown in the right column, which is simply the sum of the individual slices shown in the left and middle columns.

resulting aliased simultaneous slice acquisition is shown in the right column. With no z-gradient, the simultaneously acquired slices are perfectly overlapped, making it difficult to separate them unless their sensitivities are very different. For blipped-CAIPI, the z-gradient shifts the non-isocenter slice, resulting in less overlap in the SMS acquisition. This results in easier slice separation.

The phases of the $\boldsymbol{M}_v$ matrices in Equation (2.19) differ from each other only by the scalar multiple z_v, so in order to make each $\boldsymbol{M}_v$ as different as possible to improve conditioning, the simultaneous slices should be separated at even distances from each other. This way, the additional phase that each simultaneous slice experiences from the z-gradient modulation is spread out as much as possible in the z-direction. Furthermore, it is desirable to separate the simultaneous slices by the maximum distance possible in order to fully use the coil sensitivity information as part of the slice separation process; in general, slices further apart will have more differences in sensitivity

than slices that are nearby. An RF pulse that creates such a configuration can be written in the form of Equation (2.4), with $\tilde{f}_v = f_{\mathrm{RF}}(v-1)\Delta z/\zeta$, where Δz is the distance between the simultaneous slices, and ζ is the slice thickness. An example slice profile for 3 simultaneous slices acquired in this manner is given in Figure 2.4. The full brain volume is covered by imaging consecutive slices with each successive

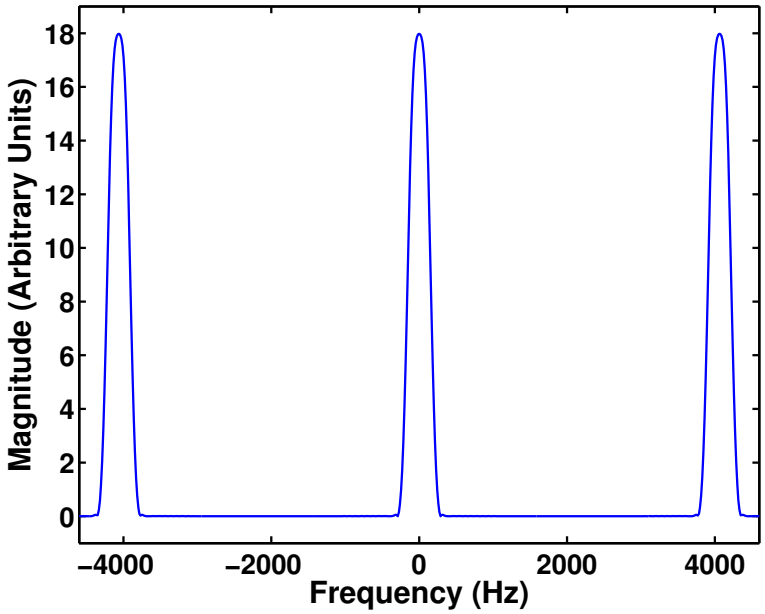

Figure 2.4: Slice profile for a 3 simultaneous slice acquisition created from the 6.4 ms Hamming-windowed sinc with 4 zero-crossings shown in Figure 2.1.

TR, while keeping the distance between the simultaneous slices the same. Using the previous expression for $\tilde{f}_v$ with consecutive slices located right next to each other, there would be $\Delta z/\zeta$ acquisitions for a total of $l\Delta z/\zeta$ slices for the whole volume.

However, one must be careful of phase wraps; if the magnitude of $g_z(t)$ is enough to cause any number of phase wraps across the z-axis, the phase modulation for each simultaneous slice could end up being very similar even if the slices are all separated from each other by some even distance. For example, if z_1, z_2, and z_3 are 0, 1, and 2, respectively, and $\gamma z_3 \int_0^t g_z(\tau)\,\mathrm{d}\tau = 4\pi$, then slice 2 experiences a phase modulation of 2π, and slice 1 experiences a modulation of 0. However, if z_1, z_2, and z_3 are 0,

1/3, and 2/3, respectively, then the modulation for slices 1, 2, and 3 are 0, $2\pi/3$, and $4\pi/3$, respectively, which is the maximum phase spread possible. From a Fourier perspective, this means that for simultaneous slices that are closer together, a higher k_z value is needed, which means we need to use a larger $g_z(t)$ to go out further in k_z-space. This also means that for a given simultaneous slice separation distance, a larger z-gradient is not necessarily better for reconstruction, even when ignoring through-plane dephasing effects.

To better understand the effect of the readout z-gradient, Zahneisen et al. [41] introduced a general framework for SMS using a 3-dimensional Fourier viewpoint. They note that the simultaneous slices create a field of view (FOV) with accompanying resolution in the z-direction. The FOV is just

$$\mathrm{FOV}_z = l\Delta z, \tag{2.21}$$

where l is the number of simultaneously acquired slices and Δz is the distance between simultaneous slices. Therefore, the necessary distance between k-space samples in the z-direction is

$$\Delta k_z = \frac{1}{\mathrm{FOV}_z} = \frac{1}{l\Delta z}. \tag{2.22}$$

The distance between simultaneous slices, Δz, specifies the resolution δ_z in the z-direction. The maximum extent of k_z-space is then

$$\begin{aligned} k_z^{\max} &= \frac{1}{2\delta_z} \\ &= \frac{l}{2\mathrm{FOV}_z} \\ &= \frac{1}{2\Delta z} \\ &= \frac{l\Delta k_z}{2}. \end{aligned} \tag{2.23}$$

A SENSE [21] reconstruction of the simultaneous slice data is done by solving

Equation (2.19) for the $\boldsymbol{x}_v$ vector. This problem is typically overdetermined since the number of coils is greater than the number of simultaneous slices, and the number of k-space samples for each readout is comparable to the number of pixels in each slice for spiral imaging. In addition, noise from Eddy currents and hardware imperfections will be present in the raw data. Therefore, it can be beneficial to use the following regularized least squares problem for reconstruction:

$$\hat{\boldsymbol{x}} = \arg\min_{\boldsymbol{x}} \left\{ \|\boldsymbol{A}\boldsymbol{x} - \boldsymbol{s}\|_2^2 + \beta \|\boldsymbol{R}\boldsymbol{x}\|_2^2 \right\}, \tag{2.24}$$

where $\boldsymbol{A}$, $\boldsymbol{x}$, and $\boldsymbol{s}$ are the system matrix, $\boldsymbol{x}_v$ vector, and $\boldsymbol{s}_u$ vector in Equation (2.19), respectively. $\boldsymbol{R}$ is a finite differencing matrix, and β is the regularization parameter that controls the tradeoff between spatial resolution and noise reduction in the reconstruction $\hat{\boldsymbol{x}}$. The least squares solution to (2.24) is $\hat{\boldsymbol{x}} = (\boldsymbol{A}'\boldsymbol{A} + \beta\boldsymbol{R}'\boldsymbol{R})^{-1}\boldsymbol{A}'\boldsymbol{s}$, which can be computed using the Conjugate Gradient algorithm [42] and implemented using Jeffrey A. Fessler's Image Reconstruction Toolbox [43].

Although $\boldsymbol{x}$ is 3-dimensional since it contains multiple 2-dimensional slices, $\boldsymbol{R}$ cannot be a 3-dimensional finite differencing matrix because differences would be computed between pixels that are in different slices separated from each other by a relatively large distance. Since $\boldsymbol{x}$ consists of l separate slices, $\boldsymbol{R}$ should perform the operation of a block diagonal matrix with each block performing a 2-dimensional finite difference computation on a single slice. In other words, $\boldsymbol{R}$ can be implemented as

$$\boldsymbol{R} = \begin{bmatrix} \boldsymbol{D}_1 & \boldsymbol{0} & \boldsymbol{0} & \boldsymbol{0} \\ \boldsymbol{0} & \boldsymbol{D}_2 & \ddots & \boldsymbol{0} \\ \boldsymbol{0} & \ddots & \ddots & \boldsymbol{0} \\ \boldsymbol{0} & \boldsymbol{0} & \boldsymbol{0} & \boldsymbol{D}_l \end{bmatrix}, \tag{2.25}$$

where $\boldsymbol{D}_1 = \boldsymbol{D}_2 = \ldots = \boldsymbol{D}_l$ is a 2-dimensional finite differencing matrix for one slice with differences in the horizontal, vertical and diagonal in-plane directions. This

construction ensures that differences are not computed between pixels that are in different slices.

The value of β can be chosen using resolution analysis of the system point spread function (PSF). The system PSF is defined as $(\boldsymbol{A}'\boldsymbol{A} + \beta\boldsymbol{R}'\boldsymbol{R})^{-1}\boldsymbol{A}'\boldsymbol{A}\boldsymbol{e}_j$, where $\boldsymbol{e}_j$ is the jth unit vector or "point." After computing this value using Conjugate Gradient, the full-width-at-half-maximum (FWHM) of the PSF can be measured along each of the three physical dimensions of the image. In this dissertation, a FWHM in the slice plane of around 1.3 pixels was found to work well by inspection, which yielded a value of $\beta = 273$ for all the experiments.

In this dissertation, B_0 inhomogeneity field maps are computed using an angle measurement method [44] from two scans with different TEs: one with a TE of 30 ms, and one of 32 ms. First, the images themselves are reconstructed for each coil by effectively computing an inverse NUFFT of the k-space data for each coil using Conjugate Gradient. Then, the field map $\angle(x^{0*}_{w,u}x^{1}_{w,u})/\Delta t$ is calculated, where $x^{0}_{w,u}$ is the wth pixel of coil u of one scan, $x^{1}_{w,u}$ is the wth pixel of coil u of the other scan, and Δt is the difference in TEs between the two scans, which is 2 ms in this case. The field maps are then summed across coils and smoothed by convolving with a 7-by-7 constant kernel. Finally, the original 2 scans are reconstructed again with inhomogeneity correction using the new field map, and the process is repeated to obtain a better estimate of the field map.

Coil sensitivities can be obtained by directly computing

$$\hat{\boldsymbol{c}}_{u,v} = \underset{\boldsymbol{c}_{u,v}}{\arg\min} \left\{ \|\boldsymbol{x}_{u,v} - \boldsymbol{B}_v\boldsymbol{c}_{u,v}\|_2^2 + \lambda \|\boldsymbol{D}\boldsymbol{c}_{u,v}\|_2^2 \right\}, \tag{2.26}$$

using $\hat{\boldsymbol{c}}_{u,v} = (\boldsymbol{B}_v'\boldsymbol{B}_v + \lambda\boldsymbol{D}'\boldsymbol{D})^{-1}\boldsymbol{B}_v'\boldsymbol{x}_{u,v}$, where $\boldsymbol{c}_{u,v}$ is the sensitivity of coil u to slice v, $\boldsymbol{x}_{u,v}$ is the inhomogeneity-corrected reconstruction for coil u and slice v, $\boldsymbol{B}_v$ is a diagonal matrix containing the square-root-sum-of-squares of images from all coils,

and $\boldsymbol{D}$ is a 2-dimensional finite differencing matrix. Coil sensitivities can also be computed using more recent techniques such as ESPIRiT [45].

Note that the B_0 inhomogeneity field maps and coil sensitivity maps must be computed from a non-SMS acquisition that has at least the same number of slices per volume as the reconstructed SMS scan, and with individual slices at the same locations as those for the SMS scan. For all the SENSE experiments in this dissertation, a separate non-SMS acquisition with matching slice locations was performed before each SMS scan.

Along with blipped-CAIPI, Setsompop et al. [40] also developed slice-GRAPPA, a k-space reconstruction scheme for slice separation. Slice-GRAPPA uses a different convolution kernel to construct the k-space data for each coil of each separated slice. Figure 2.5 illustrates the kernel operation for one coil of one separated slice. Each

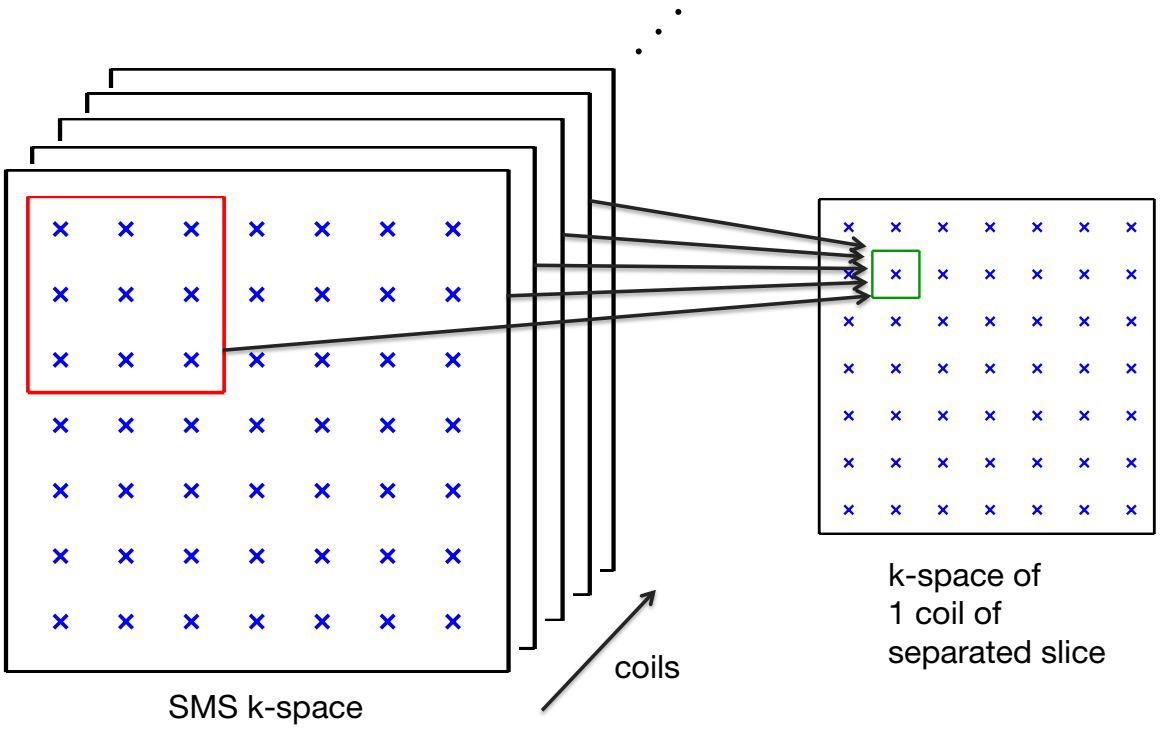

Figure 2.5: Slice-GRAPPA kernel operation to compute the k-space data for one coil of one separated slice. Each kernel operates on all coils of the SMS k-space data.

kernel operates on all coils of the SMS k-space data. A different kernel is needed to compute a different coil of that same slice in Figure 2.5. Finally, a whole set of additional kernels are needed to compute all the coils of another separated slice.

Moeller et al. [46] demonstrated the use of Cartesian SMS imaging in fMRI at 7 T, but did not use a CAIPI approach to improve the g-factor. Their demonstration used coronal slices to improve the g-factor because this orientation, along with a sagittal orientation, provided the most differences in coil sensitivity from slice to slice. They used the SENSE/GRAPPA [47] reconstruction method to separate the slices.

Recently, Zahneisen et al. [48] adapted blipped-CAIPI to single-shot spirals and demonstrated SMS imaging with a blipped spiral-in readout. An example of a blipped spiral trajectory for a 3 simultaneous slice acquisition is shown in Figure 2.6. In fMRI, spiral-in readouts have advantages over Cartesian-based ones like echo planar imaging (EPI) such as better signal recovery [49] and shorter readout times [17, 50], which reduces off-resonance distortion and also increases the maximum number of slices acquired per unit time. Furthermore, spiral trajectories have reduced sensitivity to motion when compared with EPI [51].

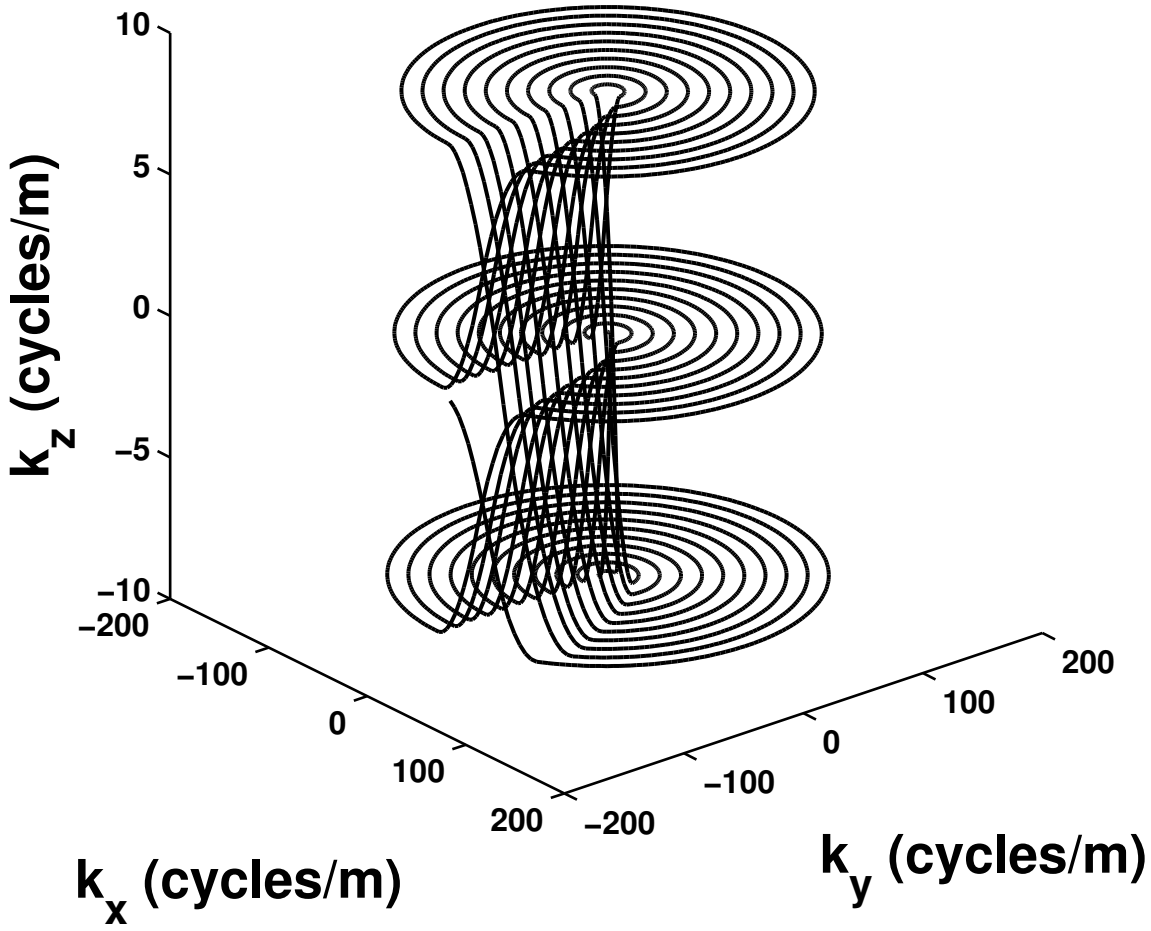

Figure 2.6: Three-dimensional blipped spiral k-space trajectory for a 3 simultaneous slice acquisition.

CHAPTER 3

Hadamard-encoded Simultaneous Multislice fMRI[1]

3.1 Hadamard-encoding for Reduced Signal Dropout

Hadamard-encoded SMS can be used to acquire thinner slices in order to reduce the signal dropout from through-plane dephasing. In Ref. [30], a method involving an incoherent addition of subslices, described by Equation (2.14), was proposed. In this section, it is shown that there is a signal recovery benefit to reconstructing the individual subslices first, then combining them afterwards. Similar to what was done in Ref. [30], two simultaneous subslices are acquired with each acquisition in this section. The conventional non-SMS comparison has individually acquired slices, each with width equal to the combined width of two simultaneous Hadamard-encoded subslices. In other words, the width of each Hadamard subslice is one-half that of a conventional slice.

3.1.1 Separation of Slices for Reduced Signal Dropout

In Ref. [30], Hadamard-encoded SMS images were reconstructed by filtering the squared magnitude of the signal as described by Equation (2.14), which results in

[1]Parts of this chapter are based on Refs. [52] and [53].

the magnitude combination of subslices given by Equation (2.15). However, this is not an optimal slice combination in terms of reducing signal dropout.

For example, assume that a conventional acquisition is performed with no susceptibility-induced field gradients. Substituting $\Delta\theta = 0$ in Equation (2.11), we have

$$\begin{aligned} |I_n^{\text{conv}}| &= \sqrt{S_{1,n}^2 + S_{2,n}^2 + 2S_{1,n}S_{2,n}\theta} \\ &= \sqrt{(S_{1,n} + S_{2,n})^2} \\ &= S_{1,n} + S_{2,n}, \end{aligned}$$

which is just the sum of the magnitudes of each subslice. However, with the reconstruction of Hadamard-encoded SMS proposed by Ref. [30], the resulting data has magnitude $\sqrt{S_{1,n}^2 + S_{2,n}^2}$, as given by Equation (2.15). This is equivalent to the signal obtained with a conventional acquisition where there is a $\Delta\theta = \pi/2$ phase difference between subslices, seen by substituting $\Delta\theta = \pi/2$ in Equation (2.11). In fact, since $0 < \cos\Delta\theta < 1$ for $-\pi/2 < \Delta\theta < \pi/2$, a conventional acquisition has better signal recovery compared to a Hadamard acquisition when the phase difference between subslices is less than $\pi/2$. Only when the phase difference between subslices is greater than $\pi/2$ does Hadamard-encoded SMS have better signal recovery using the method proposed by Ref. [30].

For the purposes of reduced signal dropout, it is better to reconstruct the individual Hadamard-encoded subslices, then combine the subslices. In other words, filter the complex Hadamard-encoded signal I_n^{Hada} given by Equation (2.12) to obtain

$$S_{1,n}e^{i\phi} = \mathcal{F}^{-1}\{W_n\mathcal{F}(I_n^{Hada})\}, \tag{3.1}$$

where W_n is the spectrum of the low-pass filter. For the other subslice, first modulate

the complex time series, then low-pass filter to obtain

$$S_{2,n}e^{i(\phi+\Delta\theta)} = \mathcal{F}^{-1}\{W_n\mathcal{F}(i(-1)^{n+1}I_n^{Hada})\}. \tag{3.2}$$

For sufficiently large $S_{1,n}$ and $S_{2,n}$, $\Delta\theta$ can be estimated by taking the difference of the phases of $S_{1,n}e^{i\phi}$ and $S_{2,n}e^{i(\phi+\Delta\theta)}$, then $S_{1,n}e^{i\phi}$ and $S_{2,n}e^{i\phi}$ can be summed and transformed into the object domain. Alternatively, if the global phase ϕ is not needed, the magnitudes $S_{1,n}$ and $S_{2,n}$ can be simply summed and transformed. In this case, the magnitude of the signal will be $S_{1,n}+S_{2,n}$ regardless of the value of $\Delta\theta$, equivalent to a conventional acquisition with no susceptibility-induced field gradients.

3.1.2 SNR Analysis

Ref. [30] also makes the claim that using a low-pass filter W_n with cutoff one-half the Nyquist frequency, their proposed Hadamard-encoding has an SNR advantage over conventional acquisitions. Assuming equal magnitudes of 1 in each subslice and uncorrelated thermal noise with standard deviation σ_0 in each acquisition, the SNR for a conventional acquisition due to thermal noise is

$$\mathrm{SNR}_0^{\mathrm{conv}} = \frac{\sqrt{2+2\cos\Delta\theta}}{\sigma_0}, \tag{3.3}$$

since the signal magnitude given by substituting $S_{1,n} = S_{2,n} = 1$ into Equation (2.11) is just $S^{\mathrm{conv}} = \sqrt{2+2\cos\Delta\theta}$.

For their proposed Hadamard-encoded SMS, the signal magnitude from Equation (2.15) is $S^{\mathrm{Hada}} = \sqrt{1^2+1^2} = \sqrt{2}$, assuming that the low-pass filter W_n behaves perfectly. To compute the effects of the low-pass filter W_n, they use Parseval's theorem, which states that the variance of the signal is reduced by the area under W_n. In other words, σ_0^2 is reduced to $c\sigma_0^2$, where $c = \frac{1}{N}\sum_{n=0}^{N-1} W_n^2$, making $0 \leq c \leq 1$.

Therefore, the SNR for a Hadamard-encoded acquisition due to thermal noise is

$$\mathrm{SNR}_0^{\mathrm{Hada}} = \frac{\sqrt{2}}{\sigma_0\sqrt{c}}. \tag{3.4}$$

Rewriting Equation (3.4), we have

$$\begin{aligned}
\mathrm{SNR}_0^{\mathrm{Hada}} &= \left(\frac{1}{\sqrt{c}}\right)\left(\frac{\sqrt{2}}{\sqrt{2+2\cos\Delta\theta}}\right)\left(\frac{\sqrt{2+2\cos\Delta\theta}}{\sigma_0}\right) \\
&= \left(\frac{\sqrt{2}}{\sqrt{c}\sqrt{2+2\cos\Delta\theta}}\right)\left(\frac{\sqrt{2+2\cos\Delta\theta}}{\sigma_0}\right) \\
&= \left(\frac{1}{\sqrt{c(1+\cos\Delta\theta)}}\right)\mathrm{SNR}_0^{\mathrm{conv}}.
\end{aligned} \tag{3.5}$$

Assuming no susceptibility-induced field gradients so that $\Delta\theta = 0$, when the low-pass filter cutoff is half the Nyquist frequency, then $c = \frac{1}{2}$, making $\mathrm{SNR}_0^{\mathrm{Hada}} = \mathrm{SNR}_0^{\mathrm{conv}}$. With no filtering, $c = 1$ so that Equation (3.5) becomes $\mathrm{SNR}_0^{\mathrm{Hada}} = \left(\frac{1}{\sqrt{2}}\right)\mathrm{SNR}_0^{\mathrm{conv}}$, which makes sense since with no through-plane dephasing, $S^{\mathrm{conv}} = 2$ and $S^{\mathrm{Hada}} = S^{\mathrm{conv}}/\sqrt{2}$, so $\mathrm{SNR}_0^{\mathrm{Hada}} = S^{\mathrm{Hada}}/\sigma_0 = S^{\mathrm{conv}}/(\sigma_0\sqrt{2}) = \left(\frac{1}{\sqrt{2}}\right)\mathrm{SNR}_0^{\mathrm{conv}}$.

From Ref. [54], the SNR of a signal S with total image noise standard deviation σ is

$$\begin{aligned}
\mathrm{SNR} &= \frac{S}{\sigma} \\
&= \frac{S}{\sqrt{\sigma_0^2+\sigma_p^2}} \\
&= \frac{S}{\sqrt{\sigma_0^2+\lambda^2S^2}}, \\
&= \frac{S}{\sigma_0\sqrt{1+\lambda^2S^2/\sigma_0^2}}, \\
&= \frac{\mathrm{SNR}_0}{\sqrt{1+(\lambda\mathrm{SNR}_0)^2}},
\end{aligned} \tag{3.6}$$

where $\sigma^2 = \sigma_0^2 + \sigma_p^2$, σ_p^2 is the variance from physiological noise, and $\sigma_p = \lambda S$, where λ is a constant that represents the decrease in SNR from signal-dependent fluctuations.

Using Equations 3.5 and 3.6,

$$\begin{aligned}\frac{\mathrm{SNR}^{\mathrm{Hada}}}{\mathrm{SNR}^{\mathrm{conv}}} &= \frac{\mathrm{SNR}_0^{\mathrm{Hada}}}{\sqrt{1+(\lambda \mathrm{SNR}_0^{\mathrm{Hada}})^2}} \frac{\sqrt{1+(\lambda \mathrm{SNR}_0^{\mathrm{conv}})^2}}{\mathrm{SNR}_0^{\mathrm{conv}}} \\ &= \frac{\mathrm{SNR}_0^{\mathrm{conv}}}{\sqrt{c(1+\cos\Delta\theta)}\sqrt{1+(\lambda \mathrm{SNR}_0^{\mathrm{conv}})^2/(c(1+\cos\Delta\theta))}} \frac{\sqrt{1+(\lambda \mathrm{SNR}_0^{\mathrm{conv}})^2}}{\mathrm{SNR}_0^{\mathrm{conv}}} \\ &= \frac{\sqrt{1+(\lambda \mathrm{SNR}_0^{\mathrm{conv}})^2}}{\sqrt{c(1+\cos\Delta\theta)+(\lambda \mathrm{SNR}_0^{\mathrm{conv}})^2}}.\end{aligned} \tag{3.7}$$

Assuming $\Delta\theta = 0$ and $c = \frac{1}{2}$, the SNR for Hadamard-encoding and conventional acquisitions is the same. In order for Hadamard-encoding to have an SNR advantage, a low-pass filter with cutoff lower than half the Nyquist frequency must be used so that $c < \frac{1}{2}$ and $\mathrm{SNR}^{\mathrm{Hada}}/\mathrm{SNR}^{\mathrm{conv}} > 1$. Note that there is a tradeoff with temporal resolution; the degrees of freedom in the Hadamard scan is multiplied by the factor c so that even with $c = \frac{1}{2}$, the temporal resolution is cut in half.

However, as long as there is some through-plane dephasing, $\Delta\theta > 0$ making $\mathrm{SNR}^{\mathrm{Hada}}/\mathrm{SNR}^{\mathrm{conv}} > 1$ even with a low-pass filter with cutoff exactly at half the Nyquist frequency. Therefore, there is an SNR benefit even with $c = \frac{1}{2}$ because of the susceptibility-induced gradients. When $c \geq \frac{1}{2}$, from Equation (3.7), $\mathrm{SNR}^{\mathrm{Hada}}/\mathrm{SNR}^{\mathrm{conv}} > 1$ when

$$\begin{aligned} c(1+\cos\Delta\theta) &< 1 \\ \Delta\theta &> \arccos\left(\frac{1}{c}-1\right). \end{aligned} \tag{3.8}$$

When $c < \frac{1}{2}$, there will always be an SNR benefit since $(1+\cos\Delta\theta) < 2$. If a higher low-pass filter cutoff is used to preserve temporal resolution, then there is only an SNR benefit at larger angles of $\Delta\theta$. For example, with $c = \frac{2}{3}$, $\mathrm{SNR}^{\mathrm{Hada}}/\mathrm{SNR}^{\mathrm{conv}} > 1$ only when $\Delta\theta > \frac{\pi}{3}$.

This SNR analysis can be extended to the reconstruction of individual subslices

as proposed with Equations 3.1 and 3.2. If the subslice separation is performed before combining them, then the magnitude signal is $S^{\text{Hada}} = |1 + 1| = 2$ after combining. Assuming the noise is uncorrelated between subslices, the variance sums to $c\sigma_0^2 + c\sigma_0^2 = 2c\sigma_0^2$ so that

$$\begin{aligned} \text{SNR}_0^{\text{Hada}} &= \frac{2}{\sqrt{2c\sigma_0^2}} \\ &= \frac{\sqrt{2}}{\sigma_0\sqrt{c}} \\ &= \left(\frac{1}{\sqrt{c(1+\cos\Delta\theta)}}\right)\text{SNR}_0^{\text{conv}}, \end{aligned} \tag{3.9}$$

which is the same as Equations 3.4 and 3.5, which both characterize the SNR using the incoherent sum method from Ref. [30]. Again, it's important to note that this assumes perfect subslice separation from the low-pass filter W_n. It follows that $\text{SNR}^{\text{Hada}}/\text{SNR}^{\text{conv}}$ is the same as in Equation (3.7), with all the same conclusions drawn above. For typical values of $\lambda = 0.008$ and $\text{SNR}_0 = 100$ from Ref. [54], Figure 3.1 plots $\text{SNR}^{\text{Hada}}/\text{SNR}^{\text{conv}}$ as a function of c and $\Delta\theta$ for either Hadamard reconstruction method.

3.1.3 Conclusions

In summary, for reconstruction of Hadamard-encoded fMRI, there is a signal recovery advantage in reconstructing individual subslices first, then combining them, as described by Equation (3.1) and Equation (3.2). For the incoherent sum method from Ref. [30] described by Equation (2.14), Hadamard-encoded fMRI has better signal recovery than conventional non-SMS fMRI only when the phase difference between subslices, $\Delta\theta$, is greater than $\pi/2$. When reconstructing subslices first, the signal recovery is maximal regardless of $\Delta\theta$, assuming clean subslice separation. The obvious disadvantage of reconstructing subslices first is that twice the number of slices need to

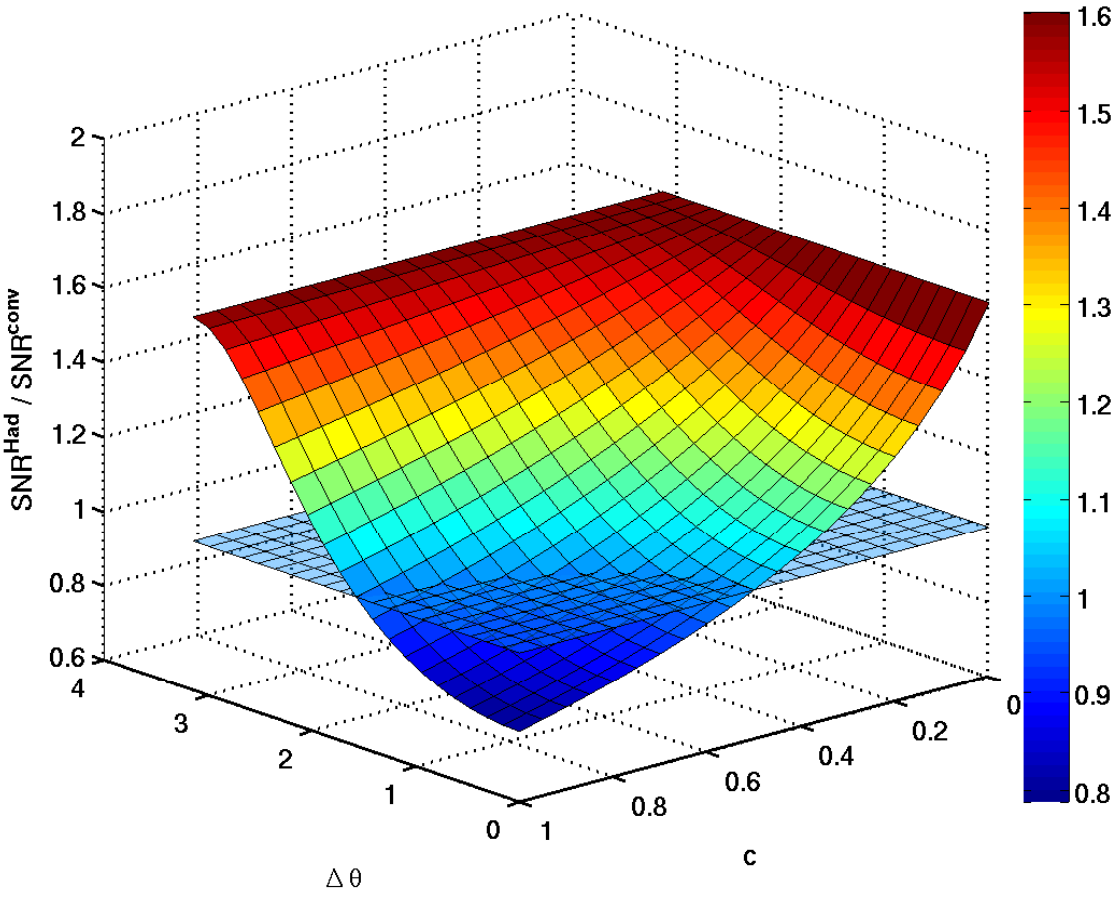

Figure 3.1: $\mathrm{SNR}^{\mathrm{Hada}}/\mathrm{SNR}^{\mathrm{conv}}$ described by Equation (3.7) when reconstructing the slices by filtering the squared magnitude of the data. Assuming no noise correlation between subslices, this is also the SNR ratio when reconstructing slices by separating subslices first, then combining. Typical values of $\lambda = 0.008$ and $\mathrm{SNR}_0 = 100$ from Ref. [54] are used. The plane at $\mathrm{SNR}^{\mathrm{Hada}}/\mathrm{SNR}^{\mathrm{conv}} = 1$ is shown for illustration. A significant portion of the plot is below 1, indicating an SNR disadvantage for Hadamard-encoding for those values of c and $\Delta\theta$.

be transformed into the image domain, which could amount to a significant amount of computational time, especially if an iterative algorithm is used.

As for the SNR, several assumptions need to be made, but in general, the incoherent sum method of Ref. [30] has comparable SNR to reconstructing individual subslices, then combining them. In either case, the SNR depends on the temporal filter cutoff c, and the phase difference between subslices $\Delta\theta$, as shown in Figure 3.1.

There, it is seen that for cutoffs less than 50% of the Nyquist frequency, the SNR is always better than a conventional scan, but for cutoffs greater than 50%, there is only an SNR benefit with greater values of $\Delta\theta$.

3.2 Hadamard-encoding for Accelerated Image Acquisition

Hadamard-encoding can also be used to accelerated image acquisition. Similarly to what was done previously, two simultaneous Hadamard-encoded slices are acquired per TR in this section. However, because the aim is acceleration, the width of each Hadamard slice is set to the width of a conventional, non-SMS acquisition. This results in a two-fold acceleration, covering the same brain region as a conventional non-SMS scan while requiring only half the TR. Note the change in terminology from Section 3.1; in this section, what was previously called a subslice is now called a slice since it now has the desired thickness of a conventional non-SMS slice.

3.2.1 Image Acquisition and Slice Separation

Simultaneously acquired slices can still be modeled using Equation (2.10), where $S_{m,n}$ is the magnitude of the mth slice at time frame number n. However, in this case, ϕ and θ_m are of no importance since we want the magnitude of each separated slice and not a combination or sum of slices as before. The Hadamard-encoded signal for 2 simultaneous slices can also be modeled as Equation (2.12). In order to encode the slices, two different RF pulses are alternated from frame to frame. In this work, the two RF pulses were created by summing two frequency-modulated Hamming-weighted sinc functions to obtain

$$\mathrm{RF}(t) = \left(e^{-i\pi f_0 t}\,\mathrm{sinc}(f_0 t) + i(-1)^n e^{i\pi f_0 t}\,\mathrm{sinc}(f_0 t)\right)\left[0.54 + 0.46\cos(2\pi t/T)\right], \quad (3.10)$$

where T is the duration of the pulse, $|t| < T/2$, f_0 is the bandwidth of the sinc, and $n = 0, 1, \ldots, N-1$ is the time frame of the pulse for N frames. The resulting slice profiles are shown in Figure 2.2. To extract or separate the slices, the magnitude of Equation (3.1) and 3.2 are computed to obtain $S_{1,n}$ and $S_{2,n}$, respectively, since image magnitudes are typically used to determine activation in fMRI. Taking the magnitude removes the effect of ϕ and $\Delta\theta$.

3.2.2 Importance of Physiological Noise

Although image magnitudes are used to determine activation in Hadamard-encoded fMRI, the time series phase is of great importance for clean slice separation and hence accurate image magnitudes. Note that the only difference between the excitation for each slice is the $i(-1)^n$ term in the RF pulse in Equation (3.10), which offsets the phase for that slice by $\pi/2$ or $-\pi/2$, depending on the time frame. The temporal filtering used for slice extraction is entirely dependent on this phase change from frame to frame. If the phase change varies, the temporal filter will not separate the slices as cleanly.

Physiological noise causes variations in not only the magnitude of the data, but also the phase [55]. Since the temporal filter W_n operates on complex data for slice separation, signal variations from physiological motion can potentially have a greater effect on Hadamard-encoded fMRI when compared to a conventional scan, where variations in the phase do not introduce additional errors in the reconstruction. In addition, during the separation of Hadamard-encoded slices, each slice requires data from at least two excitations, which can occur at different positions in a physiological motion cycle. Therefore, physiological noise correction is a crucial part of Hadamard-encoded fMRI, and it is important to perform the correction before slice separation.

3.2.3 Methods

In this work, four different methods were compared using fMRI scans: Hadamard-encoded SMS imaging with physiological noise correction (HDP), Hadamard-encoded SMS imaging without correction (HD), conventional non-SMS imaging with physiological noise correction (CNP), and conventional imaging without correction (CN). For the conventional methods, a TR of 2 s was used, and for the Hadamard-encoded scans, a TR of 1 s was used.

3.2.3.1 Physiological Noise Correction

The RETROICOR-based [16] physiological noise correction procedure used in this work models the physiological noise using

$$y(t) = \sum_{m=1}^{2} a_m^c \cos(m\phi_c) + b_m^c \sin(m\phi_c) + a_m^r \cos(m\phi_r) + b_m^r \sin(m\phi_r) \tag{3.11}$$

as in Ref. [16], but computes the coefficients a_m^x and b_m^x using a linear regression with $\cos(m\phi_x)$ and $\sin(m\phi_x)$ as regressors, along with four additional regressors consisting of a constant, linear, quadratic, and cubic trend, where x is c or r. In Equation (3.11), ϕ_c and ϕ_r are the cardiac and respiratory phases, respectively, computed from the subject's pulse and abdominal motion, and the c and r superscripts and subscripts refer to cardiac and respiratory noise, respectively. Noise and trends are corrected by simply subtracting the estimated noise and trends from the time series data for each voxel.

Hadamard-encoding with two simultaneous slices introduces a phase change in the data with every time frame, resulting in a phase time series pattern similar to what is shown in Figure 3.2, which can be challenging for linear regression to handle appropriately. For example, cardiac pulsation at 88 beats per minute produces noise at 1.47 Hz, which aliases to 0.47 Hz, very close to the Nyquist frequency of 0.5 Hz.

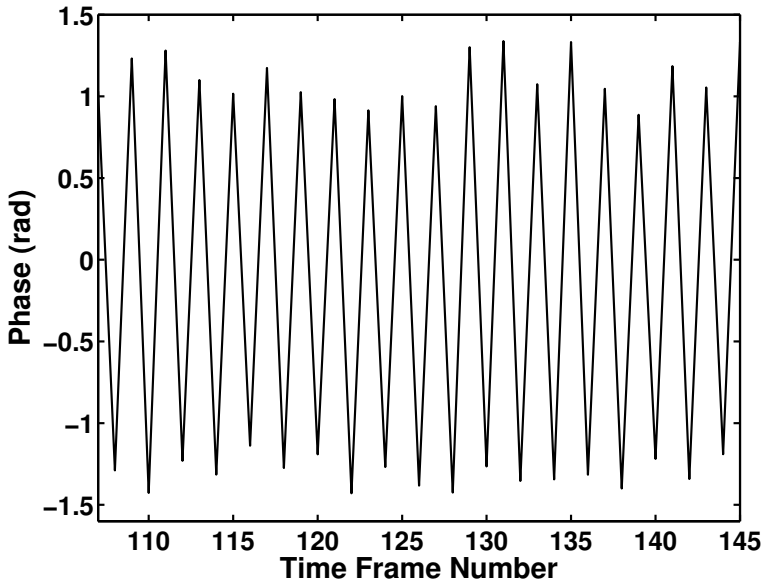

Figure 3.2: Example phase time series for one non-separated voxel of a Hadamard-encoded fMRI scan with two simultaneously acquired slices.

Since the $i(-1)^n$ Hadamard-encoding occurs at the Nyquist frequency, the regression will mistake the Hadamard-encoding for cardiac noise and much of the encoding will then be removed. Therefore, for the Hadamard scans, the RETROICOR-based noise correction was performed on the odd-numbered time frames, and separately on the even-numbered time frames. In addition, the process was done on the magnitude and the phase of the data. Consequently, four noise correction processes were performed on each voxel time series: on each of the magnitude and phase of the odd-numbered time frames, and on each of the magnitude and phase of the even-numbered frames.

Before the physiological noise correction was done on each of the odd and even phase time series, the original, full phase time series was unwrapped by adding or subtracting multiples of 2π to each time frame so that the difference between consecutive frames is less than π. This same phase unwrapping procedure was then performed again, separately on each of the odd and even time series to make the entire procedure more robust to phase jumps.

3.2.3.2 Hadamard-encoding with Physiological Noise Correction

For HDP, a non-iterative Fast Fourier Transform reconstruction was first performed on gridded spiral-in data to produce non-separated complex Hadamard-encoded slices in the image domain. Inhomogeneity correction was not performed in this step. Next, the RETROICOR-based physiological noise correction procedure was performed on each of the magnitude and phase of the odd time frames (i.e. $n = 1, 3, 5, \ldots$), then on each of the magnitude and phase of the even time frames (i.e. $n = 0, 2, 4, \ldots$).

For HDP, after physiological noise and trend correction, the data was temporally filtered with a low-pass Parks-McClellan [56] finite impulse response (FIR) filter to extract the non-alternating slices $S_{1,n}$, a process which can be represented by Equation (3.1), although in this case the filtering was not done in the Fourier domain. Given an fMRI time series sampling frequency of $F_s = 1/\text{TR}$, equal to 1 Hz in this work, a desired passband edge of $0.5\left(\frac{F_s}{2}\right)$, stopband edge of $0.82\left(\frac{F_s}{2}\right)$, passband amplitude deviation of 1%, and stopband amplitude deviation of 0.1% were used to produce a 17 tap FIR filter with frequency and step response given in Figure 3.3. This resulted in a frequency of approximately $0.633\left(\frac{F_s}{2}\right)$ at 50% magnitude. After filtering, the first 8 time frames were thrown out due to ringing, as portrayed in the step response plot in Figure 3.3, and also to compensate for the group delay introduced by the filter.

By using a temporal filter with cutoff greater than $0.5\left(\frac{F_s}{2}\right)$, the temporal resolution of Hadamard-encoded fMRI with two simultaneous slices is increased compared to a conventional non-SMS fMRI scan. In general, this does not remove desired frequency components in the time series. As seen in Figure 3.4, which shows the magnitude spectrum of a Hadamard-encoded voxel time series, the majority of the signal energy for each slice is concentrated in a relatively narrow band around 0 and $0.5F_s$. In this work, a sampling frequency of $F_s = 1$ Hz was used for the Hadamard scans, so the typical frequency band of brain activation that occurs around 0 to 0.06 Hz is

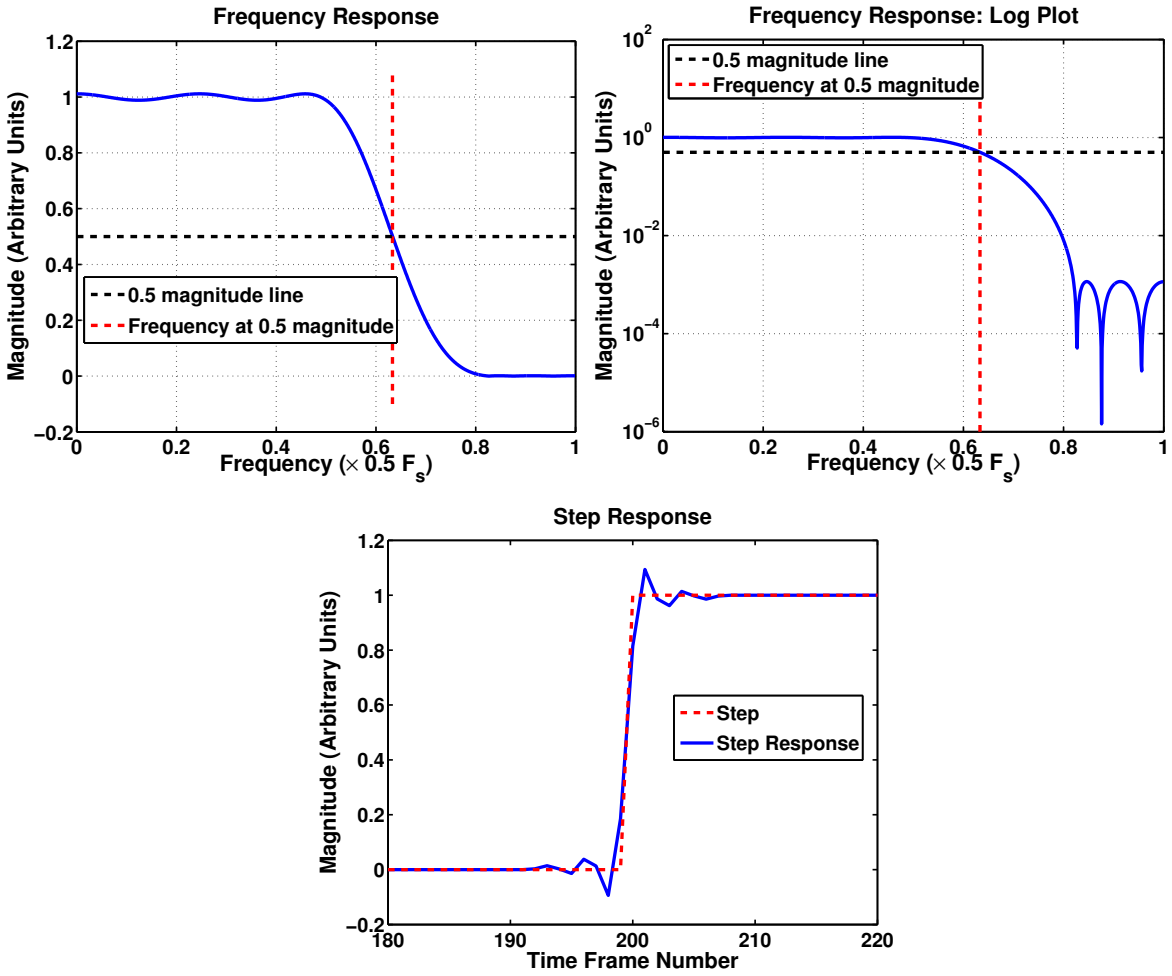

Figure 3.3: Frequency and step response of the low-pass Parks-McClellan FIR filter used to extract the simultaneous slices in Hadamard-encoded fMRI. The filter is 17 taps long, and the sampling frequency of the fMRI scan is $F_s = 1$ Hz.

very close to each of the two peaks in Figure 3.4. Depending on the sharpness of the filter transitions, filters with cutoffs up to $0.8\left(\frac{F_s}{2}\right)$ can potentially be used for even greater temporal resolution.

To extract the alternating slice $S_{2,n}$, the time series data was first modulated by $i(-1)^{n+1}$, then low-pass filtered using the same Parks-McClellan FIR filter described above. Again, this process can be described using Equation (3.2), except that the filtering was not done in the frequency domain.

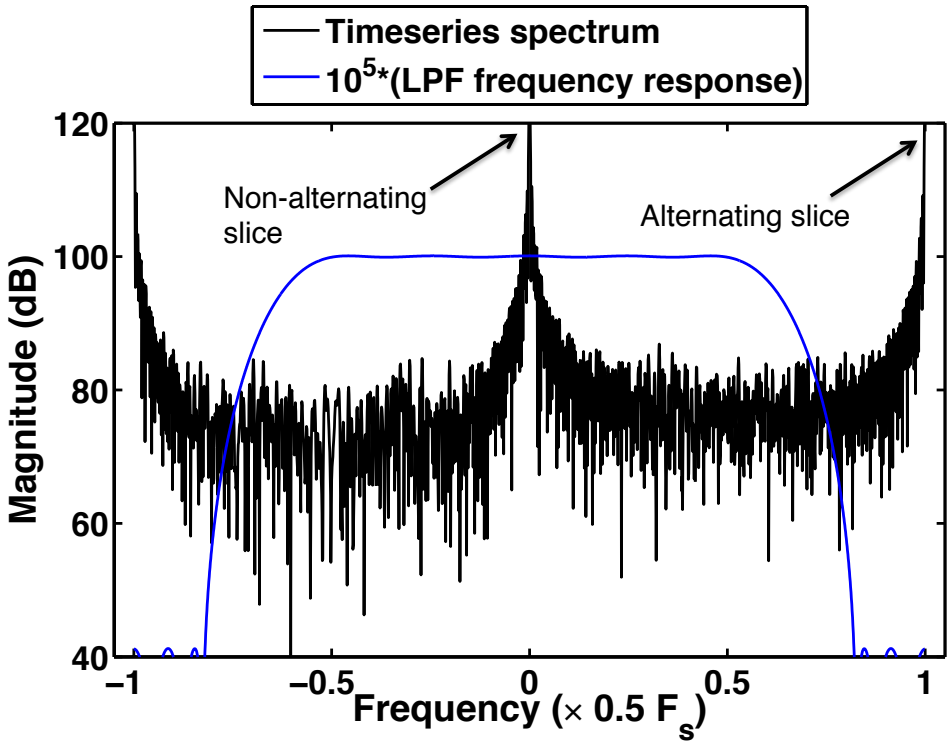

Figure 3.4: Example magnitude spectrum of a non-separated voxel time series in Hadamard-encoded fMRI with two simultaneous slices. In this work, the sampling frequency of the Hadamard-encoded fMRI scan is $F_s = 1$ Hz.

3.2.3.3 Hadamard-encoding without Physiological Noise Correction

In order to examine the effect of physiological noise removal on Hadamard-encoded fMRI, the same Hadamard-encoded SMS data was processed without physiological noise correction (HD). For HD, the raw k-space data was again gridded and Fast Fourier Transformed without B_0 inhomogeneity correction. Next, linear, quadratic, and cubic trends were removed from the time series data using linear regression and subtraction. Similar to what was described above in Section 3.2.3.2, this detrending process was performed on each of the magnitude and phase of the odd and even-numbered time frames. For the phase time series, the same phase unwrapping procedure was done before detrending on the phase as described above in Section 3.2.3.2. Finally, the same Parks-McClellan FIR filter was used to extract the slices.

3.2.3.4 Conventional Non-SMS Comparison

For the conventional non-SMS fMRI comparison, the data was processed with (CNP) and without (CN) physiological noise correction. Like the Hadamard-encoded data, the non-SMS spiral-in data was first transformed using gridding and Fast Fourier Transforms without B_0 inhomogeneity correction. For CNP, the same physiological noise correction and trend removal process described in Section 3.2.3.2 was performed, except only on the magnitude and on all time frames at once. For CN, only magnitude detrending was performed.

3.2.3.5 Scan Parameters

Scans of 10 subjects were acquired with a 3 Tesla GE magnet using a visual stimulus and finger tapping block paradigm consisting of repeating cycles of 20 s of rest followed by 20 s of stimulus and tapping. Each subject was scanned once using Hadamard-encoding and once without, which served as the conventional comparison. For the Hadamard-encoded scans, twenty pairs of 3 mm slices were acquired per TR of 1 s using $T = 8$ ms RF pulses composed of summed sincs, each with $f_0 = 1$ kHz bandwidth and 8 zero-crossings. The Hadamard scans had $N = 490$ time frames and used a spiral-in readout. In addition, the Ernst [57] angle of 62° for a gray matter T_1 of 1.33 s at 3 Tesla was used for the flip angle. For the conventional scans, forty 3 mm slices were acquired per TR of 2 s using a Hamming-weighted sinc pulse with duration 8 ms and bandwidth 1 kHz. The conventional scans had $N = 245$ time frames, used the same spiral-in readout as the Hadamard scans, and used the Ernst flip angle of 77°. For both Hadamard and conventional scans, cardiac pulsations were monitored using a pulse oximeter, and respiration was monitored using an expandable belt around the subject's abdomen. In addition, an in-plane FOV of 22 cm was used with a 64×64 resolution for all scans.

3.2.3.6 fMRI Experiment Analysis

A standard general linear model (GLM) was used to compute task activation [58]. Since the temporal resolution of the processed data from the Hadamard-encoded scans is greater than that of the conventional scans, a comparison of single-threshold activation would not be fair. Furthermore, it is difficult to accurately estimate the true degrees of freedom in the time series data after the processing steps described above have been performed, especially since many steps involve regression on each of the magnitude and phase of each of the odd and even frames of the voxel time series. Ref. [59] revisits the work in Ref. [58], resulting in a method to compute t-scores without an explicit value for the effective degrees of freedom in the data. However, in order to compare t-scores from Hadamard-encoded fMRI with those from conventional fMRI, the degrees of freedom is needed to either convert to z-scores or determine different t-score thresholds with equivalent p-value. Results from any analysis involving individual thresholds will be heavily dependent on the particular threshold chosen.

3.2.3.7 Test-retest Reliability

Therefore, in order to avoid dependence on particular t-score thresholds and perform a fair comparison, the test-retest reliability [60, 61] for each of the four methods described above was determined. Because the test-retest method requires at least three replications of a scan, each of the Hadamard and conventional scans was segmented into three runs with equal length. These three segments or runs served as the replications. Activated voxel counts were calculated using t-score thresholds from 0 to 7 in increments of 0.5 on brain-like regions of interest. All slices were used, even those without regions in the visual or motor cortex. Maximum likelihood estimation was used to compute a probability of true detection p_A and a probability of false detection p_I for each threshold. The dependent likelihood function given in the Appendix of

Ref. [60] was used. Because HD and HDP both used the same data, the probabilities were jointly computed with the same proportion of truly active voxels λ. This was similarly done with CN and CNP. The dependent likelihood function was maximized using MATLAB's nonlinear program solver "fmincon" [62] with the "sqp" algorithm described in Chapter 18 of Ref. [63].

The probabilities p_A and p_I at the 15 different t-score thresholds were used to plot a receiver operating characteristic (ROC) curve for each method. In order to compare the ROC curves between methods, the area under each ROC curve for a p_I range of 4.8×10^{-5} to 0.04 was computed. In practice, fMRI analysis would not use a threshold resulting in a $p_I > 0.04$ due to too many false activations. The areas were approximated by linearly interpolating each ROC curve to p_I steps of 1×10^{-6}, then summing the rectangular areas for each step. Finally, a two-way analysis of variance (ANOVA) of the areas was performed, along with paired Tukey [64] multiple comparisons between methods.

3.2.4 Results

3.2.4.1 Activation Maps Using Hadamard-encoding for Acceleration

Figure 3.5 shows the whole-brain activation map for run 1 of the Hadamard-encoded fMRI scan of subject 3. The top set of images have had physiological noise correction applied to them (HDP), while the bottom set of images have not (HD). Both sets used the same data. The t-scores are mapped in color and thresholded at a value of 4. The underlying grayscale brain image is the actual reconstruction result from one time frame in the middle of the scan. The same time frame is portrayed in both the upper and lower set of images for HDP and HD, respectively.

Figure 3.6 shows the analogous set of activation maps for run 1 of the conventional non-SMS fMRI scan of subject 3. The color t-score maps are again thresholded at 4,

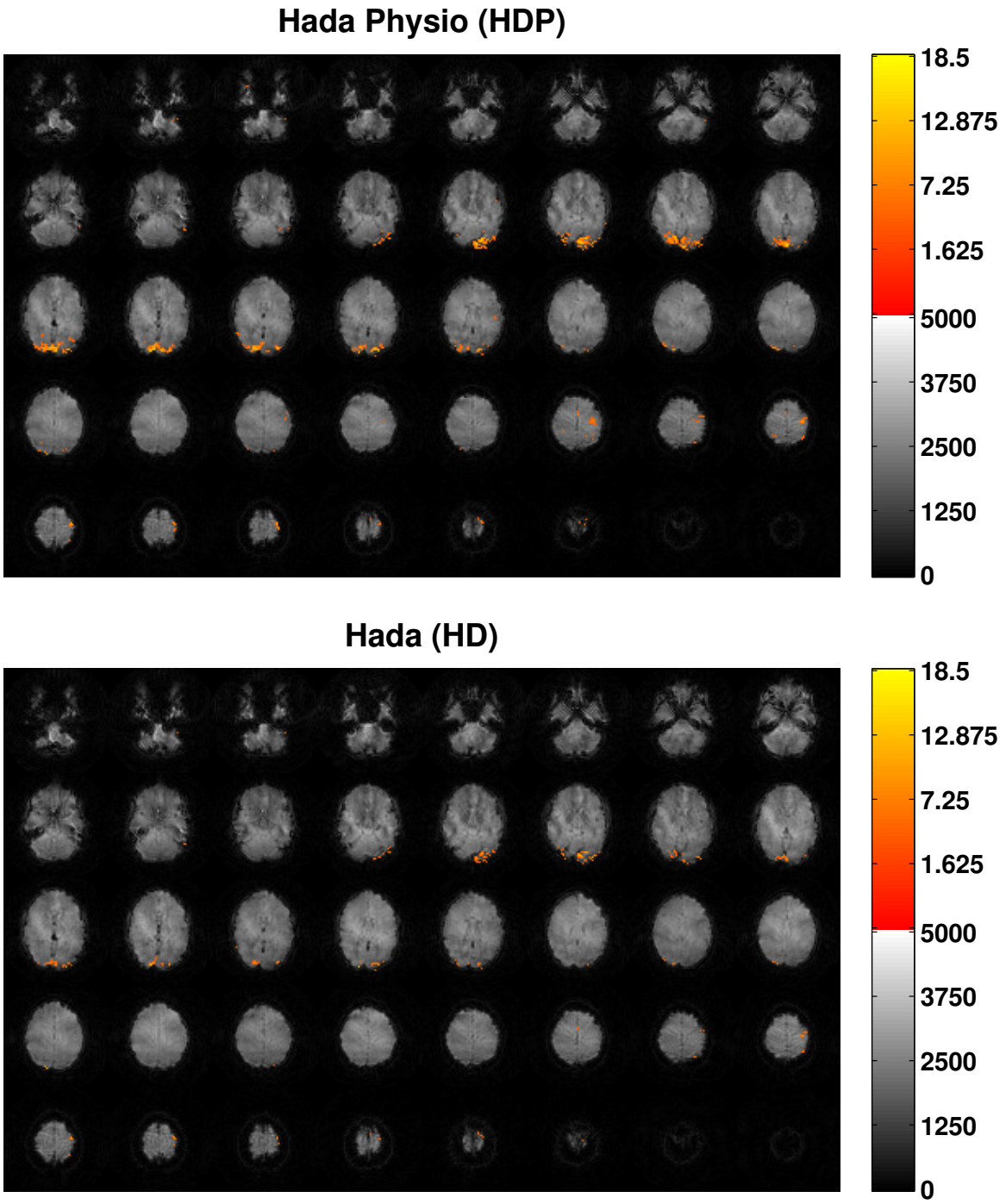

Figure 3.5: Activation maps over reconstructed images for run 1 of a Hadamard-encoded scan of subject 3, with (top) and without (bottom) physiological noise correction. A visual and motor block paradigm was used. The underlying background image is the actual result using the Hadamard reconstruction process described in Section 3.2. A t-score threshold of 4 was used.

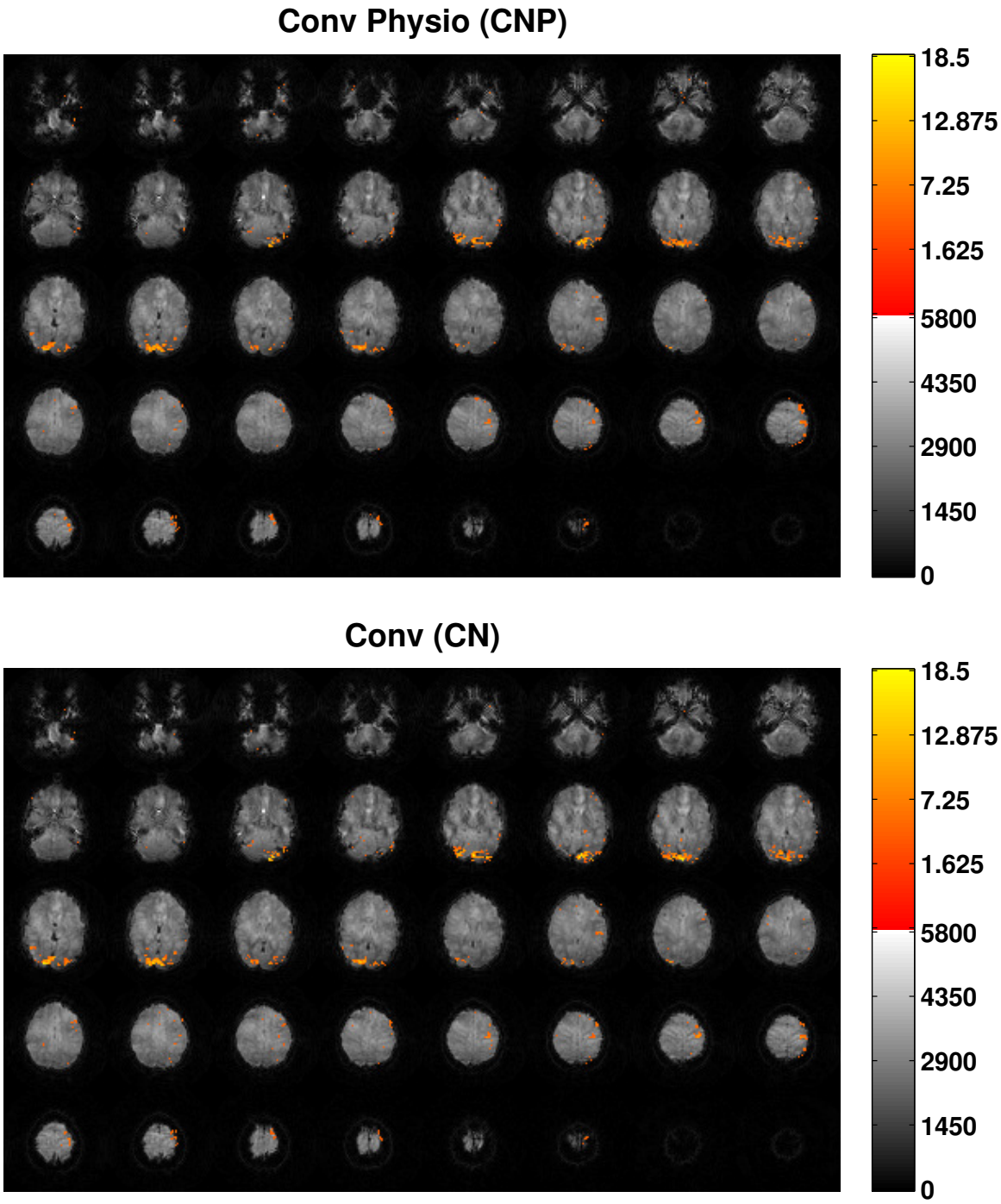

Figure 3.6: Activation maps over reconstructed images for run 1 of a conventional non-SMS scan of subject 3, with (top) and without (bottom) physiological noise correction. A visual and motor block paradigm was used. The underlying background image is the actual result using the non-SMS reconstruction process described in Section 3.2. A t-score threshold of 4 was used.

and the reconstruction result from the same time frame, located near the midpoint of the conventional scan, is portrayed as the underlying grayscale image for both CNP and CN. The t-score colorbar for Figure 3.5 and Figure 3.6 have the same scale. Due to the differences in signal intensity from different flip angles and different acquisition volumes, the grayscale bar in Figure 3.6 was adjusted to portray the brain with the same mean image brightness as in Figure 3.5.

Comparing HDP and HD in Figure 3.5, the activation areas in both the visual and motor cortices for HDP appear larger with more voxels with higher t-scores than for HD. Although the results for only one subject are shown, in general, this behavior was present in the Hadamard scans of the rest of the 9 subjects. In addition, the location of the activation areas using HDP is very similar to that using HD. The underlying brain images are very similar when comparing HDP and HD.

Comparing CNP and CN in Figure 3.6, the activation areas do not necessarily appear larger or more bright in CNP versus CN. The same can be said of the other subjects; in some subjects, the areas using CNP actually appeared smaller and less intense than in CN. However, like the Hadamard images, the underlying images using CNP appear very similar to the ones using CN.

Comparing the Hadamard images and the conventional images, the activation areas appear to be in similar locations, confirming the ability for Hadamard-encoded fMRI to localize brain activation accurately. However, the difference in activation between HDP and HD is much larger than the difference in activation between CNP and CN, suggesting that Hadamard-encoded fMRI benefited more from physiological noise correction than conventional fMRI did.

The activation is not the only visible difference between the Hadamard and conventional images; the underlying brain images look slightly different in Figure 3.5 compared to Figure 3.6. The Hadamard images in Figure 3.5 seem to have lost some of their T_2-weighted contrast between cerebral spinal fluid (CSF) and brain matter. In

the conventional images in Figure 3.6, the outline of the gyri are more visible, which is more apparent in the mid to superior slices. In general, this trend was present in the images obtained from the other subjects as well.

3.2.4.2 Test-retest Reliability of Hadamard-encoding for Acceleration

Figure 3.7 and Figure 3.8 show the mean interpolated ROC curve for each of the four methods across all 10 subjects. Figure 3.8 is the same as Figure 3.7, except with

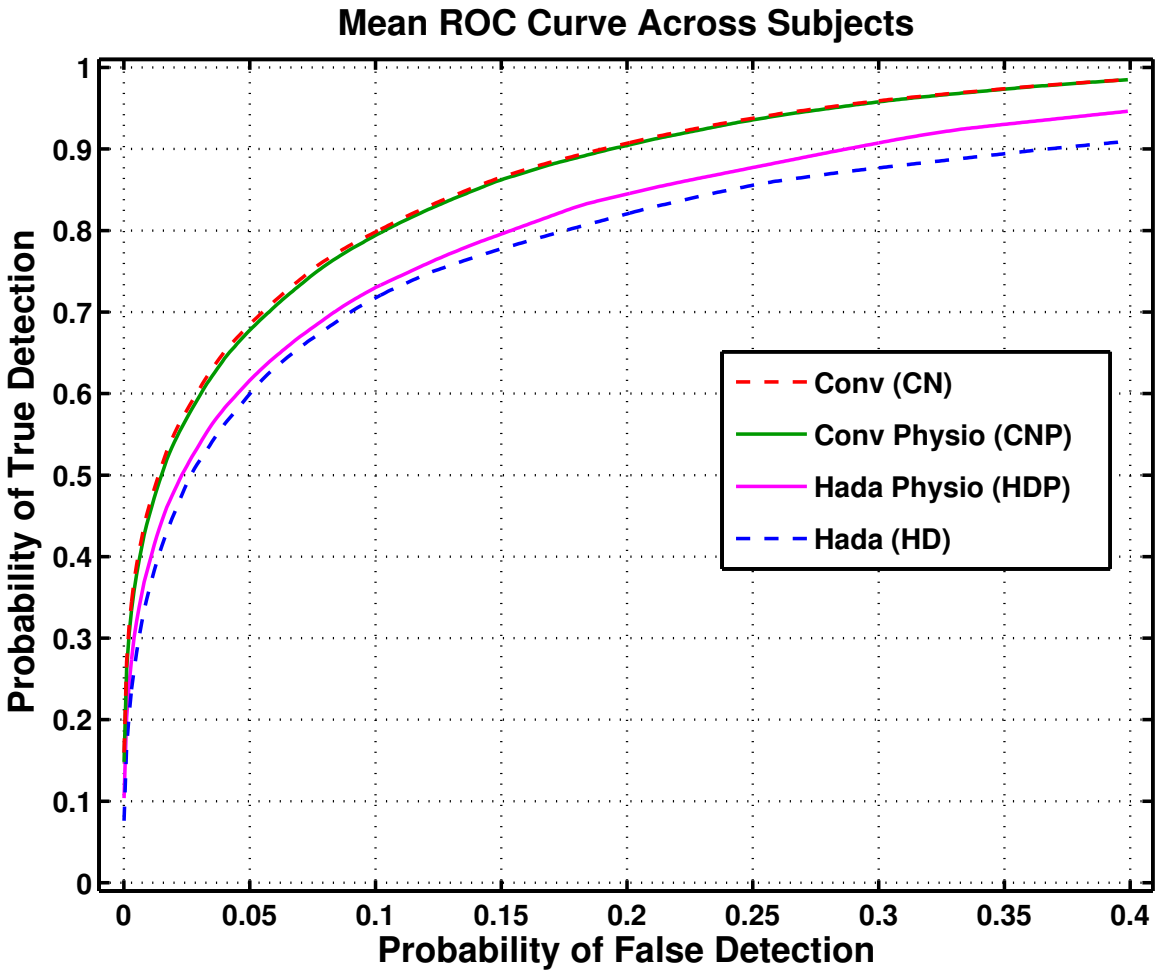

Figure 3.7: Mean ROC curve across all 10 subjects for each method. ROC curves were generated with t thresholds from 0 to 7 in increments of 0.5, then linearly interpolated to false detection probability steps of 1×10^{-6}, then averaged across subjects.

a range of false detection probabilities from 4.8×10^{-5} to 0.04, which was also the

range used to compute the areas under the curves. Qualitatively, there is not much of a difference between the two conventional methods, suggesting that conventional fMRI did not benefit much from physiological noise correction in terms of test-retest reliability. The curves for both Hadamard methods are clearly lower than the those for the conventional methods, suggesting less reliability than conventional scanning. However, the curve for HDP is higher and looks more different from HD than CNP looks compared to CN.

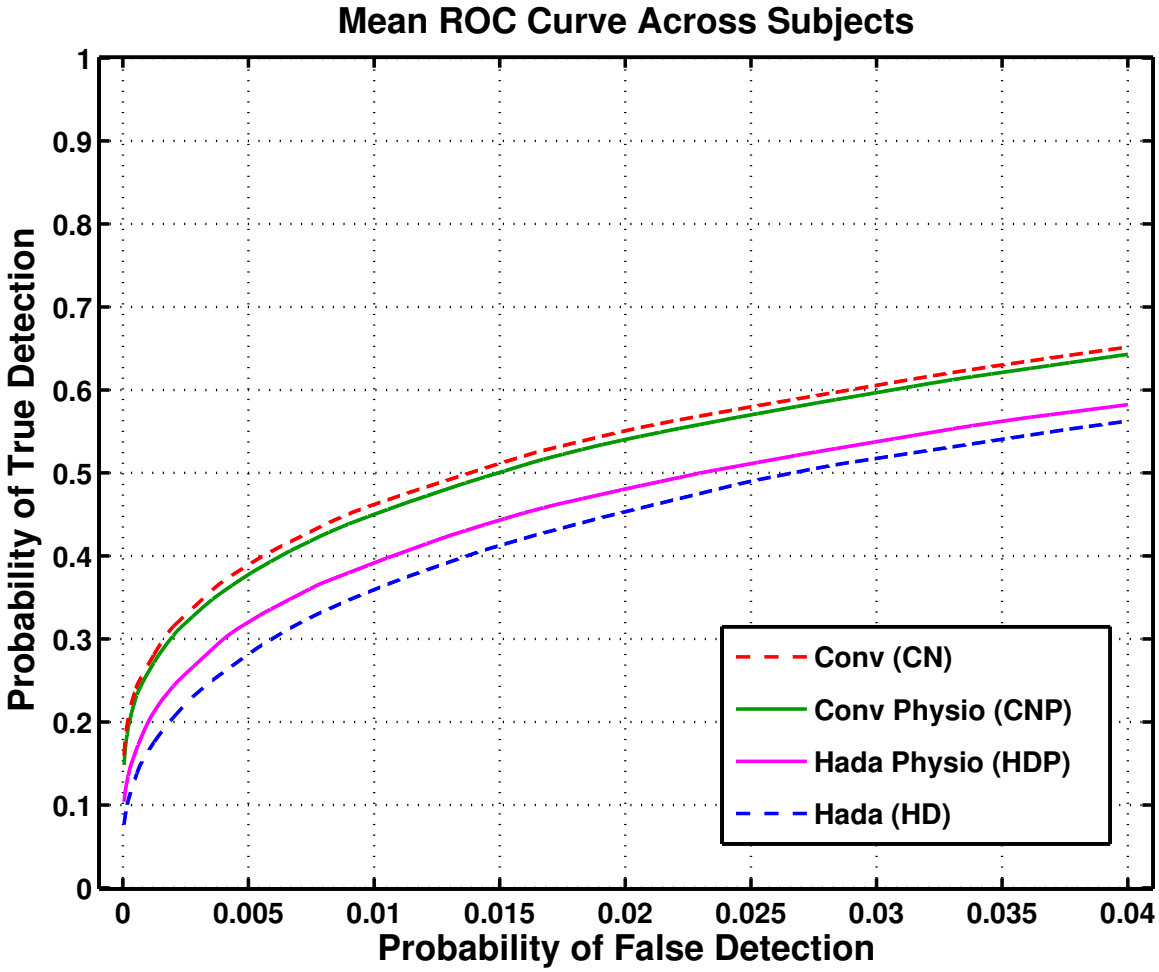

Figure 3.8: Mean ROC curve across all 10 subjects for each method. This plot is the same as Figure 3.7, except zoomed-in to a more practical range of 4.8×10^{-5} to 0.04 for the probability of false detection. ROC curves were generated with t thresholds from 0 to 7 in increments of 0.5, then linearly interpolated to false detection probability steps of 1×10^{-3}, then averaged across subjects.

In order to more quantitatively compare the ROC curves between methods, the areas under the curves for a false detection probability range of 4.8×10^{-5} to 0.04 were computed and shown in Table 3.1. The means in this table confirm what was

	Method			
	Hada	Hada Physio	Conv	Conv Physio
Subject 1	1.8797×10^{-2}	1.9619×10^{-2}	1.9958×10^{-2}	1.9069×10^{-2}
Subject 2	1.7068×10^{-2}	1.6008×10^{-2}	1.3743×10^{-2}	1.3939×10^{-2}
Subject 3	2.5302×10^{-2}	2.8582×10^{-2}	2.9562×10^{-2}	2.7414×10^{-2}
Subject 4	1.7831×10^{-2}	1.7023×10^{-2}	1.8226×10^{-2}	1.8423×10^{-2}
Subject 5	2.1257×10^{-2}	2.0544×10^{-2}	2.0050×10^{-2}	1.9572×10^{-2}
Subject 6	1.9514×10^{-2}	1.9635×10^{-2}	2.5779×10^{-2}	2.5537×10^{-2}
Subject 7	1.7619×10^{-2}	1.7148×10^{-2}	1.7913×10^{-2}	1.7760×10^{-2}
Subject 8	0.4749×10^{-2}	1.0133×10^{-2}	1.6920×10^{-2}	1.6885×10^{-2}
Subject 9	1.0043×10^{-2}	1.2975×10^{-2}	2.0261×10^{-2}	2.0092×10^{-2}
Subject 10	1.8439×10^{-2}	1.9884×10^{-2}	2.6684×10^{-2}	2.6371×10^{-2}
Mean	1.7062×10^{-2}	1.8155×10^{-2}	2.0910×10^{-2}	2.0506×10^{-2}

Table 3.1: Area under the ROC curve for false detection probabilities ranging from 4.8×10^{-5} to 0.04 for each subject and method. "Hada" indicates Hadamard-encoded fMRI, "Hada Physio" indicates Hadamard-encoding with physiological noise correction, and similarly for "Conv" and "Conv Physio" for conventional, non-SMS fMRI.

visually apparent in Figure 3.7 and Figure 3.8. However, in order to validate differences between the mean for each method, the variance across subjects needs to be determined.

Table 3.2 displays the p-values of paired Tukey [64] multiple comparisons of a two-way ANOVA of areas under the ROC curves for false detection probabilities ranging from 4.8×10^{-5} to 0.04. Figure 3.9 displays the results of the paired multiple comparisons in a different manner. The mean areas are plotted for each method with ranges equivalent to one-half the 95% confidence interval for the difference between estimated group means computed from the Tukey multiple comparison procedure. In other words, if the ranges between two methods do not overlap, then the means are significantly different with $p < 0.05$, and if the ranges do overlap, then the null hypothesis is not rejected. In Figure 3.9, the difference in means can easily be seen

Method Pair				p-value
Hada	Hada Physio			0.80
Hada		Conv		0.017
Hada			Conv Physio	0.037
	Hada Physio	Conv		0.12
	Hada Physio		Conv Physio	0.23
		Conv	Conv Physio	0.99

Table 3.2: This table displays p-values using paired Tukey multiple comparisons of a two-way ANOVA of areas under the ROC curves displayed in Table 3.1.

along with their relative positions. Larger pairwise differences between means result in a smaller p-value and conversely for smaller pairwise differences.

Using a significance of $p < 0.05$, two pairs of methods have significantly different means: HD paired with CN, as well as HD paired with CNP, with the mean for HD lower than that for either CN or CNP. This indicates that HD is significantly less reliable, or equivalently, a significantly less powerful test for a given type I error rate than either CN or CNP. However, with physiological noise correction, the reliability improves. While HDP is not significantly more reliable than HD, it is not significantly less reliable than CN or CNP since the ranges between HDP and either CN or CNP overlap in Figure 3.9. While there is a trend towards a lower p-value with the HDP and CN or CNP pairs in Table 3.2, the values are still well above 0.05. Therefore, the data suggests that with Hadamard-encoded fMRI, physiological noise correction is needed for equivalent reliability as conventional non-SMS fMRI for task based studies.

Although neither HD paired with HDP nor CN paired with CNP have mean areas that were significantly different, the p-value for HD paired with HDP is smaller than that for CN paired with CNP. Equivalently, the two conventional methods have ranges that overlap with each other more than the two Hadamard methods do in Figure 3.9. This suggests that physiological noise correction was more of a benefit for Hadamard-encoded fMRI than for conventional fMRI, which corroborates what is qualitatively

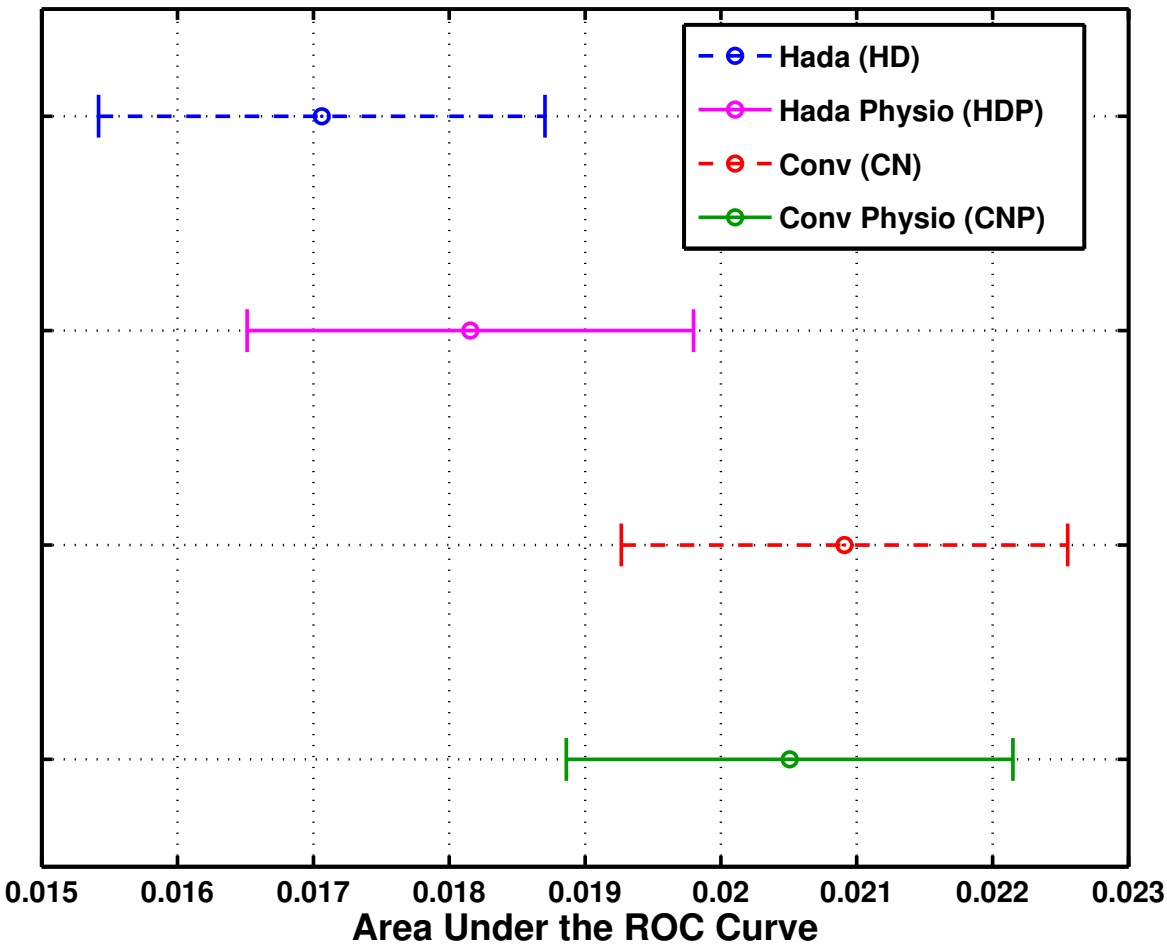

Figure 3.9: For each method, this figure plots the mean area under the ROC curve across all 10 subjects for false detection probabilities ranging from 4.8×10^{-5} to 0.04. A range around each mean is also plotted, where each range is equivalent to one-half the 95% confidence interval for the difference between estimated group means computed from the Tukey multiple comparison procedure. If the ranges for two methods overlap, there is no significant difference in mean areas, and equivalently, the p-value is greater than 0.05. If the ranges for two methods do not overlap, there is a significant difference in mean areas, and equivalently, the p-value is less than 0.05.

seen with the ROC curves in Figures 3.7 and 3.8.

3.2.5 Discussion and Conclusions

In Hadamard-encoded fMRI, simultaneous slices are distinguished from each other in the temporal frequency domain using the RF pulses, and a temporal filter is used

to extract the slices. From Ref. [65], the thermal SNR for spoiled gradient echo sequences with matching voxel volume and measurement time is given by

$$\mathrm{SNR}_0 = \frac{C}{\sqrt{\mathrm{TR}}}\sqrt{\frac{1-e^{-\mathrm{TR}/T_1}}{1+e^{-\mathrm{TR}/T_1}}}, \tag{3.12}$$

where the flip angle is assumed to be the Ernst angle, T_1 is approximately 1.33 s for gray matter, and C is a scaling constant. Assuming perfect slice separation, the Hadamard acquisition has approximately the same measurement time as a conventional non-SMS acquisition because at least two Hadamard excitations are needed to extract one slice. Substituting $\mathrm{TR}^{\mathrm{Hada}} = 1$ s and $\mathrm{TR}^{\mathrm{conv}} = 2$ s into Equation (3.12), the ratio $\mathrm{SNR}_0^{\mathrm{Hada}}/\mathrm{SNR}_0^{\mathrm{conv}}$ is approximately 1.06. Using a Monte Carlo simulation where the Parks-McClellan filter described in Section 3.2.3.2 was used for slice separation, $\mathrm{SNR}_0^{\mathrm{Hada}}/\mathrm{SNR}_0^{\mathrm{conv}}$ is approximately 1.05, which is slightly lower than the predicted value of 1.06. This is expected since the filter cutoff is $0.633\left(\frac{F_s}{2}\right)$, slightly greater than $0.5\left(\frac{F_s}{2}\right)$. Therefore, assuming perfect slice separation, Hadamard-encoded fMRI should perform at least as well as conventional non-SMS fMRI based on analysis of the thermal SNR.

However, the quality of the separation depends heavily on the temporal frequency content of each slice, as well as the behavior of the filter. Even with an ideal filter with sharp transitions and absolute suppression of stopband frequencies, physiological noise can corrupt the slice separation process if its frequency is high enough to make it into the filter's passband.

For example, respiration can cause fluctuations in the B_0 field [10, 11, 13], leading to phase variations along time. From Ref. [66], respiration-induced B_0 modulation of around 0.01 ppm at 3 Tesla, equivalent to 1.28 Hz, has been observed. For a TE of 30 ms, this results in a phase change of approximately 21.6°, a significant phase variation. A typical respiratory rate of 12 breaths per minute causes fluctuations at

a frequency of 0.2 Hz. From Figure 3.3, the frequency response still has a magnitude of around 0.6 at $0.5 - 0.2 = 0.3$ Hz, which is where 0.2 Hz fluctuations would occur if the noise was present in the alternating slice. Therefore, without physiological noise correction, respiratory noise in the alternating slice causes significant slice leakage into the non-alternating slice.

This behavior is one reason why physiological noise correction improved the reliability of Hadamard-encoded fMRI more than it did for conventional non-SMS fMRI. Although physiological noise can spuriously affect activation in conventional fMRI, it doesn't introduce additional errors of large intensity image signals leaking from one slice to another as it does in Hadamard-encoded fMRI. In addition, cardiac pulsations occur in the range of 1 to 1.6 Hz, which can alias from one slice into the frequency band of the other slice in each pair.

While physiological noise removal in Hadamard-encoded fMRI increased the mean area under the ROC curve into a range not significantly different from either conventional method, there is a slight trend towards significance with p-values of 0.12 and 0.23 when compared to CN and CNP, respectively. Visually, the range for HDP in Figure 3.9 is closer to HD than it is to either CN or CNP. The RETROICOR-based noise removal is certainly not perfect and cannot remove the entirety of all physiological noise fluctuations from the data. For example, if the subject breathes irregularly with occasional breaths deeper than normal, a low order Fourier series may not model this accurately enough for sufficient removal. The leftover respiratory fluctuation goes into a time-varying phase term in the data, corrupting the slice separation. Furthermore, even with the accelerated acquisition, the temporal sampling rate is still just 1 Hz with Hadamard-encoded fMRI, which is not typically high enough to prevent aliasing of cardiac fluctuations.

Another issue is that the stopband of the filter might not be low enough. As seen in Figure 3.3, the frequency response still has a magnitude of 0.001 at the

Nyquist frequency, which means 0.1% of the signal is leaking through. These issues could be minimized by choosing a more ideal filter with sharper transitions and lower stopband, but at the cost of increasing the length of the filter. As the length of the filter increases, additional time frames must be discarded, otherwise temporal ringing artifacts can potentially corrupt or imitate activation. Throwing away time frames reduces the degrees of freedom in the data, which is at direct odds with the goal of improving temporal resolution in fMRI. On the other hand, filtering in the frequency domain typically introduces a non-constant group delay, which can be problematic to analyze for activation.

For B_0 inhomogeneity correction, it is easier to temporally filter the k-space data, separating the slices first before transforming them into the object domain. That way a conventional non-SMS field map can be used on the separated slices in the typical manner. However, the RETROICOR-based noise correction used in this work operates in the object domain. From previously in this discussion, physiological noise has a large effect on the slice separation process, so for that reason, it was decided to transform first, perform physiological noise correction, then separate the slices in the object domain.

In order to perform B_0 inhomogeneity correction with this ordering, one could perform the initial transformation with the field map for the non-alternating slice, then perform the identical transformation with the field map for the alternating slice. Then, to extract the non-alternating slice, use only the first set of data corrected with the non-alternating slice field map, and use only the second set of data corrected with the alternating slice field map to extract the alternating slice. The disadvantage of this is that the transformation work is increased by a factor of two. However, what one would not want to do is obtain two sets of Hadamard-encoded field maps, one for the $+i$ encoding and one for $-i$, and alternate the field maps from frame to frame. This process could introduce unwanted temporal modulation on the data, corrupting

the slice separation.

Another option is to use a physiological noise correction method that operates in the k-space domain such as the method described in Ref. [13]. However, Ref. [16] has shown that retrospective corrections in k-space cannot as effectively localize physiological noise since they must operate on k-space data with high enough SNR, which involves only data from near the center of k-space. Therefore, they can undercorrect image areas with high amounts of noise such as vessels, and overcorrect areas with low physiological noise, potentially introducing spurious temporal fluctuations in the data.

However, image-based physiological noise correction is not without its own problems, especially for Hadamard-encoded fMRI. If performed on all time frames of the original data, the $+i$ and $-i$ fluctuation occurring at Nyquist frequency can be erroneously removed from the data using a noise model of aliased cardiac fluctuations. For example, with a sampling rate of $F_s = 1/\mathrm{TR} = 1$ Hz, cardiac noise at 88 beats per minute (1.47 Hz) can alias to 0.47 Hz, very close to the Nyquist frequency. The $+i$ and $-i$ fluctuation would correlate well with the modeled cardiac noise and be removed from the data. For this reason, the physiological noise correction was performed separately on each of the odd numbered time frames and even ones. However, doing this removes the benefit of increased temporal resolution for noise correction since the odd (or even) numbered frames have a TR of 2 s, which is the same as for conventional fMRI. Furthermore, since the noise correction operates on non-separated data, it cannot localize the correction to one particular slice in the pair.

One option to mitigate some of these issues is to initially perform respiratory noise correction on the full set of frames, separate the slices, then perform cardiac noise correction on the separated slices. The upper limit for a normal respiratory rate is 18 breaths per minute, which equates to 0.3 Hz. This is likely far away enough from the Nyquist frequency so that the Hadamard modulation is not removed from

the data. Although slice separation does not benefit from cardiac noise correction, diffuse phase variations are more attributed to respiratory motion [10, 11, 13] and phase fluctuations are likely the most important for slice separation. After separation, the $+i$ and $-i$ modulation is removed, and the cardiac noise can be corrected from higher temporal resolution data as well.

In conclusion, Hadamard-encoded fMRI involves distinguishing simultaneous slices from each other in the temporal frequency domain, which can be problematic because of the numerous factors in fMRI that cause undesired temporal fluctuations. The temporal resolution benefit is limited since a low-pass filter is used to separate the slices. Furthermore, the slice separation process involves alterations to the time series data, which can affect how well the underlying activation is detected. Finally, physiological noise correction on Hadamard-encoded data is not straightforward because of the need to preserve data at the Nyquist frequency. Consequently, in spite of not reaching significance, the test-retest results for Hadamard-encoded fMRI indicate that it underperforms conventional non-SMS fMRI. Based on these issues, Hadamard-encoded fMRI proved not to be a beneficial method for accelerating fMRI.

CHAPTER 4

Non-Cartesian Parallel Simultaneous Multislice fMRI[1]

The use of multiple receive coils in MRI, termed parallel imaging, has enabled high acceleration factors in SMS fMRI by taking advantage of the spatial differences between simultaneous slices in order to distinguish them. Most parallel SMS methods currently use Cartesian readouts such as EPI, partly due to the reduced complexity of the reconstruction compared to non-Cartesian readouts. However, non-Cartesian readouts such as spirals have advantages such as better signal recovery, reduced off-resonance distortion, and an increased maximum number of slices acquired per unit time. In addition, Ref. [48] has demonstrated good performance in SENSE reconstructions of blipped spiral SMS fMRI, although they did not compare it to Cartesian fMRI. This chapter explores the use of an alternative readout z-gradient in spiral SMS, an enhancement to SENSE reconstruction of SMS data, and reconstructions of non-Cartesian SMS imaging based on generalized autocalibrating partially parallel acquisitions (GRAPPA) [22].

In this chapter and the next, the term "SMS imaging" by itself will refer to parallel SMS imaging for the sake of brevity. In addition, all methods have in-plane parameters sufficient to produce a FOV of 22 cm with a resolution of 64×64 voxels. All SMS methods acquire three simultaneous slices, each 3 mm thick, using an RF

[1]Parts of this chapter are based on Refs. [67], [68], and [69].

pulse created by Equation (2.4) with $l = 3$. Finally, whenever an SMS method is compared with conventional non-SMS imaging, the non-SMS images are produced with a sinc RF pulse with the same bandwidth and duration as each of the summed sincs used in the SMS RF pulse. Furthermore, the non-SMS comparison has slice locations that match the slice locations of the corresponding SMS scan.

4.1 Methods

4.1.1 Spiral SMS with Sine Wave Modulation

Although the Fourier analysis described by Equations 2.21, 2.22, and 2.23 certainly helped in designing the blipped spiral SMS acquisition in Figure 2.6, it is not clear whether that particular blipped $g_z(t)$ scheme is optimal for slice separation using spirals. Perhaps some other blipping scheme has better performance, or maybe a different waveform altogether is optimal. Because our in-plane trajectories are spirals, which come from $g_x(t)$ and $g_y(t)$ that are "sinusoid-like," we decided to explore the use of a sinusoid for $g_z(t)$ as well, instead of the Cartesian blipping scheme done previously. Therefore, a sine wave phase modulation was implemented using a cosine $g_z(t) = 0.2994\cos(2\pi 1582t)$ G/cm, where t is in seconds. This $g_z(t)$ completes around 32 cycles over the spiral readout period of 20.224 ms. The amplitude of $g_z(t)$ was chosen to achieve a k_z trajectory that goes to $\pm k_z^{\max} \approx \pm 12.821$ m^{-1}, which was the maximum needed according to the Fourier analysis of the blipped spiral. The 3-dimensional k-space trajectory using this sinusoid z-gradient along with a spiral-in readout is shown in Figure 4.1. Figure 4.2 shows the same trajectory as Figure 4.1, except at different viewing angles. The top left image shows a "top-down" view, which is simply a spiral in the k_x-k_y plane. The middle image in the top row shows the view angled slightly more "downwards" so that the k_z variations from the sinusoid begin to become apparent. The other images have progressively lower viewing angles.

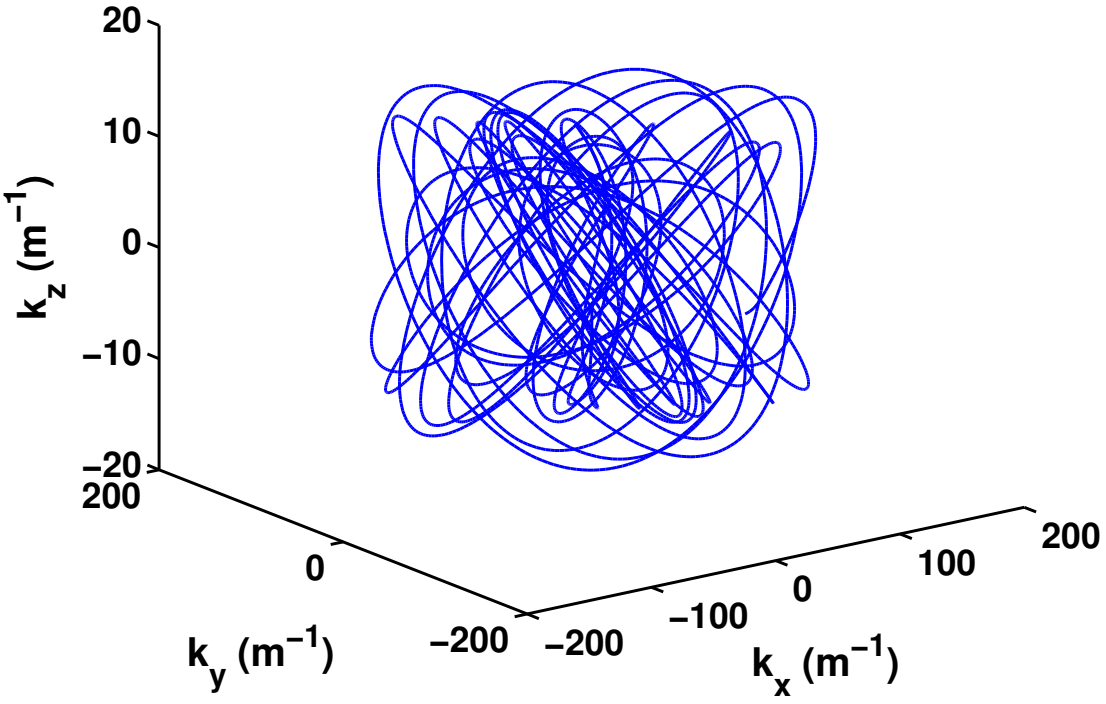

Figure 4.1: Sine wave $g_z(t)$ modulated spiral k-space trajectory used for 3 simultaneous slices.

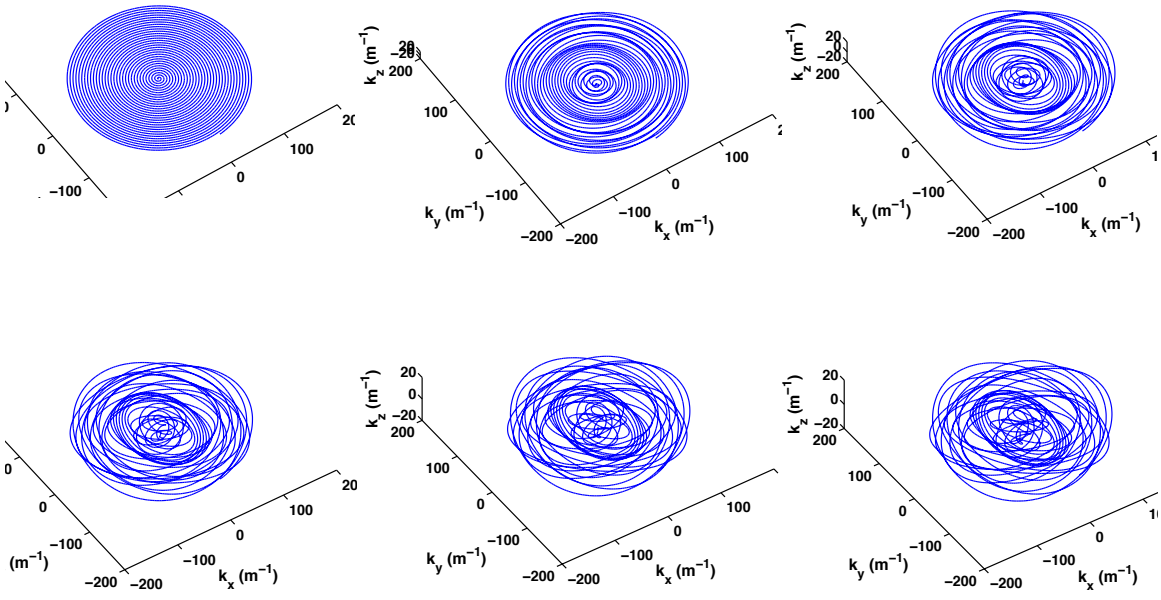

Figure 4.2: Different views of the trajectory in Figure 4.1.

4.1.2 SENSE Reconstruction

The discretized SENSE [21] reconstruction model for one acquisition of one time frame is given by

$$\begin{bmatrix} \boldsymbol{s}_1 \\ \boldsymbol{s}_2 \\ \vdots \\ \boldsymbol{s}_{n_{\text{coil}}} \end{bmatrix} = \begin{bmatrix} \boldsymbol{M}_1\boldsymbol{Q}_1\boldsymbol{C}_{1,1} & \boldsymbol{M}_2\boldsymbol{Q}_2\boldsymbol{C}_{1,2} & \cdots & \boldsymbol{M}_{n_{\text{slc}}}\boldsymbol{Q}_{n_{\text{slc}}}\boldsymbol{C}_{1,n_{\text{slc}}} \\ \boldsymbol{M}_1\boldsymbol{Q}_1\boldsymbol{C}_{2,1} & \boldsymbol{M}_2\boldsymbol{Q}_2\boldsymbol{C}_{2,2} & \cdots & \boldsymbol{M}_{n_{\text{slc}}}\boldsymbol{Q}_{n_{\text{slc}}}\boldsymbol{C}_{2,n_{\text{slc}}} \\ \vdots & \vdots & \ddots & \vdots \\ \boldsymbol{M}_1\boldsymbol{Q}_1\boldsymbol{C}_{n_{\text{coil}},1} & \boldsymbol{M}_2\boldsymbol{Q}_2\boldsymbol{C}_{n_{\text{coil}},2} & \cdots & \boldsymbol{M}_{n_{\text{slc}}}\boldsymbol{Q}_{n_{\text{slc}}}\boldsymbol{C}_{n_{\text{coil}},n_{\text{slc}}} \end{bmatrix} \begin{bmatrix} \boldsymbol{x}_1 \\ \boldsymbol{x}_2 \\ \vdots \\ \boldsymbol{x}_{n_{\text{slc}}} \end{bmatrix}, \quad (4.1)$$

where $\boldsymbol{s}_u$ is k-space data from coil u, $\boldsymbol{x}_v$ is simultaneous slice v, $\boldsymbol{C}_{u,v}$ contains the sensitivity of coil u to simultaneous slice v, $\boldsymbol{Q}_v$ is the 2-dimensional Fourier transform operator with B_0 inhomogeneity correction for slice v, $\boldsymbol{M}_v$ contains the phase imparted by the z-gradient modulation to slice v and is given by Equation (2.20), and n_{slc} is the number of simultaneously acquired slices for each SMS acquisition. For reconstruction, the $\boldsymbol{x}_v$ vector was solved for in Equation (4.1) using conjugate gradient with finite difference regularization. Because $\boldsymbol{x}_v$ contains multiple slices, the finite difference operator was constructed to only take differences within each slice and not across simultaneous slices. The $\boldsymbol{Q}_v$ matrices were implemented by a NUFFT [35, 43] with B_0 inhomogeneity correction [36]. For the spiral SMS imaging in this work, sensitivity maps were calculated using Equation (2.26).

4.1.3 Alternative Regularization Method

Instead of using the standard SENSE reconstruction described in Equation (2.24), a different way to regularize the least squares reconstruction problem is to compute

$$\hat{\boldsymbol{x}} = \arg\min_{\boldsymbol{x}} \left\{ \|\boldsymbol{A}\boldsymbol{x} - \boldsymbol{s}\|_2^2 + \beta_1 \|\boldsymbol{D}_1\boldsymbol{x}_1\|_2^2 + \beta_2 \|\boldsymbol{D}_2\boldsymbol{x}_2\|_2^2 + \ldots + \beta_l \|\boldsymbol{D}_l\boldsymbol{x}_l\|_2^2 \right\}, \quad (4.2)$$

so that each simultaneous slice, $\boldsymbol{x}_v$ has its own regularization parameter β_v. Equation (4.2) can be written in the form of (2.24) by setting $\beta = 1$ and constructing an $\boldsymbol{R}$ to perform the equivalent operation of the regularization terms in Equation (4.2). In addition, Equation (2.24) is exactly the same as Equation (4.2) if β_1, β_2, ..., β_l in Equation (4.2) are all set to the value of β in Equation (2.24). The aim behind the reconstruction in Equation (4.2) is to improve the noise reduction performance without necessarily decreasing the spatial resolution. This is done by solving for each simultaneous slice $\boldsymbol{x}_v$ separately with different β_v values for each reconstruction. For example, to reconstruct slice 2, we set β_2 to a value that would be appropriate for β in Equation (2.24), and set the rest of the parameters $\beta_1 = \beta_3 = \beta_4 = \ldots = \beta_l$ to be a relatively low value closer to 0. Experiments in this dissertation used values of 273 and 5 for this framework. The idea is that noise in the raw data or errors from model mismatch will end up in slices other than slice 2. The obvious tradeoff of this approach is that reconstruction computation is increased l-fold.

4.1.4 Spiral SMS Simulations

Non-SMS data with no readout z-gradient was acquired using a 3 Tesla General Electric MRI scanner for use in simulations of SMS data. The non-SMS scan consisted of thirty-nine 3 mm thick slices of a structured, American College of Radiology phantom, with consecutive acquisitions right next to each other. An 8-channel Invivo head coil was used for data reception, and a single-shot spiral-in readout was performed with a TE of 30 ms.

To simulate acquisitions with 3 simultaneous slices, k-space data from the appropriate individual slices were modulated with the appropriate phase from the readout z-gradient, and then simply summed together. For example, if the non-SMS acquisition has consecutive slices numbered 1 through 39, the first SMS acquisition was simulated by modulating, then summing individual slices 1, 14, and 27, the second

acquisition by modulating and summing individual slices 2, 15, and 28, and so on. Note that this process increases the amount of noise in the data compared to an actual SMS acquisition.

To illustrate the effect the z-gradient has on slice separation, an SMS simulation was performed without modulating the non-SMS k-space data before summation. In this situation, the coil sensitivities are solely responsible for slice separation.

Using the Fourier viewpoint of [41], a blipped z-gradient scheme was created so that an adequate FOV and resolution in the z-direction was attained. In this framework, $\text{FOV}_z = l\Delta z = 3(39)$ mm $= 117$ mm, $\Delta k_z = 1/\text{FOV}_z \approx 8.547$ m^{-1}, and $k_z^{\max} = \Delta k_z l/2 \approx 12.821$ m^{-1}. The 3-dimensional k-space trajectory is shown in Figure 2.6.

4.1.5 Spiral SMS Experiments

A true SMS scan was acquired with 3 simultaneous slices using a 3 Tesla General Electric MRI scanner. The slice thickness was 3 mm, and the scan consisted of 13 acquisitions of a structured, American College of Radiology phantom, with consecutive acquisitions right next to each other. An 8-channel Invivo head coil was used for data reception, and a single-shot spiral-in readout was performed with a TE of 30 ms. The same blipping scheme shown in Figure 2.6 and described in Section 4.1.4 was used during readout. A 39-slice non-SMS scan with matching slice locations was also acquired to obtain sensitivity and field maps. In addition to the blipped spiral scan, another experiment was performed using the sinusoid z-gradient of $g_z(t) = 0.2994\cos(2\pi 1582t)$ G/cm during readout, and using the same parameters as the previous experiment.

4.1.6 Concentric Ring SMS

In fMRI, efficient single-shot k_x-k_y trajectories such as a spiral-in have been recommended for fMRI due to their shorter readout times and improved signal recovery in the presence of susceptibility-induced gradients [70, 49]. However, spiral-in SMS is not well-suited for GRAPPA because of the irregularity of the sampling pattern in both the angular and radial directions. In addition, the use of a readout z-gradient [40] in SMS imaging further disrupts the regularity in a spiral readout, as shown in Figure 2.6, Figure 5b of Ref. [41], and Figure 2d of Ref. [48]. These figures show that the z-gradient blips create large gaps in each spiral platter. We propose an out-to-in concentric ring trajectory that has good sampling regularity for a GRAPPA kernel, but still retains most of the susceptibility benefits of the more established spiral-in. The concentric ring trajectory requires more samples than a spiral-in, but is still more efficient than Cartesian patterns such as EPI. In this chapter, we present a blipped, concentric-ring-in k-space trajectory with the sampling regularity necessary for implementation of slice-GRAPPA.

The out-to-in concentric ring trajectory was developed using a numerical algorithm based on Ref. [71]. As shown in Figure 4.3a, the k_x-k_y trajectory follows the path of multiple centered, concentric circles with radii spread evenly along the radial direction, along with a sample at the k-space origin. Transitions between circles follow a path created using 2 quarter-circles tangent to the main concentric rings, as shown in Figure 4.3b. All reconstruction and coil compression operations, including ones for GRAPPA, SENSE, non-simultaneous multislice imaging, and their associated field maps and calibration scans, used data obtained only in the concentric rings and origin, ignoring data sampled during all transitions. In order to provide better sampling regularity for GRAPPA, the transition paths were not started until each concentric circle was entirely complete. The numerical algorithm samples points along the k-space path with step sizes that are as a large as possible, while still satisfying

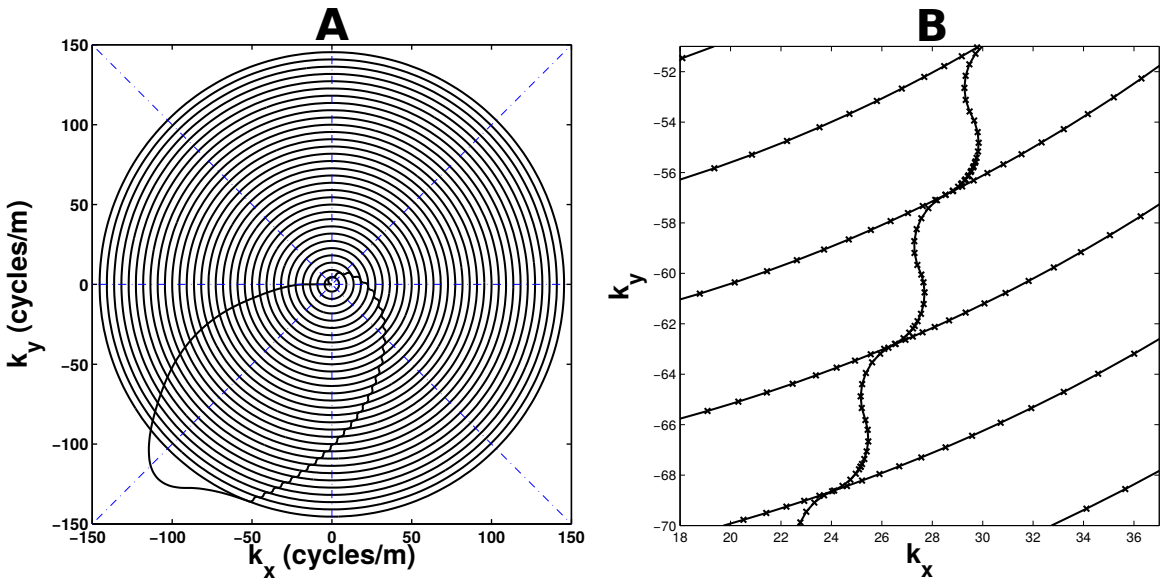

Figure 4.3: (a) k_x-k_y components of the concentric ring k-space trajectory used in this work. Boundaries of angular sectors for GRAPPA are shown with dash-dotted blue lines. (b) Close-up of ring transitions with "x" markers indicating where samples were acquired.

maximum gradient amplitude and slew rate hardware constraints. It does this by using the maximum slew rate at each step until the curvature of the path is too great. When this happens, the algorithm re-samples a previous point with a smaller step size, equivalent to backing up and slowing down the trajectory. The result is an efficient and accurate trajectory that is consistent with hardware limits.

In order to decrease the geometry factor in SMS imaging [40], z-gradient blips were used during the concentric ring readout. Using a more complicated z-gradient such as a sine wave would be problematic due to the irregularity it introduces. The z blips were timed to occur only during the k_x-k_y transitions between rings so that the entirety of each concentric ring remained in a single k_z plane, as shown in Figure 4.4. The readout z-gradient consisted of a repeating set of $(n_{\text{slc}}-1)$ positive blips followed by a rewinder negative blip and were designed according to the necessary Fourier requirements for n_{slc} simultaneously acquired slices (multiband factor), each separated by a distance of $n_{\text{acq}}d_{\text{slc}}$, where n_{acq} is the number of SMS acquisitions per TR, and

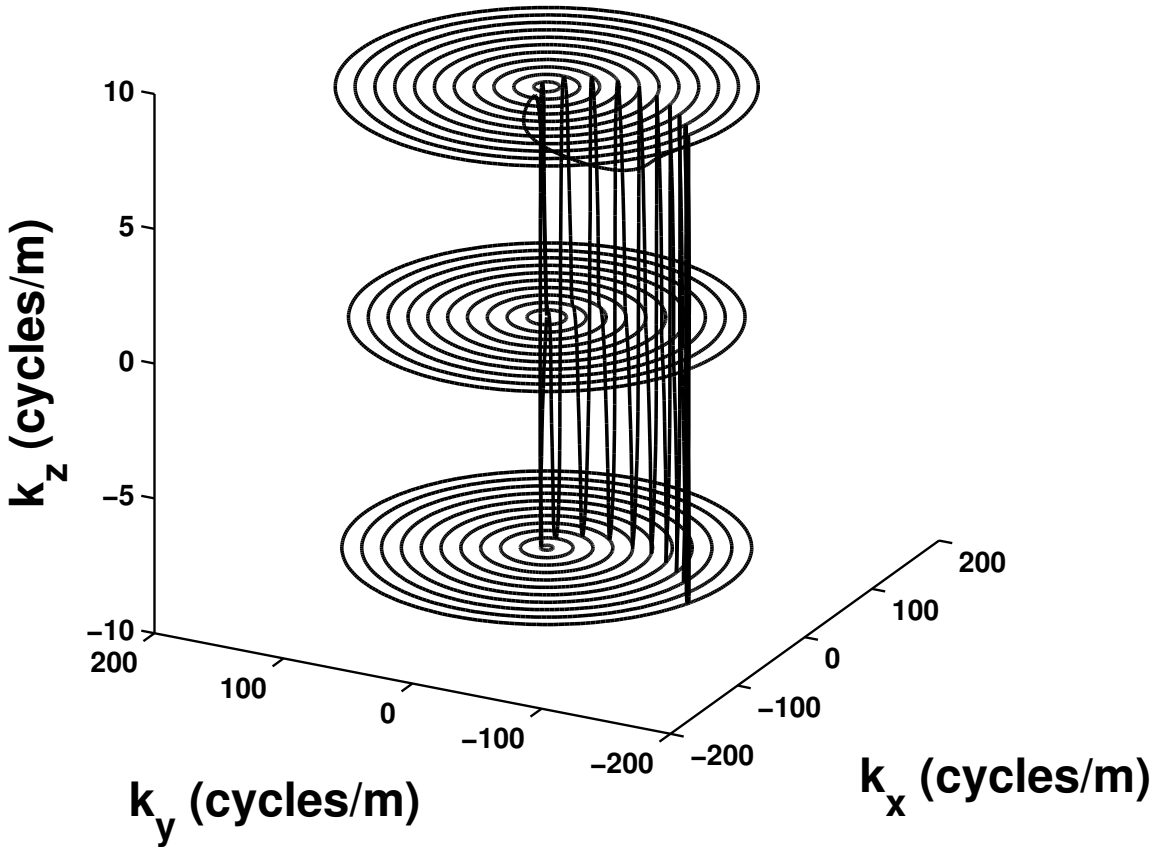

Figure 4.4: Three-dimensional concentric ring k-space trajectory for a $n_{\text{slc}} = 3$ simultaneous slice acquisition.

d_{slc} is the distance between adjacent individual slices [41]. Figure 4.5 shows the actual gradient waveforms used during readout to produce the trajectory shown in Figure 4.4. The use of tangent quarter-circles for the transition paths may not be optimal in terms of speed, but because it was desired to have the z blips entirely within each transition, the quarter-circle transitions were more than adequate to achieve the minimum time needed for each z blip.

The specifics of the concentric ring trajectory parameters used in this chapter are described in Section 5.1.6. In addition, the SMS concentric ring scans used a TR of 663 ms and a TE of 31 ms. The non-SMS concentric ring used for comparison in this

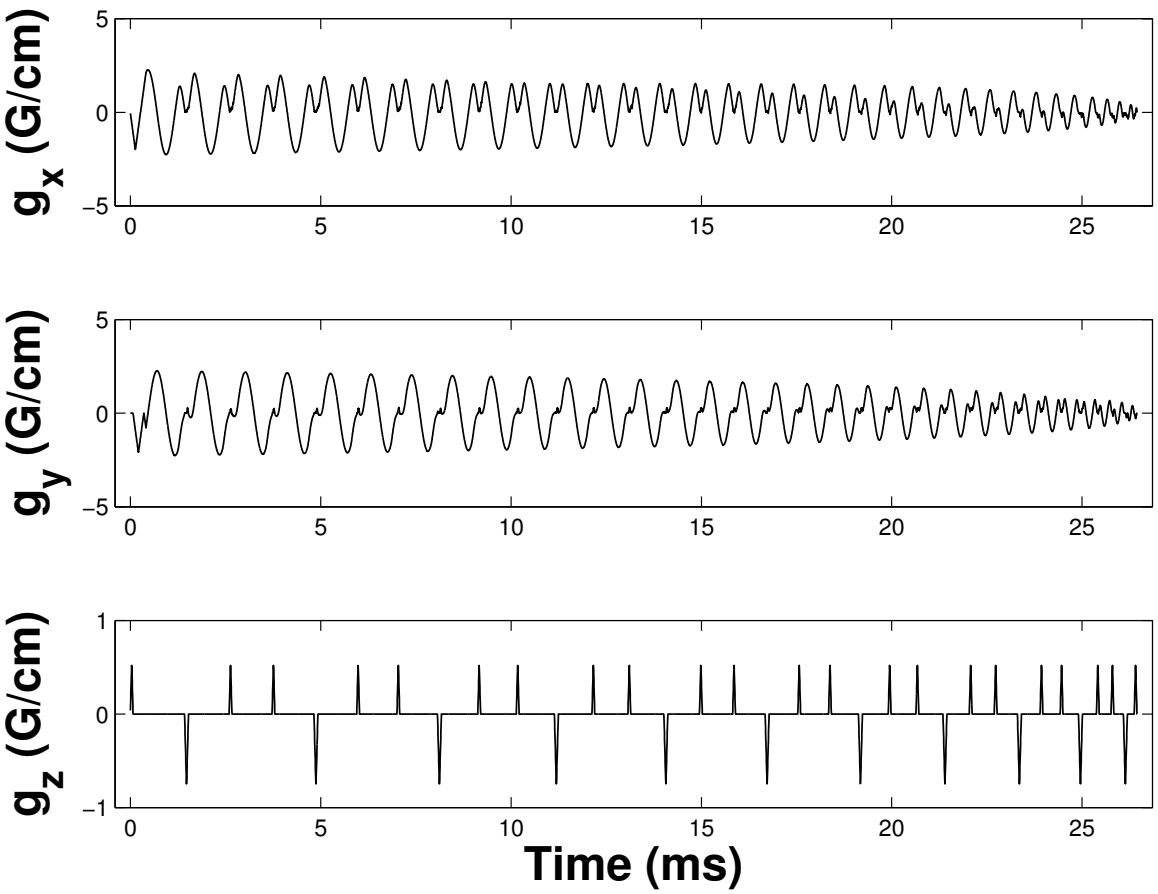

Figure 4.5: Readout gradient waveforms used to produce a $n_{\text{slc}} = 3$ simultaneous slice concentric-ring-in trajectory. The x and y gradients were designed using the numerical algorithm described in Section 4.1.6.

chapter also used a TE of 31 ms, but used a TR of 1989 ms. The specifics regarding the RF pulses used and the calibration scan are given in Sections 5.1.5 and 5.1.9.

For concentric ring SMS imaging in this work, ESPIRiT [45] was used to generate sensitivity maps from data acquired during the non-delayed field map acquisition. First, individual coil images were reconstructed with conjugate gradient using NUFFTs, inhomogeneity correction, and finite difference regularization. Then, a 2-dimensional Fourier transform was done on each coil image to obtain Cartesian k-space data. ESPIRiT was then used on this field-corrected k-space data to obtain sensitivity maps. Only the primary set of n_{coil} maps from ESPIRiT was used for all

SENSE reconstructions of concentric ring SMS imaging.

4.1.7 Slice-GRAPPA and Split Slice-GRAPPA Reconstruction

For each SMS fMRI run, a calibration scan was necessarily acquired for slice separation and reconstruction. The calibration scan consisted of non-simultaneous slices acquired at the same z locations as the SMS acquisitions. The calibration acquisitions used exactly the same k_x-k_y-k_z trajectory as the SMS acquisitions did, but with a conventional non-simultaneous RF pulse. The calibration scan used the same TR as the SMS fMRI scan to preserve image contrast and was acquired shortly before each fMRI run.

In addition to the calibration scan, field maps were obtained by acquiring non-simultaneous slices at the same z locations as the SMS acquisitions, with the same k_x-k_y concentric ring trajectory. No readout z-gradient was used for the field maps. The brain volume was acquired two times, with one time frame having an echo time delayed by 2 ms with respect to the other so that the phase difference could be used for a standard field map computation.

Prior to reconstruction, SMS data acquired at non-z-isocenter slice locations need to be demodulated so that they have the same phase modulation from the z-gradient as the isocenter SMS acquisition. For example, with an $n_{\text{slc}} = 3$ simultaneous slice acquisition taken at z-isocenter with 39 mm between simultaneous slices, a given readout z-gradient will add $\gamma z_v \int_0^t g_z(\tau)\,\mathrm{d}\tau$ amount of phase to each of the 3 slices, where $z_1 = -39$, $z_2 = 0$, and $z_3 = 39$ mm. Assuming no space between contiguous acquisitions, the adjacent set of 3 slices will be taken at $z_1 = -36$, $z_2 = 3$, and $z_3 = 42$ mm. For this non-isocenter acquisition, the data need to be modulated by $e^{i\gamma(-3)\int_0^t g_z(\tau)\,\mathrm{d}\tau}$ prior to reconstruction. This is done to ensure that all acquisitions uniformly benefit from the improved g-factor caused by the readout z-gradient.

A slice-GRAPPA (SG) reconstruction process based on Refs. [72] and [40] was developed to separate and reconstruct the SMS data. First, all acquired data from all coils were linearly interpolated to a constant angular velocity trajectory. Next, the interpolated data were divided into angular sectors as depicted in both Figure 4.3a and the lower part of Figure 4.6. Interpolated data from each angular sector were

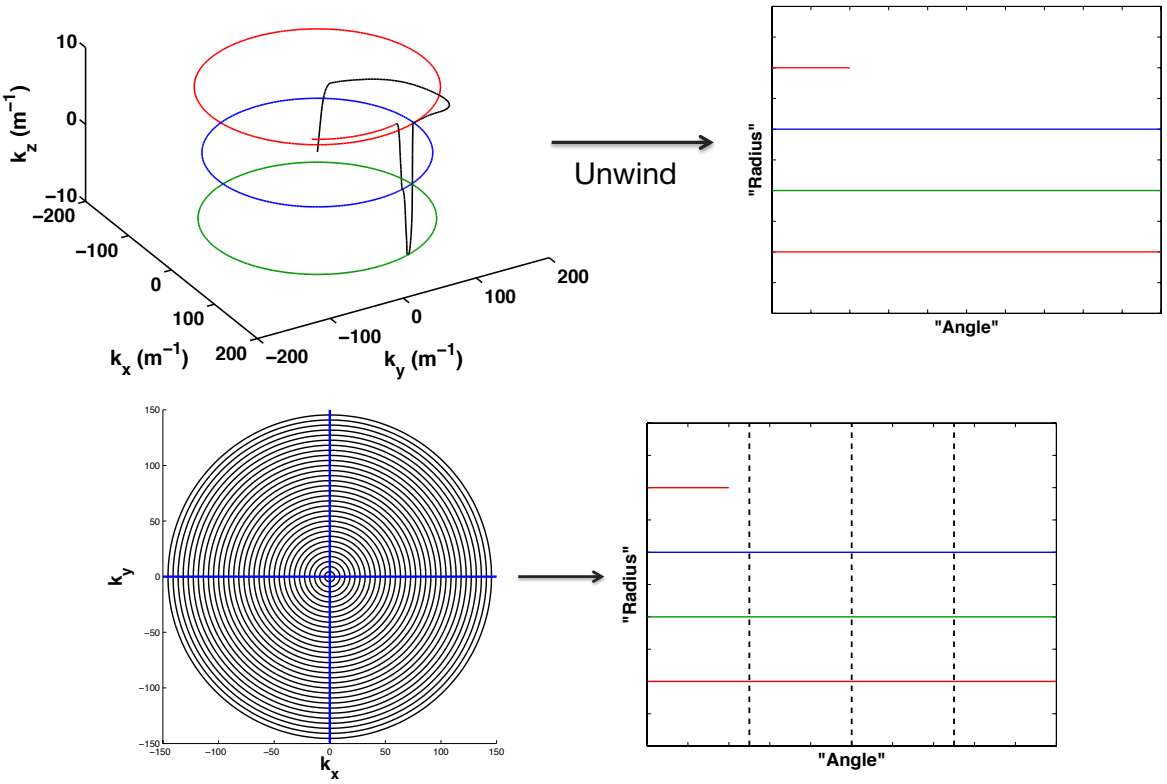

Figure 4.6: Non-Cartesian slice-GRAPPA using blipped concentric rings. The trajectory is unwinded into a Cartesian grid and divided into sectors before kernel operations are performed.

unwrapped and arranged into a Cartesian grid according to the radial and angular location of each sample as shown in the top part of Figure 4.6. SG was then applied separately to each sector according to the equation

$$\boldsymbol{S}_{\text{src}}\boldsymbol{W} = \boldsymbol{S}_{\text{trg}}, \tag{4.3}$$

where $\boldsymbol{S}_{\text{src}}$ is a "source" matrix containing interpolated data from all coils for one SMS acquisition, $\boldsymbol{W}$ is a matrix of GRAPPA kernels, and $\boldsymbol{S}_{\text{trg}}$ is a "target" matrix containing interpolated non-simultaneous calibration data, acquired at the same z locations as the SMS acquisition, and from all coils. The matrix $\boldsymbol{S}_{\text{src}}$ is constructed so that each row corresponds to a different GRAPPA kernel position or repetition, and the data from all coils is lexicographically ordered across the columns. Similarly, each row of $\boldsymbol{S}_{\text{trg}}$ corresponds to the matching kernel position for the same row in $\boldsymbol{S}_{\text{src}}$, and the calibration data from all coils is arranged across the columns for each simultaneous slice. Each column of $\boldsymbol{W}$ is a GRAPPA kernel containing weights for all coils for the corresponding column in $\boldsymbol{S}_{\text{trg}}$. The dimensions of $\boldsymbol{S}_{\text{src}}$ are n_{rep}-by-$n_{\text{kern}}n_{\text{coil}}$, those for $\boldsymbol{S}_{\text{trg}}$ are n_{rep}-by-$n_{\text{slc}}n_{\text{coil}}$, and those for $\boldsymbol{W}$ are $n_{\text{kern}}n_{\text{coil}}$-by-$n_{\text{slc}}n_{\text{coil}}$, where n_{rep} is the number of GRAPPA kernel repetitions, n_{kern} is the number of weights in the kernel for a single coil, n_{coil} is the full number of coils in the receive array, and n_{slc} is the number of simultaneously acquired slices for each SMS acquisition.

For example, using an SG kernel consisting of $n_{\text{kern}} = 4$ weights with $n_{\text{slc}} = 2$ simultaneous slices,

$$\boldsymbol{S}_{\text{src}} = \begin{bmatrix} \overbrace{s_{1,1,1} & s_{1,2,1} & s_{1,3,1} & s_{1,4,1}}^{\text{coil 1}} & \overbrace{s_{2,1,1} & s_{2,2,1} & s_{2,3,1} & s_{2,4,1}}^{\text{coil 2}} & \cdots & \leftarrow \text{rep 1} \\ s_{1,1,2} & s_{1,2,2} & s_{1,3,2} & s_{1,4,2} & s_{2,1,2} & s_{2,2,2} & s_{2,3,2} & s_{2,4,2} & \cdots & \leftarrow \text{rep 2} \\ s_{1,1,3} & s_{1,2,3} & s_{1,3,3} & s_{1,4,3} & s_{2,1,3} & s_{2,2,3} & s_{2,3,3} & s_{2,4,3} & \cdots & \leftarrow \text{rep 3} \\ \vdots & \vdots & \vdots & \vdots & \vdots & \vdots & \vdots & \vdots & \vdots & \vdots \end{bmatrix},$$

$$\boldsymbol{W} = \begin{bmatrix} \overbrace{w_{1,1,1,1} & w_{1,1,2,1} & w_{1,1,3,1} & \cdots}^{\text{simultaneous slice 1}} & \overbrace{w_{1,1,1,2} & w_{1,1,2,2} & w_{1,1,3,2} & \cdots}^{\text{simultaneous slice 2}} & \Big\} \text{source coil 1} \\ w_{1,2,1,1} & w_{1,2,2,1} & w_{1,2,3,1} & \cdots & w_{1,2,1,2} & w_{1,2,2,2} & w_{1,2,3,2} & \cdots & \\ w_{1,3,1,1} & w_{1,3,2,1} & w_{1,3,3,1} & \cdots & w_{1,3,1,2} & w_{1,3,2,2} & w_{1,3,3,2} & \cdots & \\ w_{1,4,1,1} & w_{1,4,2,1} & w_{1,4,3,1} & \cdots & w_{1,4,1,2} & w_{1,4,2,2} & w_{1,4,3,2} & \cdots & \\ w_{2,1,1,1} & w_{2,1,2,1} & w_{2,1,3,1} & \cdots & w_{2,1,1,2} & w_{2,1,2,2} & w_{2,1,3,2} & \cdots & \Big\} \text{source coil 2} \\ w_{2,2,1,1} & w_{2,2,2,1} & w_{2,2,3,1} & \cdots & w_{2,2,1,2} & w_{2,2,2,2} & w_{2,2,3,2} & \cdots & \\ w_{2,3,1,1} & w_{2,3,2,1} & w_{2,3,3,1} & \cdots & w_{2,3,1,2} & w_{2,3,2,2} & w_{2,3,3,2} & \cdots & \\ w_{2,4,1,1} & w_{2,4,2,1} & w_{2,4,3,1} & \cdots & w_{2,4,1,2} & w_{2,4,2,2} & w_{2,4,3,2} & \cdots & \\ \vdots & \vdots & \vdots & \ddots & \vdots & \vdots & \vdots & \ddots & \end{bmatrix} \vdots,$$

$$\text{and} \quad \boldsymbol{S}_{\text{trg}} = \begin{bmatrix} \overbrace{t_{1,1,1} & t_{2,1,1} & t_{3,1,1} & \cdots}^{\text{simultaneous slice 1}} & \overbrace{t_{1,2,1} & t_{2,2,1} & t_{3,2,1} & \cdots}^{\text{simultaneous slice 2}} & \leftarrow \text{rep 1} \\ t_{1,1,2} & t_{2,1,2} & t_{3,1,2} & \cdots & t_{1,2,2} & t_{2,2,2} & t_{3,2,2} & \cdots & \leftarrow \text{rep 2} \\ t_{1,1,3} & t_{2,1,3} & t_{3,1,3} & \cdots & t_{1,2,3} & t_{2,2,3} & t_{3,2,3} & \cdots & \leftarrow \text{rep 3} \\ \vdots & \vdots & \vdots & \ddots & \vdots & \vdots & \vdots & \ddots & \vdots \end{bmatrix},$$

where $s_{a,b,c}$ is the complex value of the SMS acquisition source from coil a, kernel position number b, and repetition c, $w_{a,b,c,d}$ is the complex kernel weight of source coil a, kernel position number b, target coil c, and simultaneous slice d, and $t_{a,b,c}$ is the complex value of the non-simultaneous calibration target data from coil a, slice b, and repetition c.

For each SMS fMRI run reconstructed using SG, a simulated SMS acquisition was generated for $\boldsymbol{S}_{\text{src}}$ by summing calibration slices, and the original, non-summed calibration slices were used for $\boldsymbol{S}_{\text{trg}}$. The kernels in $\boldsymbol{W}$ were then computed from $\boldsymbol{S}_{\text{src}}$

and $\boldsymbol{S}_{\text{trg}}$ in Equation (4.3) using least squares. To separate the simultaneous slices in the SMS fMRI run, the acquired data from each time frame was used for $\boldsymbol{S}_{\text{src}}$, and Equation (4.3) was used again, this time to compute k-space data for each separate slice in $\boldsymbol{S}_{\text{trg}}$.

Split slice-GRAPPA (SP-SG) [73] was also implemented and applied to each interpolated and unwrapped sector according to Equation (4.3). When computing the kernel matrix W with SP-SG, the dimensions of $\boldsymbol{S}_{\text{src}}$ and $\boldsymbol{S}_{\text{trg}}$ are different from what they were using SG. In SP-SG, the $\boldsymbol{W}$ matrix is of identical dimensions and construction as it is with SG. However, in contrast to SG, data from the non-summed calibration slices was used for $\boldsymbol{S}_{\text{src}}$. The $\boldsymbol{S}_{\text{src}}$ matrix was constructed similarly to how it was with SG, where each row corresponds to a different GRAPPA kernel position or repetition, and the data from all coils is lexicographically ordered across the columns. Calibration data from each slice were then stacked on top of each other to create a larger $\boldsymbol{S}_{\text{src}}$ matrix with dimensions $n_{\text{rep}}n_{\text{slc}}$-by-$n_{\text{kern}}n_{\text{coil}}$. The $\boldsymbol{S}_{\text{trg}}$ matrix was also constructed similarly to how it was with SG, where each row corresponds to the matching kernel position for the same row in $\boldsymbol{S}_{\text{src}}$, and the calibration data from all coils is arranged across the columns for each simultaneous slice. However, this matrix was then replicated and stacked to match the number of rows of $\boldsymbol{S}_{\text{src}}$, and appropriate entries of this larger matrix were then zeroed out so that kernel operations on slice a from $\boldsymbol{S}_{\text{src}}$ resulted in 0 for slice b in $\boldsymbol{S}_{\text{trg}}$, for $a \neq b$. The dimensions of $\boldsymbol{S}_{\text{trg}}$ using SP-SG were $n_{\text{rep}}n_{\text{slc}}$-by-$n_{\text{slc}}n_{\text{coil}}$.

For example, when computing an SP-SG kernel consisting of $n_{\text{kern}} = 4$ weights

with $n_{\mathrm{slc}} = 3$ simultaneous slices,

$$
\boldsymbol{S}_{\mathrm{src}} = \begin{bmatrix}
\overbrace{\begin{matrix} s_{1,1,1,1} & s_{1,2,1,1} & s_{1,3,1,1} & s_{1,4,1,1} \end{matrix}}^{\text{coil 1}} & \overbrace{\begin{matrix} s_{2,1,1,1} & s_{2,2,1,1} & s_{2,3,1,1} & s_{2,4,1,1} \end{matrix}}^{\text{coil 2}} & \cdots & \leftarrow \text{rep 1} \\
s_{1,1,2,1} & s_{1,2,2,1} & s_{1,3,2,1} & s_{1,4,2,1} & s_{2,1,2,1} & s_{2,2,2,1} & s_{2,3,2,1} & s_{2,4,2,1} & \cdots & \leftarrow \text{rep 2} \\
s_{1,1,3,1} & s_{1,2,3,1} & s_{1,3,3,1} & s_{1,4,3,1} & s_{2,1,3,1} & s_{2,2,3,1} & s_{2,3,3,1} & s_{2,4,3,1} & \cdots & \leftarrow \text{rep 3} \\
\vdots & \vdots & \vdots & \vdots & \vdots & \vdots & \vdots & \vdots & \vdots & \vdots \\
s_{1,1,1,2} & s_{1,2,1,2} & s_{1,3,1,2} & s_{1,4,1,2} & s_{2,1,1,2} & s_{2,2,1,2} & s_{2,3,1,2} & s_{2,4,1,2} & \cdots & \leftarrow \text{rep 1} \\
s_{1,1,2,2} & s_{1,2,2,2} & s_{1,3,2,2} & s_{1,4,2,2} & s_{2,1,2,2} & s_{2,2,2,2} & s_{2,3,2,2} & s_{2,4,2,2} & \cdots & \leftarrow \text{rep 2} \\
s_{1,1,3,2} & s_{1,2,3,2} & s_{1,3,3,2} & s_{1,4,3,2} & s_{2,1,3,2} & s_{2,2,3,2} & s_{2,3,3,2} & s_{2,4,3,2} & \cdots & \leftarrow \text{rep 3} \\
\vdots & \vdots & \vdots & \vdots & \vdots & \vdots & \vdots & \vdots & \vdots & \vdots \\
s_{1,1,1,3} & s_{1,2,1,3} & s_{1,3,1,3} & s_{1,4,1,3} & s_{2,1,1,3} & s_{2,2,1,3} & s_{2,3,1,3} & s_{2,4,1,3} & \cdots & \leftarrow \text{rep 1} \\
s_{1,1,2,3} & s_{1,2,2,3} & s_{1,3,2,3} & s_{1,4,2,3} & s_{2,1,2,3} & s_{2,2,2,3} & s_{2,3,2,3} & s_{2,4,2,3} & \cdots & \leftarrow \text{rep 2} \\
s_{1,1,3,3} & s_{1,2,3,3} & s_{1,3,3,3} & s_{1,4,3,3} & s_{2,1,3,3} & s_{2,2,3,3} & s_{2,3,3,3} & s_{2,4,3,3} & \cdots & \leftarrow \text{rep 3} \\
\vdots & \vdots & \vdots & \vdots & \vdots & \vdots & \vdots & \vdots & \vdots & \vdots
\end{bmatrix}
\begin{matrix} \\ \\ \\ \\ \\ \\ \\ \\ \\ \\ \\ \\ \\ \\ \end{matrix}
\begin{matrix} \\ \\ \\ \text{slice 1} \\ \\ \\ \text{slice 2} \\ \\ \\ \text{slice 3,} \\ \\ \\ \end{matrix}
$$

$$
\boldsymbol{S}_{\mathrm{trg}} = \begin{bmatrix}
\overbrace{\begin{matrix} t_{1,1,1} & t_{2,1,1} & t_{3,1,1} & \cdots \end{matrix}}^{\text{slice 1}} & \overbrace{\begin{matrix} 0t_{1,2,1} & 0t_{2,2,1} & 0t_{3,2,1} & \cdots \end{matrix}}^{\text{slice 2}} & \overbrace{\begin{matrix} 0t_{1,3,1} & 0t_{2,3,1} & 0t_{3,3,1} & \cdots \end{matrix}}^{\text{slice 3}} & \leftarrow \text{rep 1} \\
t_{1,1,2} & t_{2,1,2} & t_{3,1,2} & \cdots & 0t_{1,2,2} & 0t_{2,2,2} & 0t_{3,2,2} & \cdots & 0t_{1,3,2} & 0t_{2,3,2} & 0t_{3,3,2} & \cdots & \leftarrow \text{rep 2} \\
t_{1,1,3} & t_{2,1,3} & t_{3,1,3} & \cdots & 0t_{1,2,3} & 0t_{2,2,3} & 0t_{3,2,3} & \cdots & 0t_{1,3,3} & 0t_{2,3,3} & 0t_{3,3,3} & \cdots & \leftarrow \text{rep 3} \\
\vdots & \vdots & \vdots & \ddots & \vdots & \vdots & \vdots & \ddots & \vdots & \vdots & \vdots & \ddots & \vdots \\
0 & 0 & 0 & \cdots & t_{1,2,1} & t_{2,2,1} & t_{3,2,1} & \cdots & 0 & 0 & 0 & \cdots & \leftarrow \text{rep 1} \\
0 & 0 & 0 & \cdots & t_{1,2,2} & t_{2,2,2} & t_{3,2,2} & \cdots & 0 & 0 & 0 & \cdots & \leftarrow \text{rep 2} \\
0 & 0 & 0 & \cdots & t_{1,2,3} & t_{2,2,3} & t_{3,2,3} & \cdots & 0 & 0 & 0 & \cdots & \leftarrow \text{rep 3} \\
\vdots & \vdots & \vdots & \ddots & \vdots & \vdots & \vdots & \ddots & \vdots & \vdots & \vdots & \ddots & \vdots \\
0 & 0 & 0 & \cdots & 0 & 0 & 0 & \cdots & t_{1,3,1} & t_{2,3,1} & t_{3,3,1} & \cdots & \leftarrow \text{rep 1} \\
0 & 0 & 0 & \cdots & 0 & 0 & 0 & \cdots & t_{1,3,2} & t_{2,3,2} & t_{3,3,2} & \cdots & \leftarrow \text{rep 2} \\
0 & 0 & 0 & \cdots & 0 & 0 & 0 & \cdots & t_{1,3,3} & t_{2,3,3} & t_{3,3,3} & \cdots & \leftarrow \text{rep 3} \\
\vdots & \vdots & \vdots & \ddots & \vdots & \vdots & \vdots & \ddots & \vdots & \vdots & \vdots & \ddots & \vdots
\end{bmatrix}
\begin{matrix} \\ \\ \\ \text{slice 1} \\ \\ \\ \text{slice 2} \\ \\ \\ \text{slice 3,} \\ \\ \\ \end{matrix}
$$

where $s_{a,b,c,d}$ is the complex value of the non-simultaneous calibration data from coil a, kernel position number b, repetition c, and slice d, and $t_{a,b,c}$ is the complex value of the non-simultaneous calibration data from coil a, slice b, and repetition c. Note that for slice separation, Equation (4.3) is used with the original SG dimensions of $\boldsymbol{S}_{\text{src}}$ and $\boldsymbol{S}_{\text{trg}}$, with the acquired SMS data used in $\boldsymbol{S}_{\text{src}}$.

For both SG and SP-SG, data from each k-space sector were then reassembled back into their original interpolated concentric ring locations and demodulated with the negative of the phase imparted by the blipped readout z-gradient. Finally, conjugate gradient using a non-uniform fast Fourier transform (NUFFT) [35, 43] with B_0 inhomogeneity correction [36] and finite difference regularization was used to transform k-space data into coil images, and the coil images were combined using the standard square-root-sum-of-squares method. The specifics of the SG and SP-SG parameters used in this chapter are described in Section 5.1.7.

4.2 Results

4.2.1 Spiral SMS Simulation Results

Figure 4.7(a) shows the resulting SENSE reconstruction of 3 non-simultaneous slices using Equation (2.16) as a model with $l = 1$ and $d = 8$. The resulting reconstruction for one set of 3 simultaneous slices with no readout z-gradient modulation and using $l = 3$ and $d = 8$ in Equation (2.16) is shown in Figure 4.7(b). The artifacts are quite prominent when compared to the non-SMS reconstruction in Figure 4.7(a), and the absolute difference image in Figure 4.7(g) has relatively large magnitudes. The sensitivities of the 8-channel head coil shown in Figure 4.8 make it clear why the performance is so poor: the coils are physically arranged so that different axial slices have very similar coil sensitivities.

Figure 4.7(c) shows the SENSE reconstruction of blipped spiral SMS imaging. The

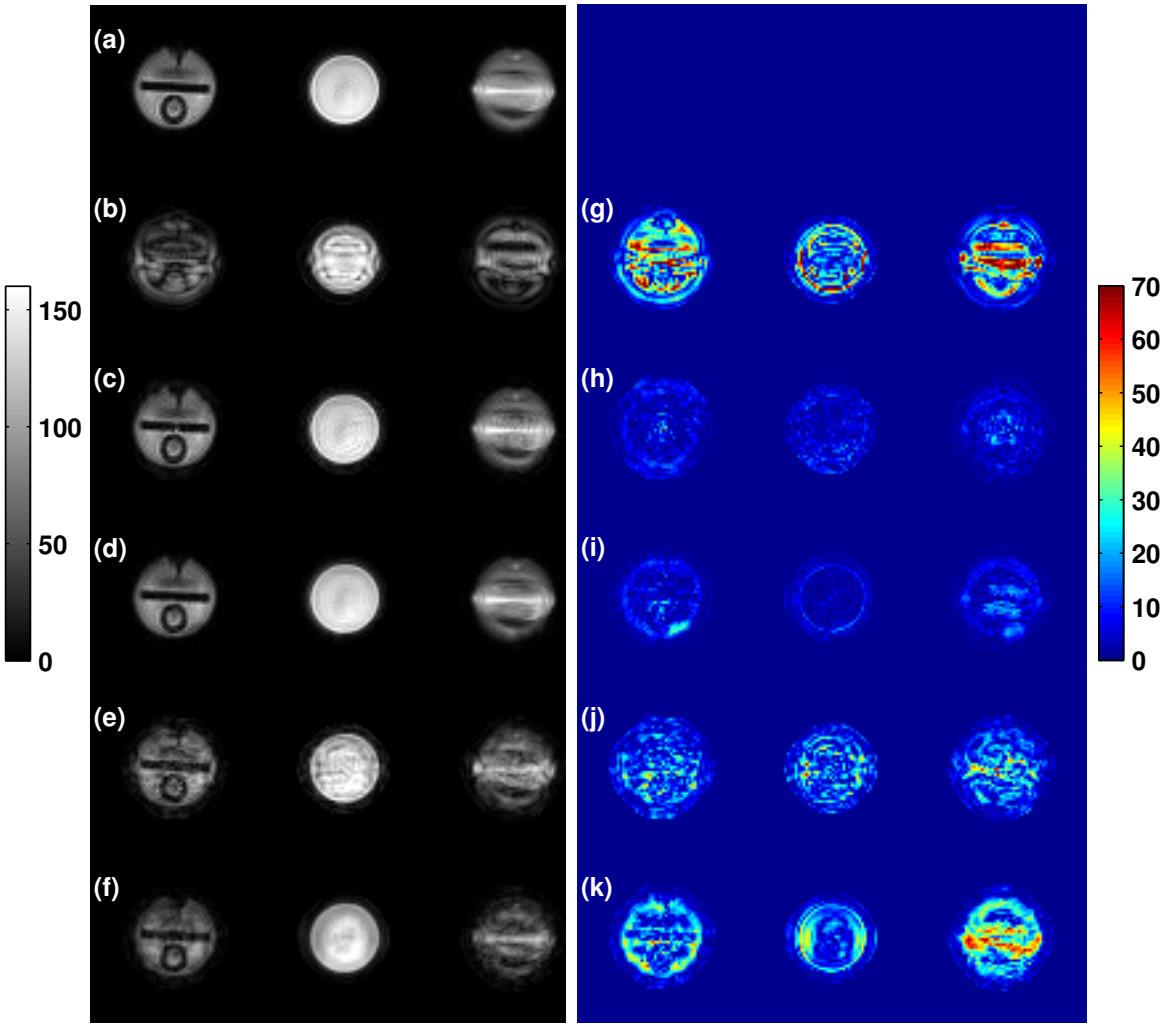

Figure 4.7: Spiral SMS simulations: SENSE method reconstructions of 3 different slices of a phantom. Non-SMS SENSE reconstruction shown in (a). SMS reconstruction without $g_z(t)$ modulation shown in (b), with blipped $g_z(t)$ modulation shown in (c), with regularization using Equation (4.2) and blipped $g_z(t)$ modulation shown in (d), with sine wave $g_z(t)$ modulation shown in (e), and with regularization using Equation (4.2) and sine wave $g_z(t)$ modulation shown in (f). On the right, (g), (h), (i), (j), and (k) are the absolute difference images of (b), (c), (d), (e), and (f), respectively, with (a).

image quality is much improved over the reconstruction without any $g_z(t)$ modulation in (b), but there are still artifacts present. In addition, there is still some residual signal in the Figure 4.7(h) difference image. These artifacts are not the result of

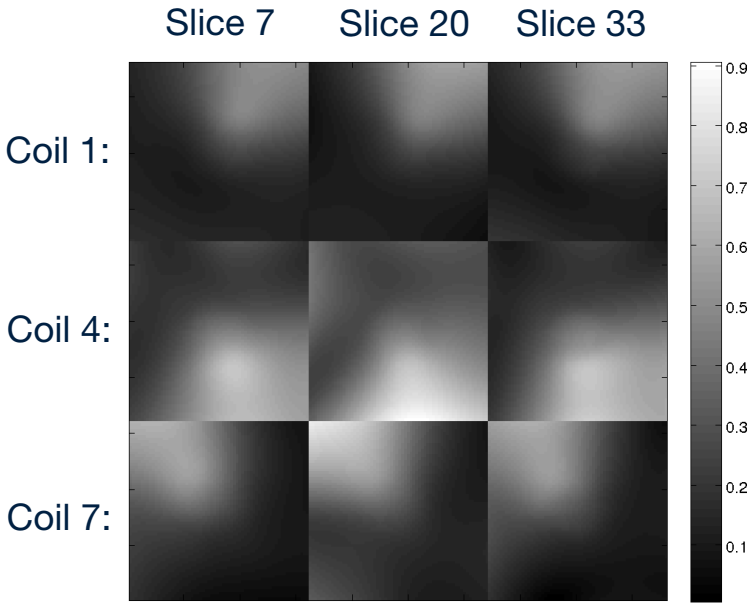

Figure 4.8: Coil sensitivities of the 8-channel Invivo head coil used for the spiral SMS simulations and experiments. Top row shows coil 1, middle row shows coil 4, and bottom row shows coil 7. Three different slices corresponding to the slices in Figure 4.7 are shown across the columns.

under-regularization because increasing β to 1500 does not remove the artifacts, and increasing β even further results in over-smoothing. Using this same simulation data, but with the reconstruction approach in Equation (4.2), the artifacts are reduced as shown in Figure 4.7(d), and the results look similar to the non-SMS images in (a). However, there does appear to be some signal loss, especially in the lower right edge of the object in each of the leftmost and rightmost slices in (d), seen more clearly in the difference image in (i). Ignoring those areas, the rest of the object seems to have errors no bigger than the ones shown in (h) for traditional regularization of blipped SMS. Any SMS reconstruction will never perfectly match the non-SMS results in (a) because there must be a penalty for the SMS acceleration. The hope is that the benefits of an increase in temporal resolution will outweigh the SNR loss for the purposes of detecting activation in fMRI.

Note that the images in Figure 4.7(d) are the result of choosing the appropriate slice out of 3 different reconstructions. The full results of all 3 reconstructions are

shown in Figure 4.9 for each of the different β combinations. The images suggest that

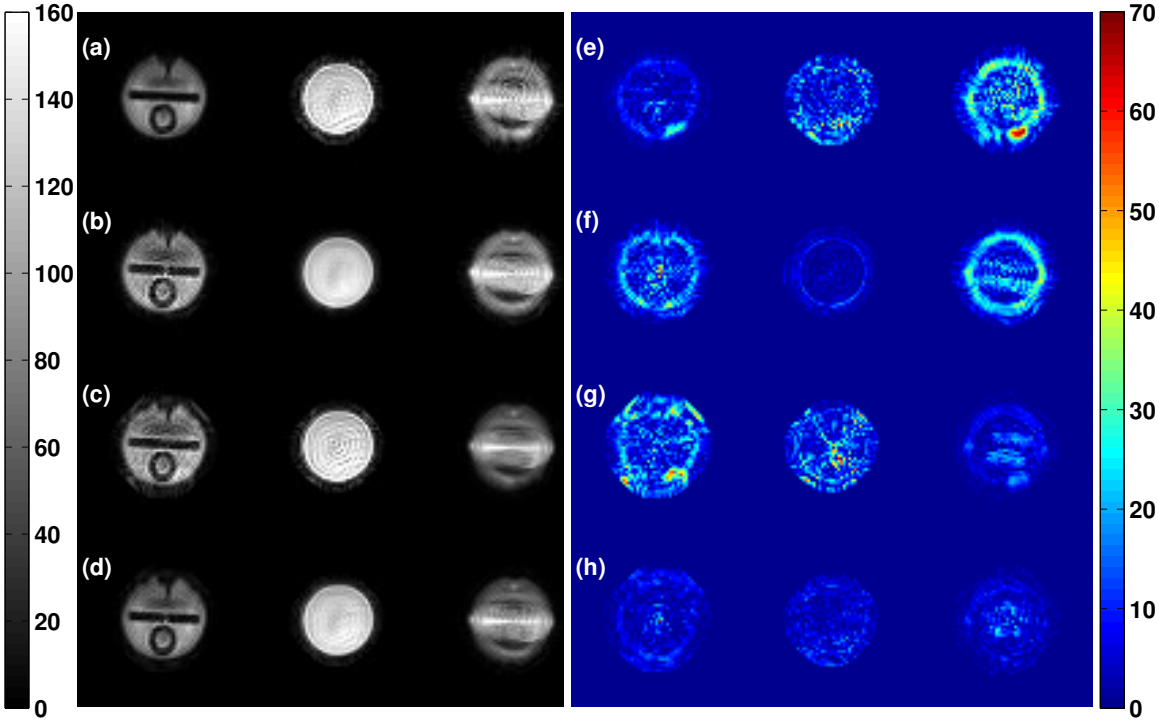

Figure 4.9: All reconstructions using all β combinations for the blipped spiral SMS simulation with regularization in Equation (4.2). (a) shows the reconstruction using $\beta_1 = 273$, $\beta_2 = 5$, and $\beta_3 = 5$, where slice 1 refers to the image on the left, slice 2 is the center image, and slice 3 is the image on the right. (b) shows the reconstruction using $\beta_1 = 5$, $\beta_2 = 273$, and $\beta_3 = 5$. (c) shows the reconstruction using $\beta_1 = 5$, $\beta_2 = 5$, and $\beta_3 = 273$. (e), (f), and (g) are the absolute difference images of (a), (b), and (c), respectively, with the original non-SMS slices used in the simulation, which are shown in Figure 4.7(a). (d) shows the reconstruction for the blipped spiral SMS simulation using traditional regularization with a single β, and is the same as the image in Figure 4.7(c). (h) is the difference image of (d), and is the same as the image in Figure 4.7(h).

the noise has been "pushed out" to the 2 slices with small β values in each case. This behavior is seen more clearly in the absolute difference images in (d), (e), and (f). In each of those images, the slices corresponding to $\beta_v = 5$ have much larger errors than the slice with $\beta_v = 273$.

The result using a spiral readout z-gradient is shown in Figure 4.7(e). The reconstruction does not work as well as the previous blipping scheme. There are significant

artifacts over all 3 slices, also seen in the difference image in Figure 4.7(j). The regularization scheme in Equation (4.2) removes some of these artifacts, as shown in Figure 4.7(f), especially for the inherently smooth center slice, but the reconstruction does not look as accurate as even the single-β reconstruction with the blipped spiral in Figure 4.7(c). However, both reconstructions in (e) and (f) are still better than the one in (b), which had no z-gradient modulation.

For each of the acquisition and reconstruction methods presented in this section, Table 4.1 shows the root-mean-square-error (RMSE) for each of the individual slices and for all 3 slices combined. A mask extending approximately 4 pixels from the edge of the object in each slice was used. The RMSE of all 3 slices was slightly higher using

Method	Slice 1	Slice 2	Slice 3	All 3 Slices
No Modulation	28.158	24.014	28.730	27.295
Blipped	6.246	5.989	5.641	5.960
Blipped with different βs	6.887	4.253	6.822	6.245
Sinusoid	13.467	15.719	15.036	14.690
Sinusoid with different βs	16.888	16.187	24.866	20.004
Blipped with $\beta_1 = 273$	6.887	13.491	18.577	13.894
Blipped with $\beta_2 = 273$	12.985	4.253	15.341	12.302
Blipped with $\beta_3 = 273$	16.259	15.014	6.822	13.200

Table 4.1: For each method, this table shows the RMSE for each of the individual slices, as well as the combined RMSE for all 3 slices in the spiral SMS simulation. The SENSE reconstruction of the non-SMS image in Figure 4.7(a) is used as the true image.

Equation (4.2) on blipped spiral SMS data compared to traditional regularization on blipped spiral data. This is likely due to the increased error in the lower right edge of the object in Figure 4.7(i). However, Equation (4.2) works quite a bit better on slice 2 of the blipped spirals as seen by the RMSE reduction in Table 4.1. Slice 2, as shown in Figure 4.7(a), has fewer sharp edges than either of slice 1 or slice 3, and is likely more similar to a slice of the brain. Although further investigation is needed, this suggests that Equation (4.2) has the potential to improve SENSE reconstruction of fMRI.

Table 4.1 also corroborates the visual appearance of the difference images in Figure 4.9; for the Equation (4.2) reconstructions of blipped spiral SMS data, slices with $\beta_v = 5$ have much higher RMSE than the slice with $\beta_v = 273$ in each case. The error in slices with $\beta_v = 5$ have RMSE that is two to three times higher than the RMSE for the corresponding slice when using traditional regularization.

Although the quantitative RMSE results indicate more errors in the reconstruction using Equation (4.2), it is worth noting that the visual results using Equation (4.2) appear subjectively better and closer to the original images in Figure 4.7(a) when compared to using traditional regularization with a single β. RMSE is only one method for quantifying image quality; a slightly higher RMSE does not always indicate that an image has worse quality.

There is another notion of the PSF, called the modulation PSF in this work. The modulation PSF is defined as the $\boldsymbol{q}$ such that $\boldsymbol{Qq} = \boldsymbol{MQe}_j$, which describes how the z-gradient perturbs a point in the image domain. Here, $\boldsymbol{Q}$ is a 2-dimensional NUFFT matrix, $\boldsymbol{M}$ is a diagonal matrix containing the phase modulation enacted by $g_z(t)$, and $\boldsymbol{e}_j$ is the jth unit vector or "point." For a slice at the z-gradient isocenter, $\boldsymbol{M}$ is the identity matrix, so $\boldsymbol{q} = \boldsymbol{e}_j$.

In order to help separate simultaneous slices, the other slices should have a modulation PSF $\boldsymbol{q}$ that has energy at a different in-plane location than $\boldsymbol{e}_j$. This way, the coil sensitivities will have a greater difference from slice to slice. For example, in [40], the blipped-CAIPI scheme effectively did a clean shift of the slices. Their $\boldsymbol{q}$ would be just a shifted $\boldsymbol{e}_j$, as shown in Figure 4.10.

For spirals, Figure 4.11 shows the modulation PSF for a slice 39 mm away from isocenter using a blipped $g_z(t)$ in (b), and using the sine wave $g_z(t)$ in (c). Figure 4.11(a) is the point used as $\boldsymbol{e}_j$ to compute the modulation PSFs and has a magnitude of 90. The other two images indicate that the blipped $g_z(t)$ has better performance because its modulation PSF has a maximum magnitude of only around 10.09

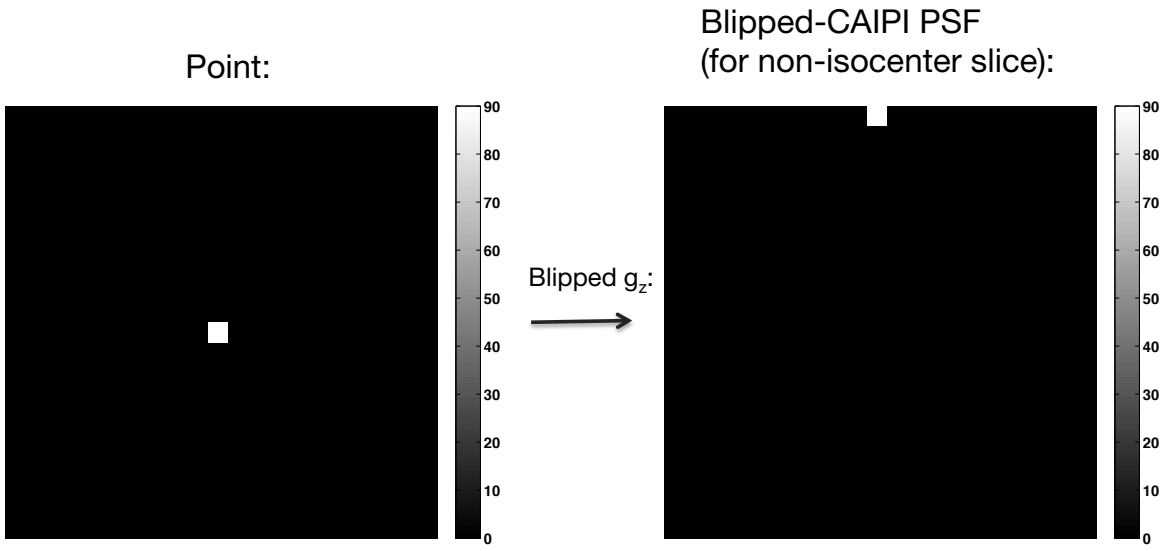

Figure 4.10: Modulation PSF using blipped-CAIPI.

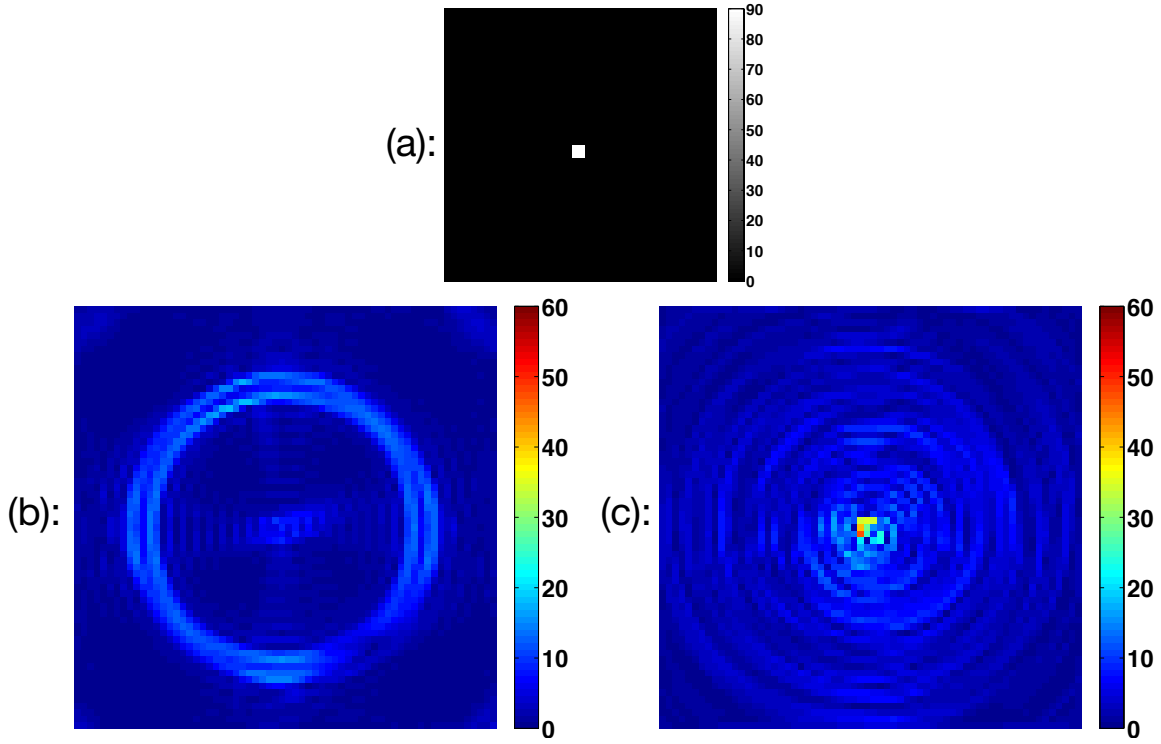

Figure 4.11: Spiral SMS: modulation PSF for a slice 39 mm away from isocenter using a blipped $g_z(t)$ in (b), and using the sine wave $g_z(t)$ in (c). The point used to computed the modulation PSFs is shown in (a) and has a magnitude of 90. The maximum magnitude in the center of (b) and (c) is approximately 10.09 and 47.1, respectively. The modulation waveforms are specified in Section 4.1.1 and Section 4.1.4.

at the jth pixel position, whereas the sine wave $g_z(t)$ has a modulation PSF with maximum magnitude 47.1 at the jth position. The blipped $g_z(t)$ modulation PSF is more "spread out" than the one for the sine wave $g_z(t)$, enabling the coil sensitivities to work better during slice separation. Figure 4.12 shows the same blipped spiral and sinusoid-modulated spiral modulation patterns using a brain image instead of a point.

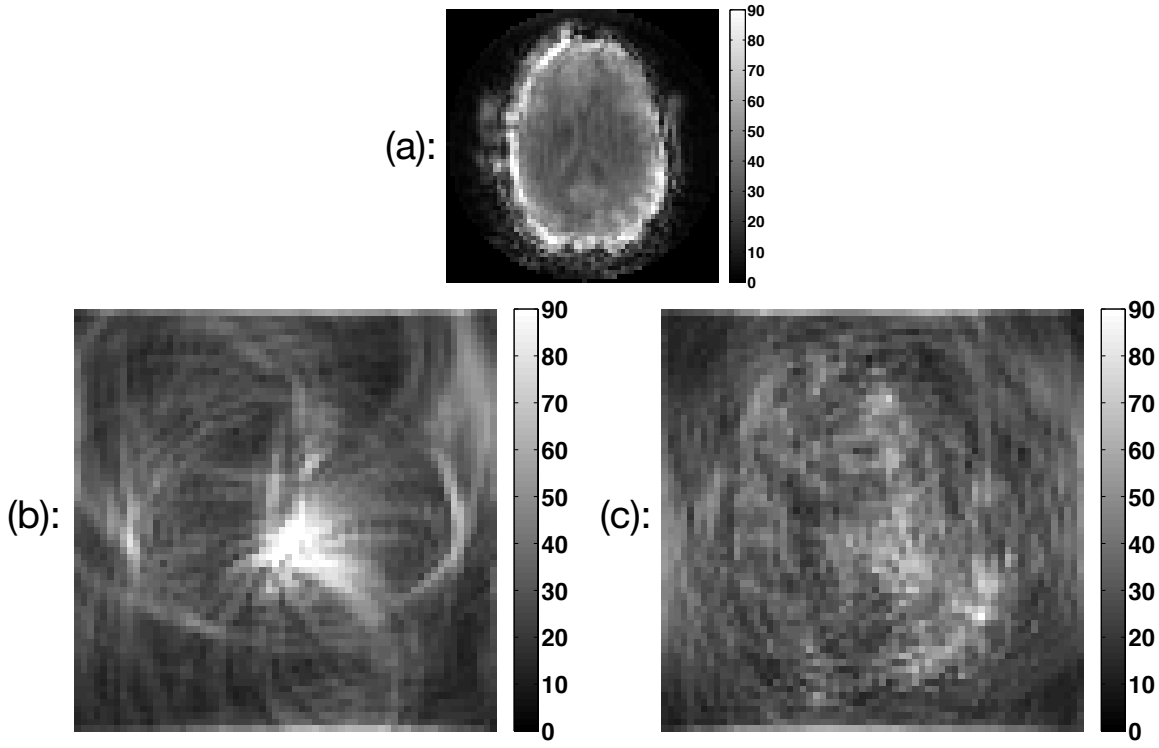

Figure 4.12: Spiral SMS: modulation pattern for a brain slice 39 mm away from isocenter using a blipped $g_z(t)$ in (b), and using the sine wave $g_z(t)$ in (c). Instead of a point, the brain image shown in (a) was used to compute the images in (b) and (c). The modulation waveforms are specified in Section 4.1.1 and Section 4.1.4.

4.2.2 Spiral SMS Experiment Results

Figure 4.13(a) shows the resulting SENSE reconstruction of the non-SMS scan using Equation (2.16) as a model with $l = 1$ and $d = 8$. The blipped spiral SMS reconstruction is shown in Figure 4.13(b), with the reconstruction using Equation (4.2) in

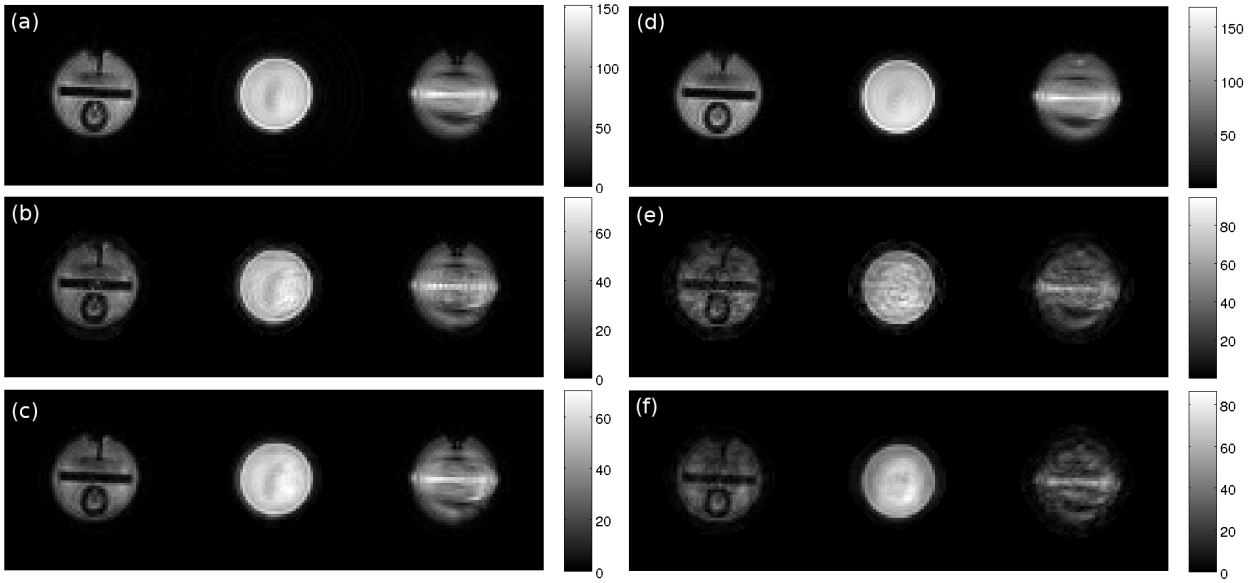

Figure 4.13: Spiral SMS experiments: SENSE method reconstructions of 3 different slices of a phantom. Non-SMS reference for blipped $g_z(t)$ shown in (a). SMS reconstruction with blipped $g_z(t)$ modulation shown in (b), with regularization using Equation (4.2) and blipped $g_z(t)$ modulation shown in (c). Non-SMS reference for sine wave $g_z(t)$ shown in (d). SMS reconstruction with sine wave $g_z(t)$ modulation shown in (e), and with regularization using Equation (4.2) and sine wave $g_z(t)$ modulation shown in (f).

Figure 4.13(c). Although the images in (c) are quite comparable to (a), there are still noticeable differences. In particular, the lower right-hand part of the slices in Figure 4.13(b) and (c) seem slightly more deformed than the other parts. This defect may have something to do with the location in k_x-k_y-space where the z-gradient blips. As seen in Figure 2.6, each of the 3 platters have a "piece" missing where the trajectory blips to another plane. Experiments using a different k_x-k_y location for z-gradient blipping resulted in similar defects, but in other parts of the images.

Figure 4.13(e) shows reconstruction results for the SMS scan with sinusoid readout z-gradient. Figure 4.13(d) shows the SENSE reconstruction of the non-SMS scan that was used to compute sensitivity and field maps for the SMS scan. Figure 4.13(f) shows results using Equation (4.2) for regularization. Much the same as the simulations, the results are not as good as those using blipped spirals; there is significant high

spatial frequency distortion throughout all three slices.

It is worth noting that, similar to the simulations, the regularization scheme in Equation (4.2) seemed to denoise the slices better than just using the same β value for all three slices. Figure 4.14 shows the full results of all three reconstructions needed to obtain the images in Figure 4.13(c). Again, it seems that in each case, noise gravitated towards slices with lower β values.

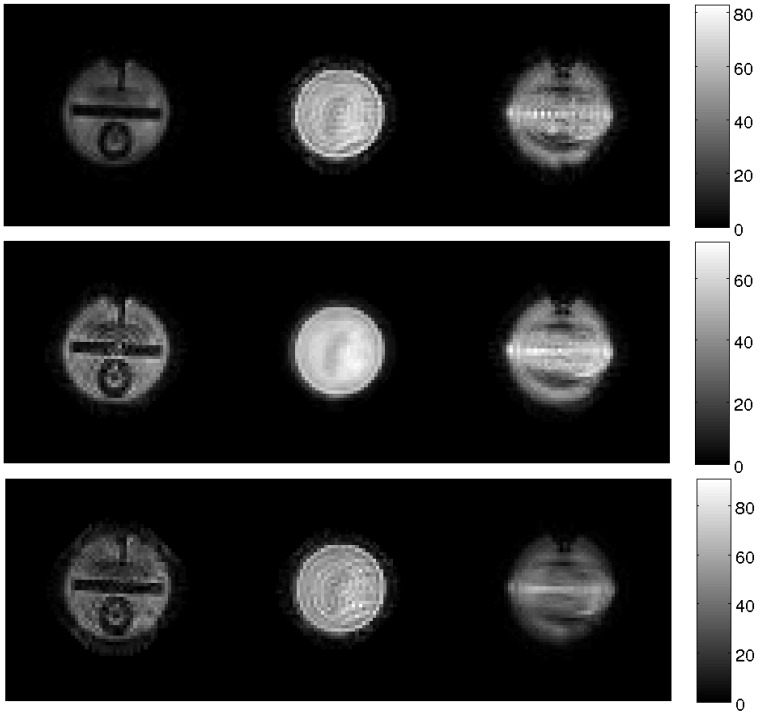

Figure 4.14: All reconstructions using all β combinations for blipped spiral SMS experiment with regularization in Equation (4.2). Top row shows the reconstruction using $\beta_1 = 273$, $\beta_2 = 5$, and $\beta_3 = 5$. Middle row shows the reconstruction using $\beta_1 = 5$, $\beta_2 = 273$, and $\beta_3 = 5$. Bottom row shows the reconstruction using $\beta_1 = 5$, $\beta_2 = 5$, and $\beta_3 = 273$. The images in the left column are slice 1, the images in the center column are slice 2, and the ones on the right column are slice 3.

4.2.3 Concentric Ring SMS Results

Figure 4.15 shows the sensitivity maps of the isocenter slice using the 32-channel coil used in the concentric ring SMS scans. Unlike the 8-channel coils shown in Figure 4.8,

there is significant variation along the through-plane direction, which should help with slice separation in SMS reconstruction. Therefore, much better performance should be expected using this 32-channel coil compared to the previous 8-channel coil.

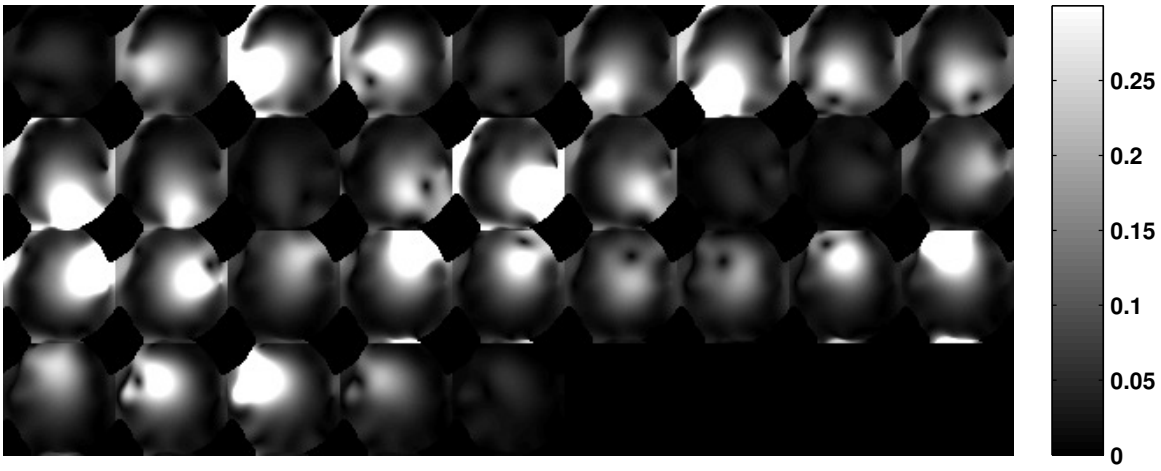

Figure 4.15: Sensitivity maps of the isocenter slice using the Nova Medical 32-channel receive head coil used for the concentric ring scans in this work.

Reconstruction of simulated concentric ring SMS imaging was performed similar to what was described in Section 4.1.4 for spiral data. However, instead of a phantom, brain images were used, as well as a blipped readout z-gradient. Figure 4.16 shows the reconstruction results using SENSE, SG, and SP-SG. Each column contains images that were acquired simultaneously; for example, the first column in Figure 4.16 contains slice 1 for the top set of images, slice 14 for the middle set, and slice 27 for the bottom. For each method, these 3 slices were acquired simultaneously. Qualitatively, the images are comparable across methods, with the SENSE images perhaps exhibiting slightly more ringing than SG or SP-SG. In addition, the more inferior slices seem to have more noise than the superior slices. The field maps used in these reconstructions are shown in Figure 4.19.

Figure 4.17 shows the corresponding absolute difference images for the images in Figure 4.16. Similar to Figure 4.16, the slice numbers are labeled at the top of

the columns, and each overall column contains slices acquired simultaneously in the simulation. Note that the errors are not distributed evenly throughout the brain; inferior slices clearly have larger errors than more superior ones. In addition, the distribution of errors within each slice varies between methods. The SENSE images contain errors in the center of the slice, whereas the SG and SP-SG images have larger areas that are cleaner. The SG and SP-SG images have trouble with specific areas such as the eyes or areas near the sinuses.

Figure 4.18 contains plots of the RMSE for the images in Figure 4.16. Within-brain masks were used for the calculation. The lowermost plot in Figure 4.18 plots the RMSE for each acquisition of 3 simultaneous slices, where acquisition 1 is defined as slices 1, 14, and 27, acquisition 3 has slices 3, 16, and 29, and so on. The results here indicate that the inferior slices do contain larger errors than the more superior ones. Interestingly, as the RMSE in the top two plots trends down, the RMSE in the third plot, for slices 27 through 39, trends up for the most part (note that slice 39 contains essentially no signal). It is unclear whether these trends are associated with each other or if the RMSE merely depends on the object shape. In other words, if one slice in a set of simultaneous slices is more difficult to reconstruct, perhaps that can affect the quality of the reconstructions of the other slices. Finally, note that the RMSE here is much smaller than the RMSE shown in Table 4.1, which is expected given the better sensitivity properties of the 32-channel coil versus the 8-channel coil.

Figure 4.20(c) shows the modulation PSF, defined in Section 4.2.1, for the blipped concentric rings. Compared to the modulation PSF of the blipped spirals shown in Figure 4.20(b), the modulation PSF for concentric rings has lower signal at the center location, indicating less overlap of simultaneous slices and better slice separation. Figure 4.21 shows the same modulation PSFs windowed lower for clarity. The modulation PSF for blipped spirals has a maximum magnitude of approximately 10.09 at the center, whereas the modulation PSF for blipped concentric rings has a maxi-

mum magnitude of 4.28 at the center. In addition, the modulation PSF for blipped concentric rings is more circularly symmetric than that for blipped spirals.

Figure 4.22 shows the modulation pattern produced by the blipped concentric ring trajectory for a $n_{\text{slc}} = 3$ simultaneous slice acquisition. Figure 4.23 shows all acquisitions in the entire volume. The modulation pattern for these figures was created in essentially the same manner as the modulation PSF described in Section 4.2.1. However, instead of using a point for $\boldsymbol{e}_j$, the images shown in Figures 4.22 and 4.23 are the $\boldsymbol{q}$ such that $\boldsymbol{Qq} = \boldsymbol{MQx}$, where $\boldsymbol{x}$ is the original, non-modulated brain slice. The middle slice, labeled slice 20 in Figures 4.22 and 4.23, is located at z-isocenter and therefore has no modulation applied to it.

Figure 4.24 shows the activation map for an SP-SG reconstruction of a visual stimulus and motor task SMS scan. All 39 slices are shown. The underlying grayscale image is the actual reconstruction result using SP-SG on one time frame. Areas in the visual and motor cortices show strong activation through multiple slices, demonstrating the feasibility of accelerated fMRI using non-Cartesian GRAPPA-based reconstruction of SMS imaging.

4.3 Discussion and Conclusions

The 3-dimensional k-space trajectory for the sine wave $g_z(t)$ is shown in Figure 4.1. The trajectory looks almost random since $g_z(t)$ is going up and down at a regular frequency, whereas $g_x(t)$ and $g_y(t)$ are going up and down faster and faster as the spiral goes in. Using the Fourier viewpoint of [41], the proper z-axis resolution is achieved since k_z goes to $\pm k_z^{\max} \approx \pm 12.821$ m^{-1}. However, a closer examination of the k_x and k_y sampling pattern that is achieved at $k_z \approx 12.821$ m^{-1}, shown in Figure 4.25, reveals that the in-plane spatial frequencies are sampled almost at random in this k_z plane and also very sparsely. It is important to obtain enough data in this k_z

plane for adequate z-axis resolution, but the sampling density is very low, especially compared to the top platter in Figure 2.6. Also, in Figure 2.6 the k-space sampling is concentrated in 3 distinct platters, which define the FOV_z, since $\text{FOV}_z = 1/\Delta k_z$. For the sine wave trajectory in Figure 4.1, much of k-space is sampled in between where the platters in Figure 2.6 would be located. This behavior is problematic in two viewpoints: the FOV_z is much too large than is necessary for the actual distance between the simultaneous slices, and the k_z plane at $k_z = 0$ is inadequately sampled, similar to the situation in Figure 4.25. The larger FOV_z is not strictly a problem *per se*, but it contributes to the issue of undersampling in k_x and k_y at the k_z planes that would benefit from denser sampling. In other words, the unnecessarily large FOV_z came at the expense of undersampling in-plane, so that much of the data is wasted.

Many of the issues with the sine wave modulation come from the fact that the SMS signal is inherently Cartesian in the z direction. In other words, a y-z plot of the SMS images would show 3 lines at 3 separate z locations corresponding to the 3 simultaneous slices. This scheme demands a distinct z resolution and FOV_z, and an increase in either would be unnecessary and would certainly come at the expense of something else. The reason why spiral sampling in the k_x-k_y plane is not inferior to Cartesian sampling in the k_x-k_y plane is because the sampling densities for the 2 patterns are comparable. The spiral pattern can easily be gridded to the Cartesian locations that have the appropriate in-plane resolution and FOV. However, the pattern in Figure 4.1 cannot be easily gridded to the distinct k_z platters in Figure 2.6 because the platters are so few and far away from each other, making the two sampling densities in k_z very different.

Equation (4.2) has the potential to improve SENSE reconstruction of SMS data by redistributing errors between simultaneous slices. The idea is that the reconstruction can be tailored to an individual slice by using different combinations of regularization parameters. Note that this method only works because of the nature of SMS

imaging; with SMS reconstruction, we have the luxury of moving errors into slices we don't care about. However, one drawback is that computation for reconstruction is increased by a factor of l for an l simultaneous slice acquisition. Given the increasing number of coils used in modern imaging, this can add a significant amount of time for reconstruction.

It is also important to note that the reconstruction using Equation (4.2) should theoretically not be a result of oversmoothing in the slice with $\beta_v = 273$. The traditional regularization method of Equation (2.24) is exactly the same as Equation (4.2) when all the regularization parameters in Equation (4.2) are set to the value of the single $\beta = 273$ in Equation (2.24). For each of the reconstructions using different β_v values, two of the slices used a value of $\beta_v = 5$, and only one used a value of $\beta_v = 273$. No slices used a value greater than 273, which suggests that no slices should be smoothed more than they would be using 273 for all slices.

The blipped concentric ring SMS results clearly outperformed the blipped spiral results, but the concentric ring data was acquired using a 32-channel coil, whereas the spiral SMS data used an 8-channel coil. Furthermore, the 8-channel coil has poor sensitivity differences in the through-plane direction. A direct comparison of blipped concentric rings versus blipped spirals would need to use the same receive hardware, along with the same amount of acceleration. However, the modulation PSF results shown in Figures 4.20 and 4.21 indicate that blipped concentric rings should have better slice separation due to less overlap between simultaneous slices. The reason why the modulation PSF for blipped spirals resulted in a larger amount of signal at the center is likely because of how the transitions between k_z planes create a gap in each spiral platter, as shown in Figure 2.6. These gaps create a block of k-space where the data is not appropriately modulated, and likely also created the slight asymmetry in the modulation PSF shown in the lower right corner of Figure 4.21(b). Also interesting is that in the blipped spiral simulation results in Figures 4.7(d)

and 4.7(i), the lower right edge of the object had the most errors. Whether this is due to the behavior of the modulation PSF remains to be determined.

An alternative reconstruction approach is to use a one-dimensional inverse Fourier transform in the through-plane direction to separate slices instead of SENSE or slice-GRAPPA. This can be done for blipped concentric ring SMS data because the simultaneous slices are fully sampled in the through-plane direction.

For a SENSE-based reconstruction using this method, in-plane SENSE is performed on each of the undersampled k_z platters in the three-dimensional k-space displayed in Figure 4.4 to produce a hybrid (x, y, k_z) space. Then, a simple l-point inverse Fourier transform is performed to separate the slices, where l is the number of simultaneously acquired slices.

For a GRAPPA-based reconstruction, in-plane GRAPPA is performed on each of the undersampled k_z platters to produce a fully sampled (k_x, k_y, k_z) space. Then, the l-point inverse Fourier transform is performed to separate the slices into a hybrid (k_x, k_y, z) space. The k-space data for each slice is then transformed into the object domain using any method the user desires. Ref. [74] presents a similar idea for 3-dimensional imaging.

However, the sensitivity maps, or calibration data in the GRAPPA case, need to be carefully prepared in order for this method to work. For SENSE, conventional non-SMS maps can be acquired and computed. However, each appropriate set of l maps corresponding to simultaneously acquired slices needs to be Fourier transformed in the through-plane direction to produce sensitivity maps in a hybrid (x, y, k_z) space. In-plane SENSE needs to use these hybrid domain (object in x and y, and frequency in z) maps in order to work. Similarly, for in-plane GRAPPA, k-space data from l calibration slices needs to be Fourier transformed in the through-plane direction into (k_x, k_y, k_z) space before it can be used to calibrate the kernel. This technique introduces an additional factor of complexity for the GRAPPA kernels since each k_z

platter has a different set of undersampled rings.

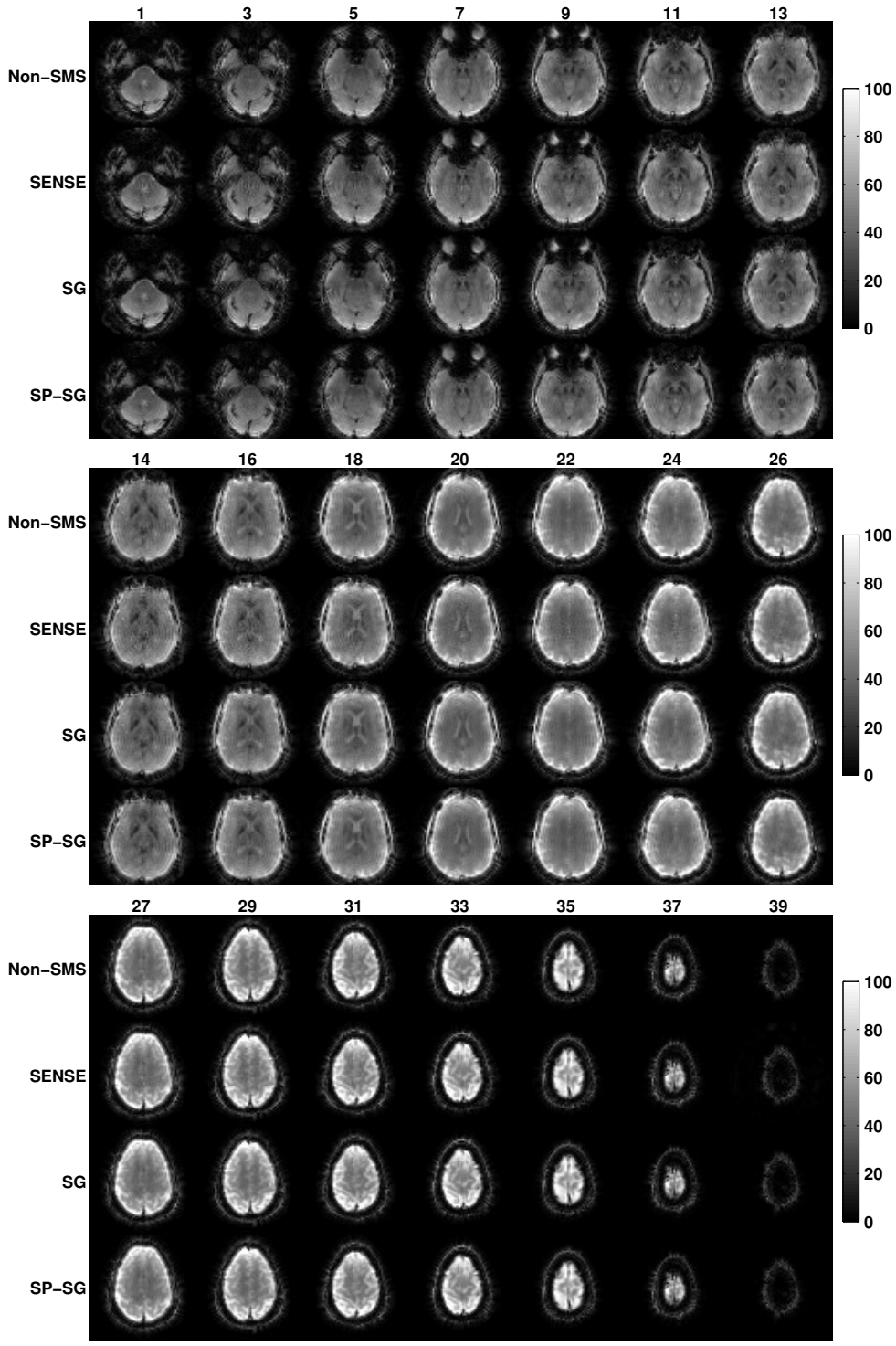

Figure 4.16: Concentric ring simulations: reconstruction results for SENSE, SG, and SP-SG, as well as the non-SMS slices used to create SMS data in the simulations. The separated, non-SMS slices are numbered consecutively from 1 to 39 starting most inferiorly and going superiorly. The number at the top of each column of images indicates the slice number for that column.

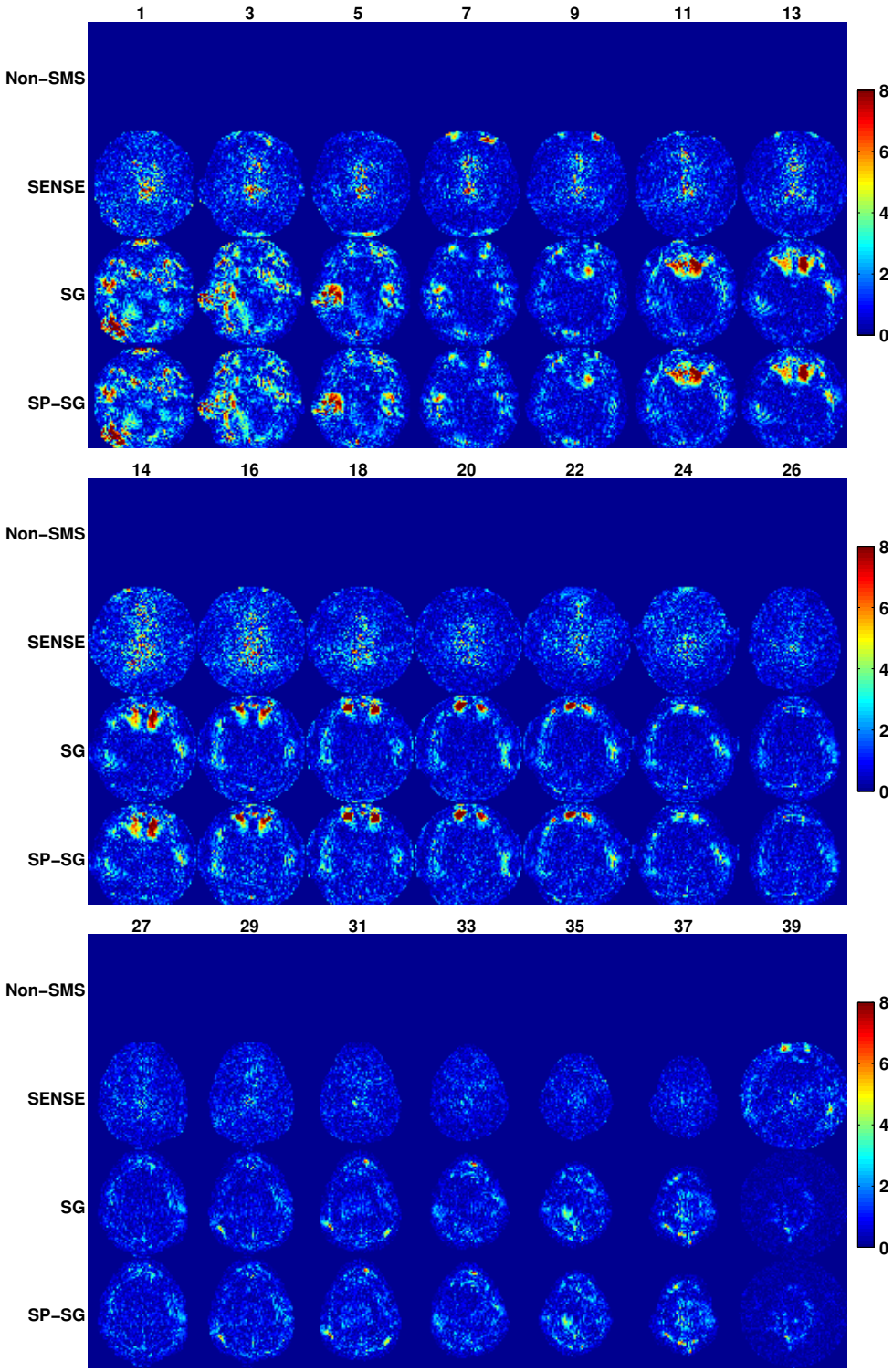

Figure 4.17: Concentric ring simulations: absolute difference images between each reconstruction method labeled on the left and the non-SMS slices used to simulate the SMS acquisition. The non-SMS slices used as the "truth" are the ones shown in Figure 4.16 labeled "non-SMS." The number at the top of each column of images indicates the slice number for that column.

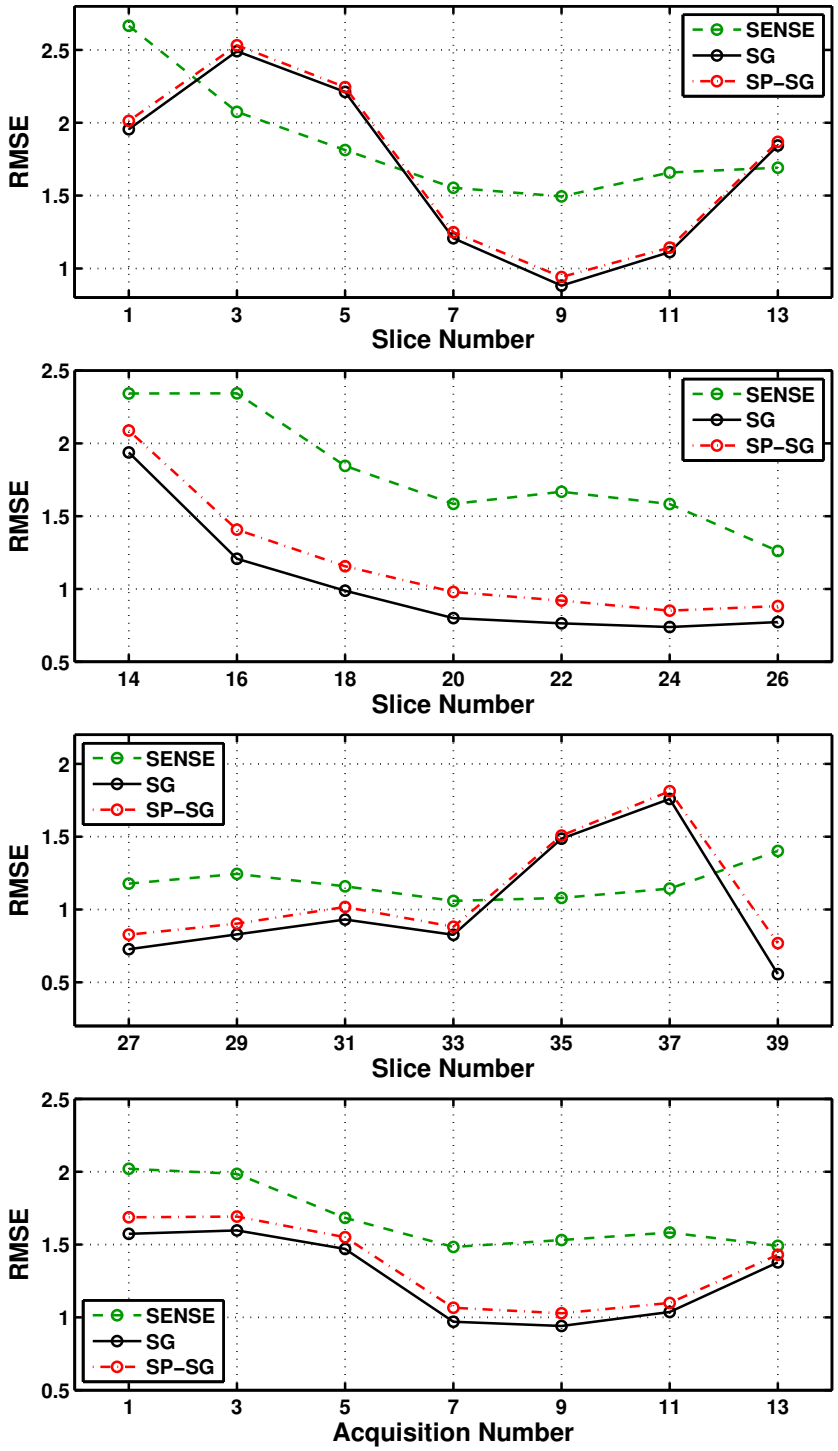

Figure 4.18: Concentric ring simulations: using each method, the top 3 plots show the RMSE within individual slices. The bottommost plot shows the RMSE for each acquisition of 3 simultaneous slices shown directly above it in the upper 3 plots.

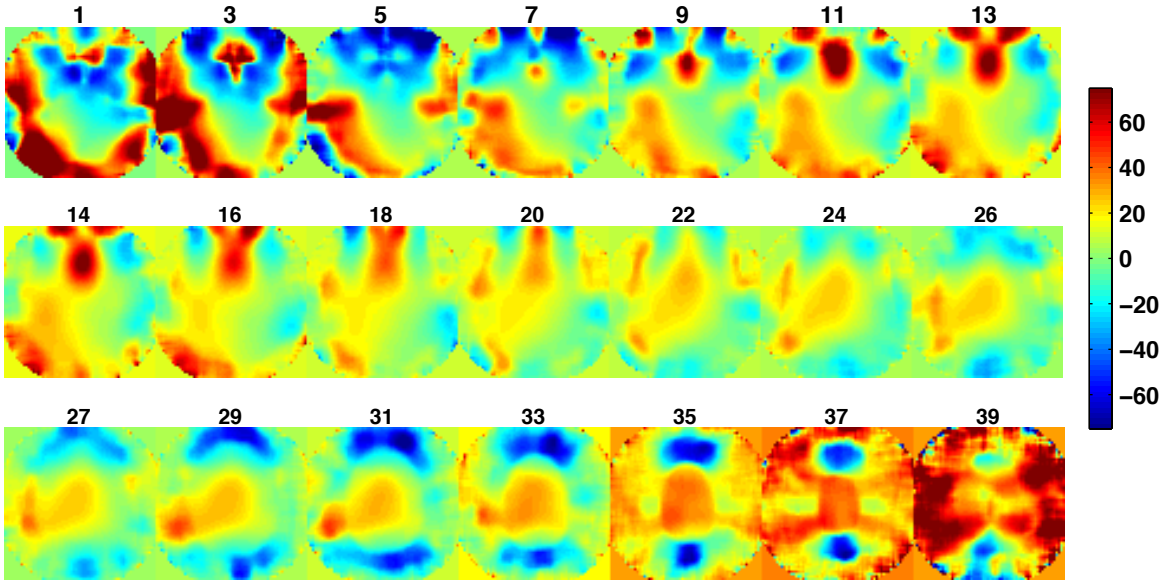

Figure 4.19: Concentric ring simulations: field maps used for the reconstructions. The number at the top of each column of images indicates the slice number for that column. The colormap is in units of Hertz.

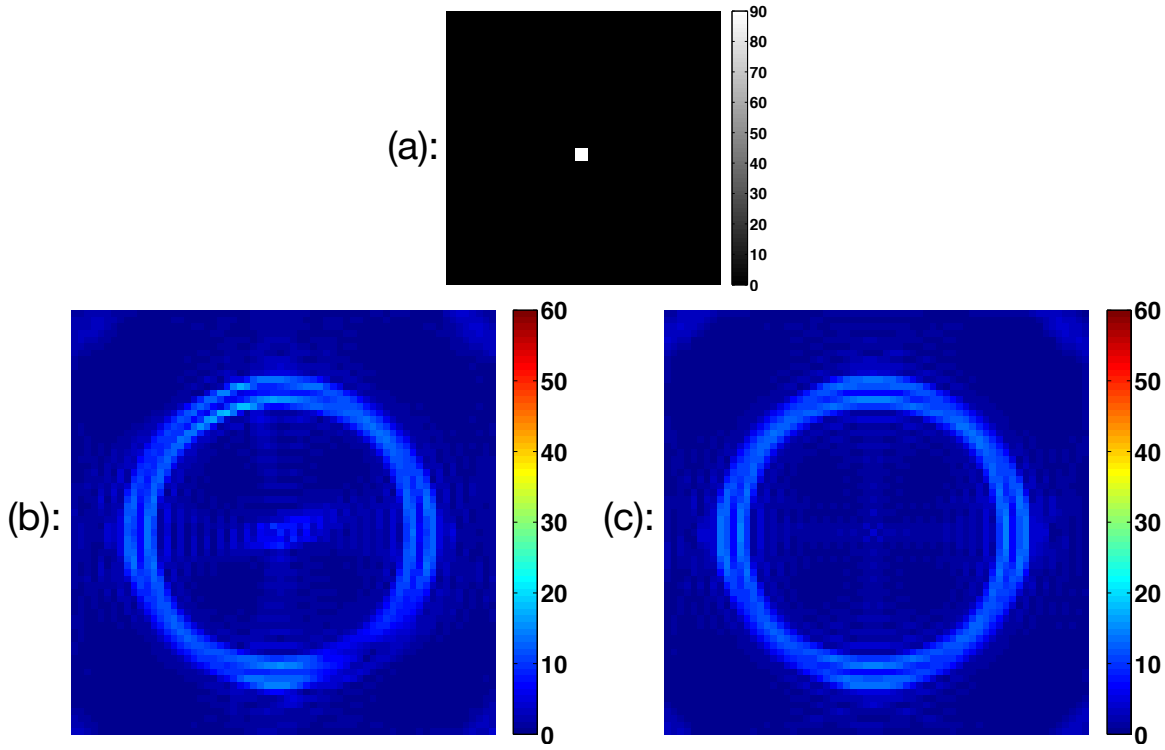

Figure 4.20: (a) Point used to calculate the modulation PSF using blipped spirals (b), and using blipped concentric rings (c). The magnitude of the point in (a) is 90. The maximum magnitude at the center in (b) and (c) is approximately 10.09 and 4.28, respectively.

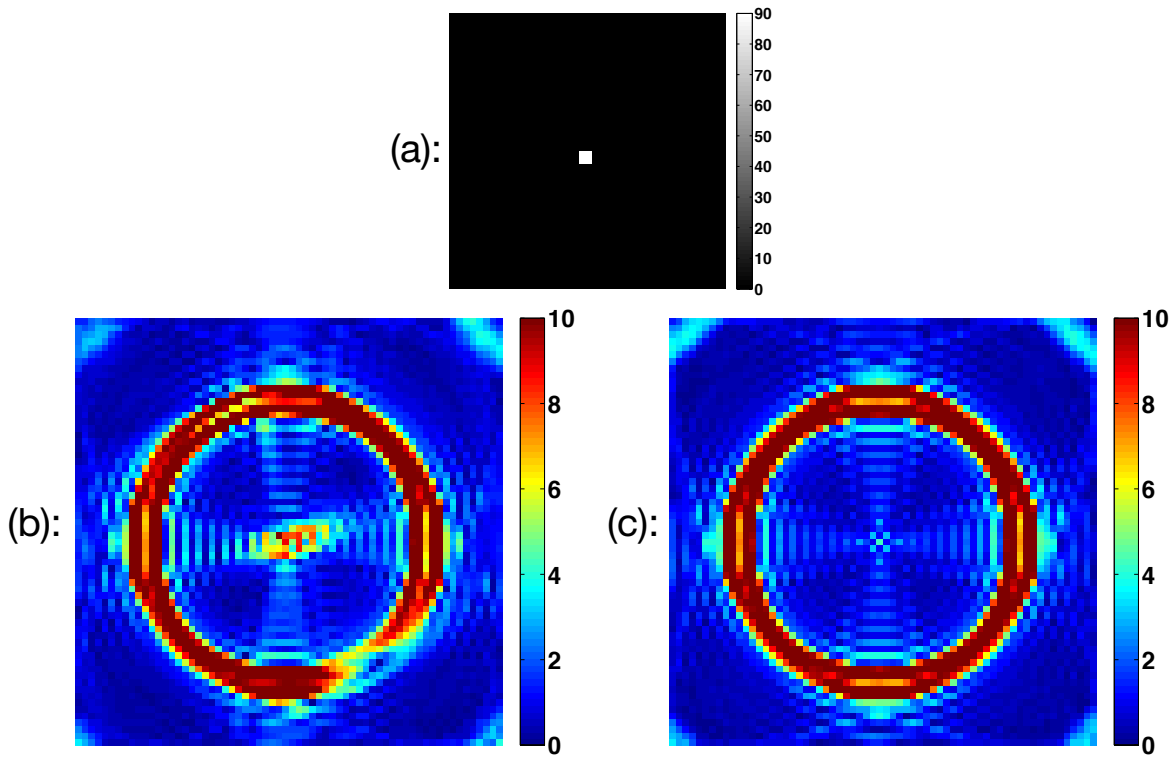

Figure 4.21: Same modulation PSFs shown in Figure 4.20, except windowed lower to portray the differences at the center more clearly. Image (a) shows the point used to calculate the modulation PSF using blipped spirals (b), and using blipped concentric rings (c). The magnitude of the point in (a) is 90. The maximum magnitude at the center in (b) and (c) is approximately 10.09 and 4.28, respectively.

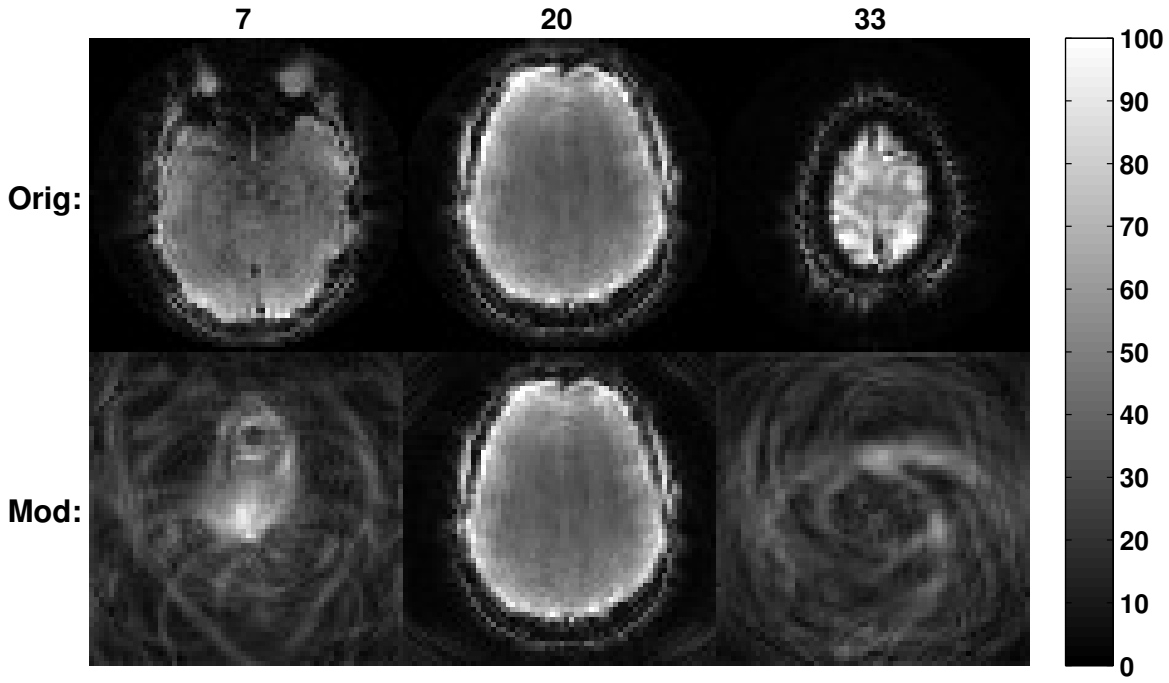

Figure 4.22: Modulation pattern resulting from a blipped concentric ring trajectory for 3 simultaneous slices. The numbers at the top indicate the slice number, where contiguous slices in the volume are numbered 1 through 39. The 20th slice is acquired at z-isocenter, assuming an axial acquisition. The top row shows the original, non-modulated, 3 simultaneous slices. The bottom row shows what the blipped modulation does to the various slices. Slice 20 is unaffected because it is acquired at z-isocenter. The blipped EPI equivalent of slices 7 and 33 would be a simple FOV shift. The modulation pattern for all acquisitions in the volume are shown in Figure 4.23.

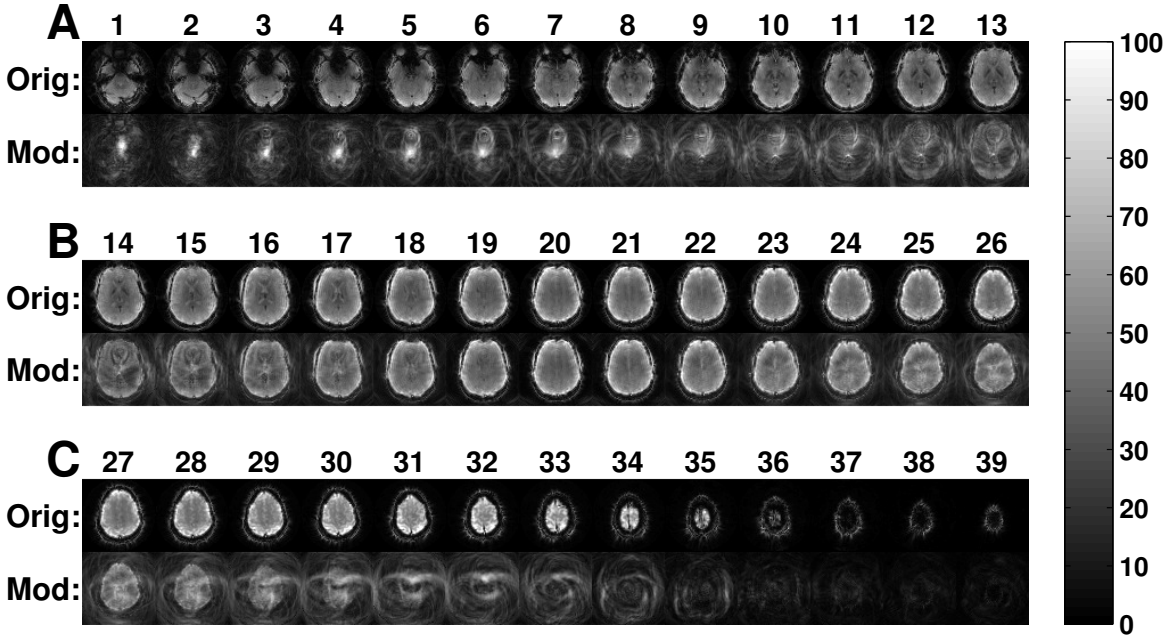

Figure 4.23: Modulation pattern resulting from a blipped concentric ring trajectory for 3 simultaneous slices. The numbers at the top indicate the slice number, where contiguous slices in the volume are numbered 1 through 39. The 20th slice is acquired at z-isocenter, assuming an axial acquisition. The top row in each of (a), (b), and (c) shows the original, non-modulated slices. The bottom row in each of (a), (b), and (c) shows what the blipped modulation does to the various slices. Each column of images in (a), (b), and (c) form the set of images acquired simultaneously in a 3 simultaneous slice acquisition. The acquisition consisting of slices 7, 20, and 33 is shown in Figure 4.22.

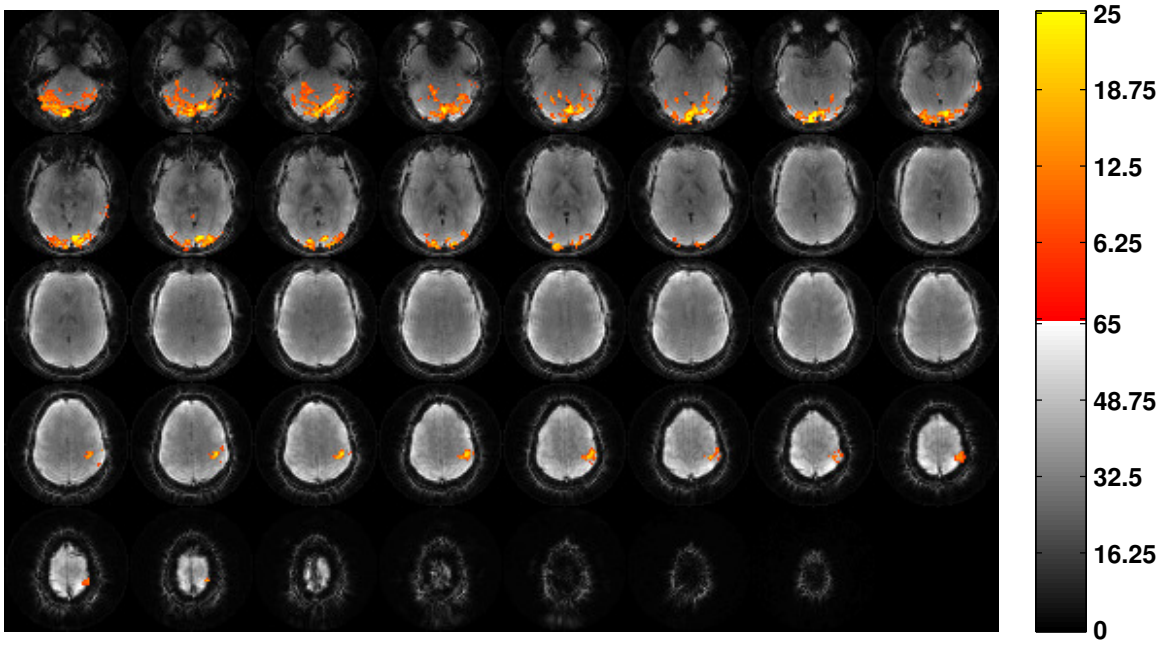

Figure 4.24: Activation map of a 3 simultaneous slice concentric ring fMRI scan with a visual stimulus and motor task. The underlying grayscale image is the SP-SG reconstruction result for one time frame in the middle of the scan. The colormap is the t-score.

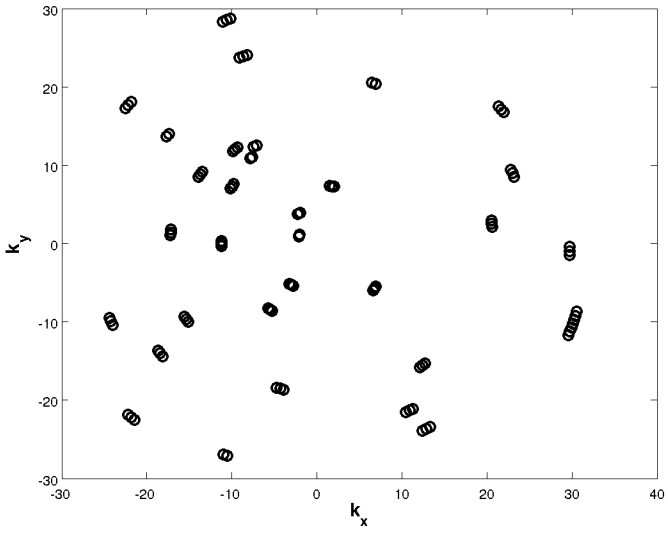

Figure 4.25: Sine wave $g_z(t)$ sampling pattern in the k_x-k_y plane at $k_z = k_z^{\max} \approx 12.821$ m^{-1}. This plot is essentially a slice through the top edge of Figure 4.1.

CHAPTER 5

Coil Compression in Parallel Simultaneous Multislice fMRI[1]

When multiple coils are used for slice separation in SMS imaging, the computational load increases by several factors during reconstruction. Coil compression reduces the amount of data used in processing by exploiting the redundancy of the acquired signal from different coils. By combining the original coil data into a new, reduced set of virtual coils, the amount of data is decreased by several factors, which reduces the computational burden for reconstruction. In this chapter, we propose generalized autocalibrating partially parallel acquisitions-based simultaneous-multislice-acquired coil compression (GRABSMACC), a method that uses the slice-separation kernel to simultaneously compress the k-space data before it is transformed into the image domain. Similarly to GRAPPA [22], GRABSMACC does not rely on accurate sensitivity maps for reconstruction, which is an advantage over SENSE [21] in parallel imaging. In this work, GRABSMACC is demonstrated with the non-Cartesian concentric ring sampling pattern, but should also work with Cartesian trajectories such as EPI.

King et al. [76, 77] implemented coil compression in hardware by changing the image signal basis to one composed of the eigenvectors of the noise covariance matrix. The hardware implementation has SNR benefits, but lacks the flexibility of software

[1]This chapter is based on Refs. [75] and [69].

coil compression, especially with varying levels of acceleration in different directions. On the software side, Buehrer et al. [78] developed a method that reduces image noise in parallel MRI by taking advantage of coil noise covariance and the coil sensitivities for aliased voxels. Not only does this method rely on sensitivities and the issues that go along with the acquisition and accuracy of sensitivity maps, but it requires the undersampling to produce a simple point spread function for it to be practical. Huang et al. [79] used Principal Component Analysis in the k-domain, circumventing the need for coil sensitivities and noise covariance. More recently, Zhang et al. [74] reduced the number of required virtual coils by performing a Singular Value Decomposition (SVD) to compress data in a hybrid image-k-domain. This method was implemented by Cauley et al. and shown to work well with a blipped EPI trajectory in SMS [80]. However, the method relies on a Fourier transform in a fully sampled direction to obtain hybrid space, which is not possible for many non-Cartesian trajectories, such as our implementation of a concentric ring readout. Beatty et al. [81] have proposed a new method that combines the k-space reconstruction kernel with a coil compression kernel. This method is similar to GRABSMACC in that the unaliasing process is also responsible for coil compression. However, in the current work, we extend this general idea to SMS imaging with non-Cartesian trajectories.

Because GRABSMACC uses the slice-separation kernel to simultaneously compress k-space data, the kernel convolution step for slice separation uses a larger dataset when compared to standard SVD coil compression, which only operates on pre-compressed data. Although this comes at an increased computation cost when compared to standard SVD compression, we show that GRABSMACC preserves functional activation better at higher levels of compression, thus enabling a fewer number of virtual coils to be used when compared to standard compression. Furthermore, the main computational burden in SMS reconstruction lies not in the slice separation process, but in the transformation of unaliased k-space data for each coil into the

image domain prior to coil combination. Therefore, the reduction in the number of required coils for GRABSMACC results in significant computational time savings, especially when reconstructing multiple fMRI studies.

This chapter provides the following novel contributions: (a) the development and evaluation of GRABSMACC, a practical method for coil compression and reconstruction of both Cartesian and non-Cartesian SMS fMRI, and (b) the analysis of coil compression performance and computation time in fMRI with both non-SMS and SMS imaging. With coil compression in fMRI, care must be taken to ensure that the functional activation in an fMRI scan is not reduced in exchange for data compression. In this chapter, we present the methodology of GRABSMACC and analyze concentric-ring-in fMRI scans of several subjects to compare activation performance, image artifacts, SNR, and reconstruction speed for different levels of coil compression using GRABSMACC, standard coil compression in GRAPPA-based and SENSE-based SMS reconstruction, and coil compression in traditional, non-SMS imaging. In addition, data from a separate spiral-in scan is used to compare image artifacts and SNR with those from the concentric ring data.

5.1 Methods

Along with GRABSMACC, all algorithms, reconstruction methods, and coil compression methods described in this section are available at https://github.com/alcu/sms.

5.1.1 Standard Coil Compression in Slice-GRAPPA and Split Slice-GRAPPA

Standard coil compression in SG and SP-SG compresses the SMS k-space data before the entire GRAPPA process described previously. Each acquisition in a time frame is compressed separately, resulting in n_{acq} compression matrices. First, n_{stack} number of

time frames, located in the middle of the fMRI run, are stacked into a matrix $\boldsymbol{S}_{\text{stack}}$, with data from each coil arranged along a single column of $\boldsymbol{S}_{\text{stack}}$. The dimensions of $\boldsymbol{S}_{\text{stack}}$ are $n_{\text{stack}}n_{\text{dat}}$-by-$n_{\text{coil}}$, where n_{dat} is the number of samples located only in the concentric rings, and n_{coil} is the full number of coils in the receive array. The compression matrix, $\boldsymbol{V}_{\text{comp}}$, is calculated by computing the SVD of $\boldsymbol{S}_{\text{stack}}$, described by

$$\boldsymbol{S}_{\text{stack}} = \boldsymbol{U}\boldsymbol{\Sigma}\boldsymbol{V}^{*}, \tag{5.1}$$

and using the first n_{vcoil} columns of $\boldsymbol{V}$ as $\boldsymbol{V}_{\text{comp}}$, where n_{vcoil} is the number of virtual coils to which the data should be compressed. Since each acquisition in a time frame is compressed separately, there will be n_{acq} compression matrices, where n_{acq} is the number of acquisitions in a single time frame of an SMS scan.

To compress each fMRI time frame, each SMS acquisition from that frame is assembled into a matrix $\boldsymbol{S}_{\text{full}}$ and multiplied by the corresponding $\boldsymbol{V}_{\text{comp}}$ for that SMS acquisition to obtain

$$\boldsymbol{S}_{\text{comp}} = \boldsymbol{S}_{\text{full}}\boldsymbol{V}_{\text{comp}}, \tag{5.2}$$

where $\boldsymbol{S}_{\text{comp}}$ contains the compressed SMS acquisition and has dimensions n_{dat}-by-n_{vcoil}. The matrix $\boldsymbol{S}_{\text{full}}$ is constructed in the same manner as $\boldsymbol{S}_{\text{stack}}$, except with data from only one time frame, and therefore has dimensions n_{dat}-by-n_{coil}. Before calculating $\boldsymbol{W}$ in Equation (4.3), the calibration data must be compressed with the same $\boldsymbol{V}_{\text{comp}}$ matrices before being interpolated and arranged into $\boldsymbol{S}_{\text{trg}}$. Specifically, the calibration scan has $n_{\text{tot}} = n_{\text{slc}}n_{\text{acq}}$ acquisitions, and the n_{slc} non-simultaneous calibration acquisitions that match the excitation locations of a single SMS acquisition should each use the same $\boldsymbol{V}_{\text{comp}}$ as that single SMS acquisition. Once the SMS and calibration data are compressed, the previously described SG or SP-SG process is performed with a reduced coil dimension of n_{vcoil} for all matrices in Equation (4.3).

5.1.2 GRABSMACC

In contrast, our proposed method for coil compression, GRABSMACC, only compresses the "target" data and not the "source" data, and uses the GRAPPA kernel for both slice separation and coil compression. In this method, the non-simultaneous acquisitions from the calibration scan are used to compute the compression matrices $\boldsymbol{V}_{\text{comp}}$. Specifically, the calibration data is used for $\boldsymbol{S}_{\text{stack}}$ in Equation (5.1), and the first n_{vcoil} columns of $\boldsymbol{V}$ are used to construct $\boldsymbol{V}_{\text{comp}}$. Since there are $n_{\text{tot}} = n_{\text{slc}} n_{\text{acq}}$ calibration acquisitions, or equivalently, slices, there are n_{tot} number of $\boldsymbol{V}_{\text{comp}}$ matrices, one for each slice. Each slice of the calibration scan is arranged into an $\boldsymbol{S}_{\text{full}}$, and each $\boldsymbol{S}_{\text{full}}$ is then compressed using Equation (5.2).

Once the calibration data is compressed to n_{vcoil} coils, it is used in Equation (4.3) as $\boldsymbol{S}_{\text{trg}}$ for computation of $\boldsymbol{W}$. No coil compression is done on data used for $\boldsymbol{S}_{\text{src}}$. Therefore, in GRABSMACC, the source data matrix has full coil dimensions, the target matrix has compressed coil dimensions, and the kernel has both. Specifically, in SG the dimensions of $\boldsymbol{S}_{\text{src}}$ are n_{rep}-by-$n_{\text{kern}} n_{\text{coil}}$, those for $\boldsymbol{S}_{\text{trg}}$ are n_{rep}-by-$n_{\text{slc}} n_{\text{vcoil}}$, and those for $\boldsymbol{W}$ are $n_{\text{kern}} n_{\text{coil}}$-by-$n_{\text{slc}} n_{\text{vcoil}}$, where n_{rep} is the number of GRAPPA kernel repetitions, n_{kern} is the number of weights in the kernel for a single coil, n_{coil} is the full number of coils in the receive array, and n_{slc} is the number of simultaneously acquired slices for each SMS acquisition. In SP-SG, the dimensions of $\boldsymbol{S}_{\text{src}}$ are $n_{\text{rep}} n_{\text{slc}}$-by-$n_{\text{kern}} n_{\text{coil}}$, those for $\boldsymbol{S}_{\text{trg}}$ are $n_{\text{rep}} n_{\text{slc}}$-by-$n_{\text{slc}} n_{\text{vcoil}}$, and those for $\boldsymbol{W}$ remain unchanged from SG.

To separate the slices in GRABSMACC, uncompressed k-space data from each acquisition of each time frame is used for $\boldsymbol{S}_{\text{src}}$, and Equation (4.3) is used to compute the compressed, separated slices in $\boldsymbol{S}_{\text{trg}}$. Hence, multiplication by $\boldsymbol{W}$ performs a simultaneous slice separation and compression of k-space data. Finally, the slice-separated data can be transformed into images by the same conjugate gradient and square-root-sum-of-squares process described previously.

5.1.3 Standard Coil Compression in SENSE

Standard coil compression for SENSE was done exactly the same as for standard coil compression in SG and SP-SG, described previously. However, a new set of virtual coil sensitivities need to be computed for use in Equation (4.1). This was done by first compressing the k-space data from the non-delayed field map acquisition before performing the previously-described ESPIRiT process to generate n_{vcoil} sensitivity maps. Similar to the GRAPPA calibration data, n_{acq} number of $\boldsymbol{V}_{\text{comp}}$ matrices must be used appropriately for $n_{\text{tot}} = n_{\text{slc}} n_{\text{acq}}$ non-simultaneous slices. Finally, Equation (4.1) with $n_{\text{coil}} = n_{\text{vcoil}}$ is used to reconstruct the separated slices by using the compressed SMS acquisitions for $\boldsymbol{s}_u$ and the virtual coil sensitivities for $\boldsymbol{C}_{u,v}$.

5.1.4 fMRI Experiment Design and Analysis

For each of five healthy subjects, both a concentric ring SMS fMRI scan and a non-simultaneous multislice (non-SMS) concentric ring fMRI scan were performed in accordance with the University of Michigan Institutional Review Board using a GE Discovery MR750 3.0 Tesla MRI scanner and a Nova Medical 32-channel receive head coil. The SMS and non-SMS scans each had a total acquisition time of 240 s for the entire run. Each fMRI scan had 20-second blocks of both visual and motor stimuli alternating with 20-second blocks of rest. The visual stimulus consisted of a flashing checkerboard pattern, and subjects were instructed to tap the fingers on only their right hand while the visual stimulus was present.

Functional activation for all scans was computed using the General Linear Model on detrended magnitude data using a paradigm model waveform based on SPM's canonical hemodynamic response function [82]. Maps of t-scores were computed using Ref. [59], which accounts for degrees of freedom in the time-series data, and a threshold of $t > 6$ was used to determine voxel activation in all scans. Counts of

activated voxels were performed by manually masking visual and left motor cortex areas, then counting the number of activated voxels within those masked regions. A different mask was created for each subject, but all methods performed on data from one subject used the same mask for that subject.

5.1.5 SMS Scan Parameters

Each SMS fMRI time frame consisted of $n_{\text{acq}} = 13$ acquisitions per TR of $n_{\text{slc}} = 3$ simultaneous slices, each of which were 3 mm thick and acquired $n_{\text{acq}}d_{\text{slc}} = 39$ mm apart with no space between contiguous acquisitions. The SMS TR and TE were 663 ms and 31 ms, respectively. The SMS RF pulse was created using a sum of 3 Hamming-windowed sincs, each of which was frequency-modulated to create the 39 mm gap between simultaneous slices. The SMS RF pulses for all 5 subjects were 6.4 ms in length, and the Ernst angle for gray matter was used for the flip angle.

The calibration TR and TE in all cases were 663 ms and 31 ms, respectively. To match the SMS scans, each calibration time frame had $n_{\text{tot}} = n_{\text{slc}}n_{\text{acq}} = 39$ slices. Because the SMS scans used the minimum TR for 13 acquisitions, only 13 slices of the entire volume could be acquired per TR in the calibration scans. Therefore, a total of $n_{\text{slc}} = 3$ TRs were needed for the calibration data. The RF pulse used for the calibration scan for each subject was the corresponding single non-modulated sinc used for the SMS scan for that subject. The calibration RF pulses for all 5 subjects were 6.4 ms in length.

5.1.6 Trajectory Parameters

The out-to-in concentric ring k_x-k_y trajectory was designed to produce a 64-by-64 image with a 22 cm FOV, and consisted of 32 equally spaced concentric circles with a sample at the k-space origin, as shown in Figure 4.3a. All gradients were designed to

use 150 mT/m/ms for the maximum slew rate and 40 mT/m for the maximum amplitude. The blipped z-gradient consisted of a repeating pattern of positive-negative-positive blips to obtain a k_z trajectory that starts out at $1/\mathrm{FOV}_z$ for the outermost k_x-k_y ring, goes to $-1/\mathrm{FOV}_z$ for the next ring, then 0 for the next ring, and continues with that pattern until the k_x-k_y-k_z origin is reached, where $\mathrm{FOV}_z = n_{\mathrm{tot}} d_{\mathrm{slc}}$ is the SMS field of view in the through-plane direction. The scanner gradient sampling interval was 4 µs, resulting in 6612 samples for the entire concentric ring trajectory, including the initial path from the origin to the outermost ring and the final origin sample. The number of samples located only in the concentric rings was $n_{\mathrm{dat}} = 5892$.

The separate non-SMS spiral-in scan, which was only used to compute image artifacts and SNR, also had a trajectory designed to produce a 64-by-64 image with a 22 cm FOV. A blipped z-gradient was simulated by adding to the spiral k-space data the appropriate amount of phase generated from blips with the same areas as those used for the concentric ring trajectory. For the spiral data, the simulated z-blips were timed to occur at one particular angular location, resulting in the trajectory shown in Figure 2.6. The gradient sampling interval was also the same as that for concentric rings, and resulted in $n_{\mathrm{dat}} = 5056$ total samples for each spiral.

5.1.7 GRAPPA Reconstruction Parameters

For all the GRAPPA-based reconstructions, each concentric ring was interpolated to a constant angular velocity trajectory of 208 samples, then separated into 8 angular sectors, as depicted in Figure 4.3a. The spiral scan was not reconstructed using GRAPPA. The GRAPPA kernel for each sector of each coil consisted of a 3-by-3 grid that weights 3 consecutive rings and 3 consecutive interpolated points in the angular direction, resulting in $n_{\mathrm{kern}} = 9$. For each sector of each coil, an additional asymmetric kernel was computed for the outermost and innermost rings, respectively. Instead of computing additional asymmetric kernels for the angular edges, each sector

was created with an overlap of 1 point along both angular edges so that the original, non-asymmetric kernel could be used to compute all data points up to the non-overlapped angular edge. Finally, for the sample at the k-space origin, another kernel was constructed that uses 8 evenly spread data points from each of the innermost 3 rings. Coil compression for SG and SP-SG used $n_{\text{stack}} = 10$. For GRABSMACC, only the calibration frame was used to compute coil compression matrices, so $n_{\text{stack}} = 1$.

Conjugate gradient with 5 iterations and finite difference regularization was used to transform k-space data into the image domain. Theory from Ref. [83] was used to choose the regularization parameter in terms of the desired spatial resolution in the reconstruction. The regularization parameter for a point spread function with a full width at half maximum of 1.35 was determined, which results in a slight degree of smoothing. However, the same regularization parameter was used for all methods including all the GRAPPA-based, SENSE, and non-SMS reconstructions, so all methods should have the same degree of smoothing from regularization.

5.1.8 SENSE Reconstruction Parameters

Each concentric ring SMS scan and the spiral scan were reconstructed using SENSE. Conjugate gradient with 10 iterations was used, along with the same field map, regularization parameter, and NUFFT parameters used in the SG and SP-SG conjugate gradient computation. The number of iterations was determined by examining the change in the solution with each iteration and using the number that resulted in a change similar to using 5 iterations with non-SMS reconstruction. The ESPIRiT process used a kernel of size 3-by-3 on only the central 32-by-32 region of the 64-by-64 Cartesian k-space, a threshold of 0.02 times the largest singular value to determine the ESPIRiT calibration matrix null space, and an eigenvalue threshold of 0.95 for the final eigenvector sensitivity maps. Coil compression in SENSE was done with $n_{\text{stack}} = 10$.

5.1.9 Non-SMS Scan Parameters

The non-SMS fMRI scans had $n_{\text{tot}} = n_{\text{slc}} n_{\text{acq}} = 39$ slices per time frame to match the SMS scans. However, the non-SMS scans used a TR of 1989 ms and a TE of 31 ms. The same RF pulse used for the SMS calibration scans was used for the non-SMS scans, but with a different Ernst flip angle for gray matter because of the longer TR. A separate field map acquisition was also acquired. Conjugate gradient using NUFFTs with inhomogeneity correction and finite difference regularization was used for reconstruction, and the coil images were combined using square-root-sum-of-squares. The same regularization parameter and NUFFT parameters used in SG and SP-SG were used with 5 iterations. It was found that further iterations did not produce significant changes in the solution for non-SMS data. The non-SMS scans were also coil-compressed before reconstruction for comparison with the SMS reconstructions. Specifically, $n_{\text{stack}} = 10$ time frames from the middle of the scan were used in a similar manner as in standard coil compression of SG and SP-SG, with the only difference being that there were $n_{\text{tot}} = 39$ different $\boldsymbol{V}_{\text{comp}}$ matrices, one for each slice.

5.1.10 Field Maps

The field map acquisitions for SMS scans used a TR of 663 ms, whereas those for the non-SMS scans used a TR of 1989 ms. The field map acquisitions for the non-SMS scans were relatively straightforward; two whole-volume time frames were captured with one frame having a slightly delayed TE. The SMS field maps were necessarily acquired in a similar manner to the SMS calibration scans since a TR of 663 ms was only long enough to acquire 13 slices. In other words, a total of $2n_{\text{slc}} = 6$ TRs were needed to acquire 2 whole-volume frames, with n_{slc} of the TRs using a delayed TE. Field map data was reconstructed in 2 passes using conjugate gradient with NUFFTs,

inhomogeneity correction, and the same regularization parameter as all the rest of the methods.

5.1.11 Image Artifacts

The interslice leakage artifact and intraslice artifact using the Linear System Leakage Approach [73] were computed for all SMS reconstruction methods by taking the concentric ring non-SMS data consisting of only the middle $n_{\text{acq}} = 13$ slices of the non-SMS scan of subject 5 and reconstructing them with each of the various SMS methods. Additionally, a spiral non-SMS scan was used in a similar manner to compute the same interslice leakage and intraslice artifacts for comparison. In the notation of Ref. [73], the interslice leakage metric of $(L_{2\to1} + L_{2\to3})$ was computed, along with the intraslice artifact of $(I_{2\to2} - I_2)$. Figure 5.1 illustrates how these artifacts were computed. The interslice leakage artifact metric is defined as $\sum_w (|p_{w,1}|^2 + |p_{w,3}|^2) \,/\, \sum_w (|p_{w,1}|^2 + |p_{w,2}|^2 + |p_{w,3}|^2)$, where $p_{w,v}$ is the complex value of pixel w in slice v of the 3 simultaneous slice reconstruction, and w ranges through the number of pixels in each slice. Here, $v = 1$ indicates all of the 13 inferior slices in the 39 total slices, $v = 2$ indicates the middle 13 slices, and $v = 3$ indicates the superior 13 slices. The intraslice artifact metric is defined as $\sum_w (|p_{w,2}|^2 - |q_{w,2}|^2) \,/\, \sum_w (|p_{w,1}|^2 + |p_{w,2}|^2 + |p_{w,3}|^2)$, where $q_{w,v}$ is the complex value of the ground truth (non-SMS) voxel. The total image artifact of $(L_{1\to2} + I_{2\to2} + L_{3\to2} - I_2)$ was computed by synthesizing SMS data from all 39 slices of the non-SMS scan, then reconstructing and comparing the SMS reconstruction with the original, ground truth non-SMS slices. Figure 5.1 also illustrates how this artifact was computed. The total image artifact is defined as $\sum_w (|p_{w,2}|^2 - |q_{w,2}|^2) \,/\, \sum_w (|q_{w,2}|^2)$. For the concentric ring data, all artifact computations were performed on 10 time frames of the non-SMS scan of subject 5, and the resulting metrics and maps were computed on the average of those 10 frames.

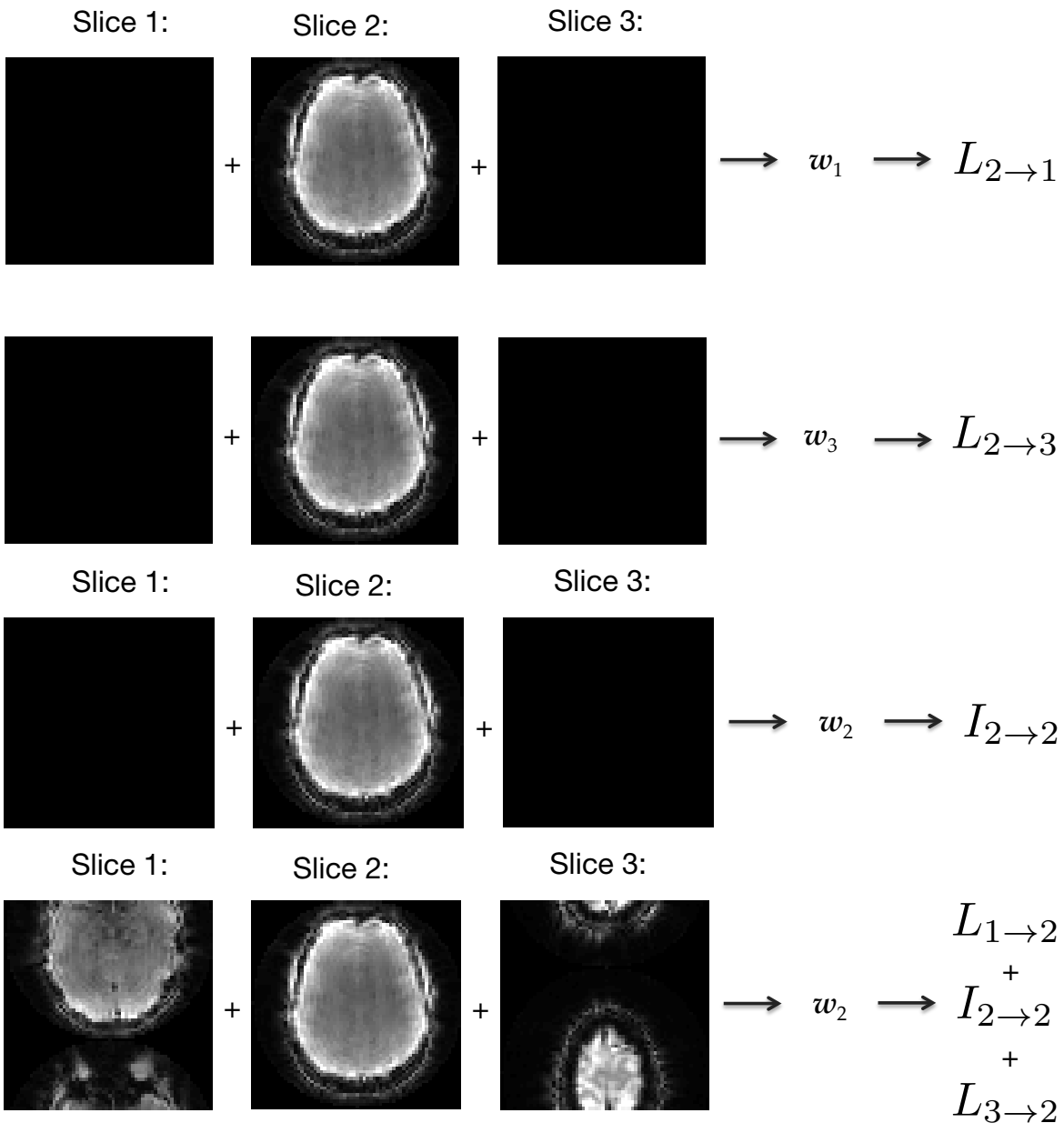

Figure 5.1: Illustration showing the concept of interslice leakage artifacts (top two rows), intraslice artifacts (third row), and total image artifacts (bottom row). In this figure, w_v indicates the kernel that computes k-space data of (one coil of) separated slice v.

5.1.12 Retained SNR

The Pseudo Multiple Replica method [84] was used to compute the retained SNR, which is equivalently defined as $1/g$, where g is the geometry factor in SMS recon-

structions. In order to use this method, a single non-SMS concentric ring volume and a noise-only scan were performed on one subject. The noise-only scan was used to construct a noise covariance matrix for each slice. To compute pseudo multiple replicas for a non-SMS acquisition, an instance of correlated noise was generated for each slice of each replica by multiplying an instance of complex standard normal noise by the square root of the noise covariance matrix for that slice. This correlated noise was then added to a non-SMS concentric ring slice to obtain k-space data for one slice of one replica. A total of 250 replicas were generated by repeating this process.

To compute replicas for an SMS acquisition, slices of the non-SMS volume were appropriately modulated and summed to simulate SMS acquisitions, and only the first n_{acq} noise covariance matrices were used to generated replicas as above. An additional single non-SMS spiral volume and spiral noise-only scan were performed on the same subject to generate replicas for both non-SMS and SMS spiral acquisitions. Finally, these pseudo multiple replicas were reconstructed with various different methods and coil compression as described previously.

The temporal SNR of the non-SMS pseudo multiple replicas reconstructed without coil compression was calculated by taking the temporal mean divided by the temporal standard deviation. The same computation was done to calculate the temporal SNR for each reconstruction method and coil compression level used on either SMS or non-SMS replicas. The retained SNR map for each method and compression level was calculated by dividing the SNR for that method by the SNR of the non-compressed non-SMS replica reconstructions. The average retained SNR for each method was computed by taking the average value within a manually-created within-brain region.

5.2 Results

5.2.1 Activated Voxel Counts

Figure 5.2a shows the mean of activated voxel counts across all 5 subjects in the visual and motor cortex ROIs for different acquisition and reconstruction methods versus number of virtual coils. Since $n_{\text{coil}} = 32$ for all experiments, 32 indicates no coil compression. In the Results section and in all the Figures, the terms "SG" and "SP-SG" by themselves refer to standard coil compression in SG and SP-SG, respectively. The terms "GRABSMACC-SG" and "GRABSMACC-SP-SG" refer to the use of GRABSMACC in SG and SP-SG, respectively. Looking at Figure 5.2a, the activated count for both GRABSMACC-SG and GRABSMACC-SP-SG remains unaffected until the number of virtual coils is reduced to around 5. The count for SP-SG initially tracks that of GRABSMACC-SP-SG, but has a drop at just 14 virtual coils and quickly drops far lower than the GRABSMACC-SP-SG count. The count for SG increases towards the count for SP-SG as the number of virtual coils decreases and similarly drops back down at 14 virtual coils. The SENSE count also begins to decrease at 14 virtual coils. Coil compression in non-SMS imaging performed similarly to both GRABSMACC-SG and GRABSMACC-SP-SG, with a decrease in count starting at around 4 virtual coils.

The counts for each method were also normalized by dividing by the count using all 32 coils. Figure 5.2b shows the mean across subjects of the normalized counts for each method, along with error bars indicating 95% confidence intervals for each mean. The normalized counts for all four methods exhibit similar trends as they do in Figure 5.2a. Of note, the error bars around the normalized counts for GRABSMACC-SG, GRABSMACC-SP-SG, and non-SMS are very small, especially for 10 to 32 virtual coils, indicating excellent reproducibility between subjects. The error bars around the counts for SENSE are also small, but for a reduced range of 20 to 32 virtual coils.

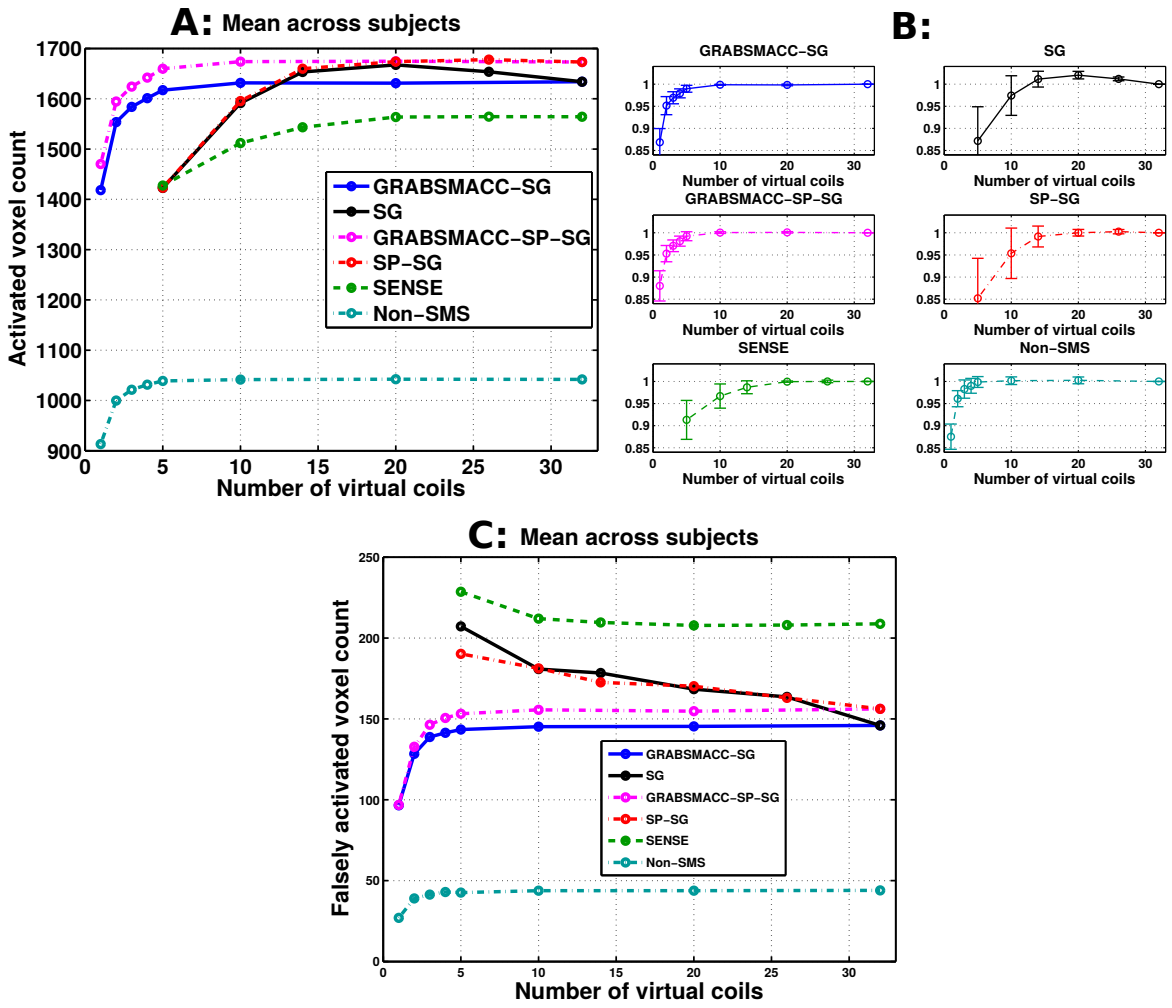

Figure 5.2: (a) Activated voxel counts: mean across all 5 subjects. (b) Normalized activated voxel counts: mean across all 5 subjects with error bars indicating 95% confidence intervals. Before taking the mean across subjects, the count for each method was normalized by the count using all 32 coils. (c) Falsely activated voxel counts: mean across all 5 subjects. Falsely activated voxels are defined as active brain voxels that are outside the visual and motor cortex areas used for the activated voxel counts in (a) and (b). A t-score threshold of 6 was used for all methods.

For SG and SP-SG, the error bars are relatively large below 20 virtual coils.

Figure 5.2c shows the mean of "falsely" activated voxel counts across all 5 subjects in the visual and motor cortex areas for different acquisition and reconstruction methods versus number of virtual coils. Falsely activated voxels are defined as active brain voxels that are outside the visual and motor cortex ROIs used for the activated

voxel counts in Figures 5.2a and 5.2b. The most striking feature of Figure 5.2c is that SG and SP-SG exhibit increased false activation with just a small amount of compression. SENSE does as well, but to a lesser extent. However, the false activation level does not change appreciably for GRABSMACC-SG, GRABSMACC-SP-SG, and non-SMS until approximately 5 virtual coils.

Table 5.1 contains p-values of paired Dunnett [85] multiple comparisons of a two-way analysis of variance (ANOVA) of activated voxel counts. For each method, the control used in Dunnett's multiple comparison method is the activated voxel count using all 32 coils. This control is then paired with and compared to the voxel count using different numbers of virtual coils for each method. In other words, each entry in the table corresponds to a test between the counts for the number of virtual coils listed at the top, and the counts for all 32 coils using the same method. Using a p-value threshold of 0.05 for rejecting the null hypothesis, the largest number of virtual coils with a count that significantly differs from the count using all 32 coils is indicated in bold for each method in Table 5.1. Non-SMS has the best compression performance with a significant difference in counts only when the number of virtual coils is all the way down to 2. GRABSMACC-SG and GRABSMACC-SP-SG do almost as well, with a difference when there are only 3 virtual coils. SG and SP-SG do slightly worse, with a significant change at 5 virtual coils. However, SG and SP-SG still perform better than SENSE, which does the worst with a significant count difference when compressing down to 10 virtual coils.

5.2.2 Activation Maps and Reconstructed Images

Figure 5.3a shows the quantitative t-score activation map for one visual cortex slice of subject 5 for different combinations of method (listed at the left) and number of virtual coils (listed at the top). The same visual cortex slice from the same fMRI time frame was reconstructed using the indicated combination of method and virtual coils, and

	Number of virtual coils								
Method	1	2	3	4	5	10	14	20	26
GRABSMACC-SG	<0.001	<0.001	**0.0078**	0.13	0.74	1.0		1.0	
SG					**<0.001**	0.47	0.94	0.67	0.94
GRABSMACC-SP-SG	<0.001	<0.001	**0.011**	0.17	0.89	1.0		1.0	
SP-SG					**<0.001**	0.11	0.99	1.0	1.0
SENSE					<0.001	**0.013**	0.54	1.0	1.0
non-SMS	<0.001	**0.016**	0.46	0.94	1.0	1.0		1.0	

Table 5.1: For each method, this table displays p-values using paired Dunnett multiple comparisons of a two-way ANOVA of activated voxel counts. The count for each number of virtual coils is compared pairwise with the count using all 32 coils using the same method. For each method, the value in bold corresponds to the largest number of virtual coils with a p-value less than 0.05, or equivalently, the largest number of virtual coils with an activation count that differs significantly from the non-compressed reconstruction.

is shown underneath the activation map in each entry. In other words, the underlying background image is the actual result using the indicated reconstruction method. The non-SMS images are from a different fMRI run and are intensity windowed differently from the SMS images due to the differing TR. Figure 5.3b shows the same data as 5.3a, but for one motor cortex slice of subject 5.

The visual and motor cortex activation maps are very similar between all the SMS methods, which is expected since they are all reconstructed using the same data. The non-SMS activation pattern, however, is still quite similar to the SMS reconstruction results, indicating good functional reproducibility in SMS fMRI. Comparing between different numbers of virtual coils, the activation map for each method does not change much in terms of shape or location; the only noticeable difference is a smaller activation size when the number of virtual coils becomes very small. In this regard, these results corroborate those in Figures 5.2a and 5.2b.

Figure 5.4 shows the virtual coil sensitivities for the z-isocenter slice when computing $\boldsymbol{V}_{\text{comp}}$ from non-SMS k-space data and from SMS k-space data for 10 virtual coils. The original uncompressed coil sensitivities are shown in Figure 4.15. Qualita-

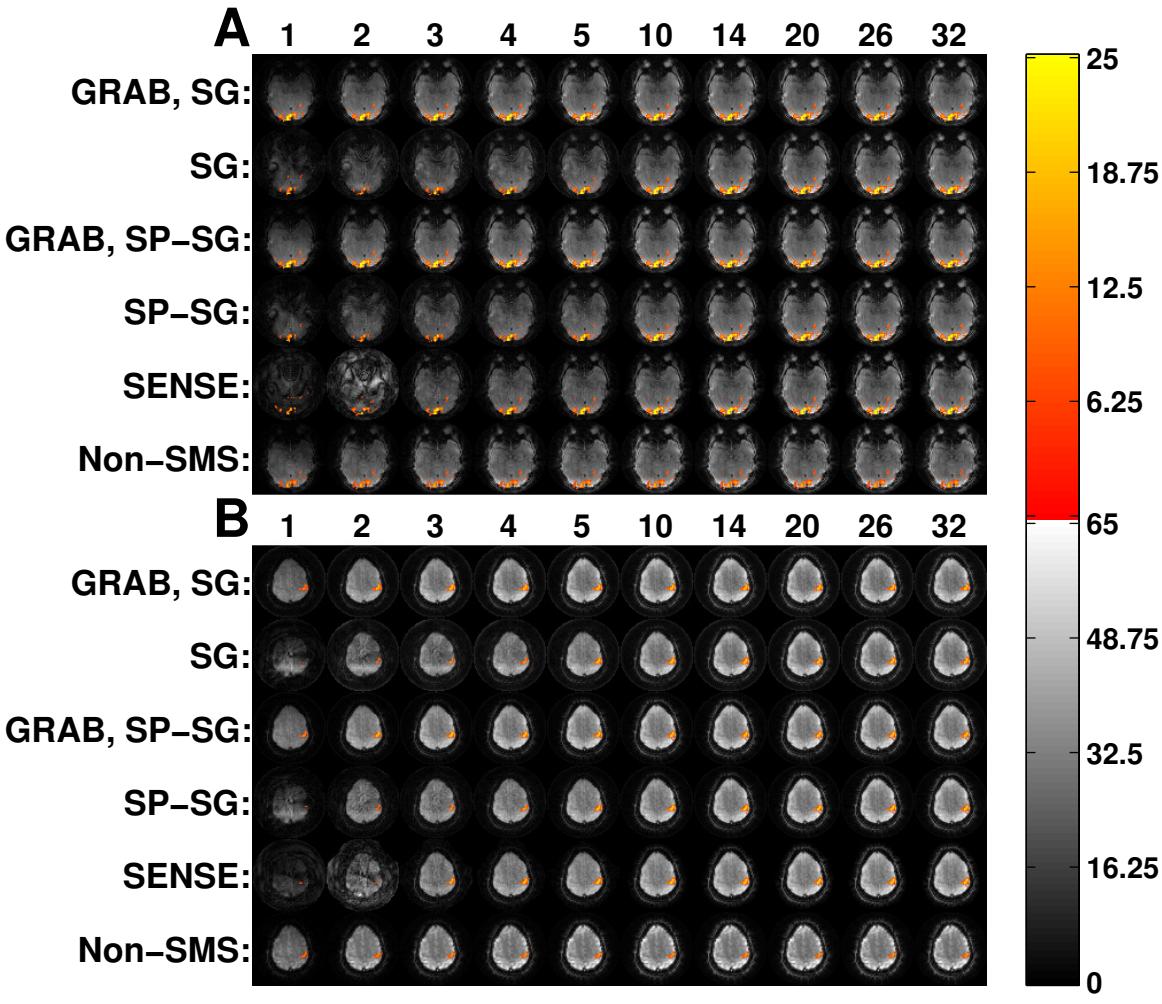

Figure 5.3: (a) Visual and (b) motor cortex activation maps over reconstructed images for subject 5. The underlying background image is the actual result using the indicated reconstruction method. A t-score threshold of 6 was used for all methods. The top of each column lists the number of virtual coils for that column. For each of (a) and (b), the same visual or motor cortex slice is pictured for all methods and number of virtual coils. The activated voxel color scale is the t-score.

tively, the non-SMS virtual coil sensitivity patterns and shading seemed to vary less between subjects than the SMS virtual sensitivity patterns did.

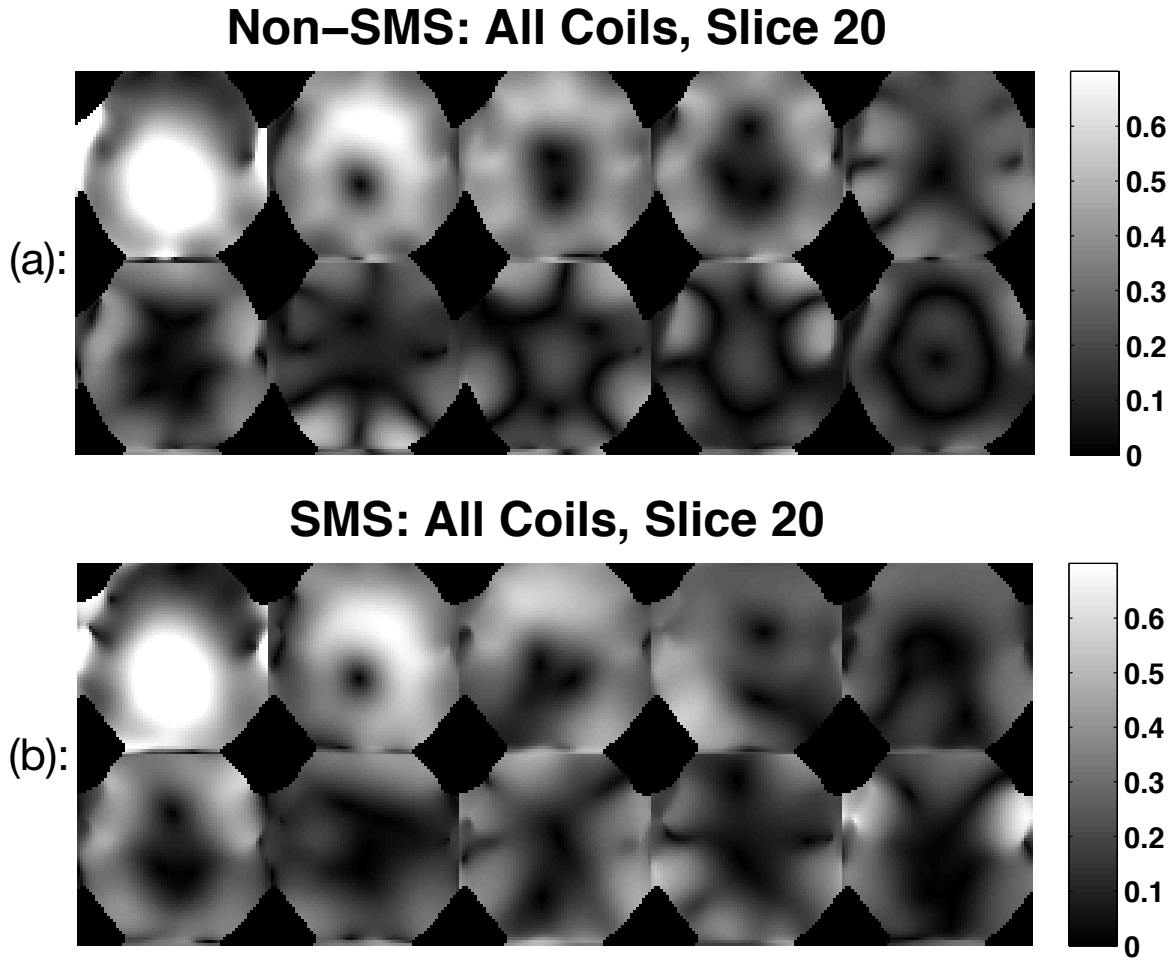

Figure 5.4: Virtual coil sensitivities for slice 20, the z-isocenter slice, when computing the compression matrices from (a) the non-SMS data and (b) the SMS data for 10 virtual coils.

5.2.3 Image Artifacts

Figure 5.5 shows the interslice leakage ($L_{2\to1} + L_{2\to3}$), intraslice ($I_{2\to2} - I_2$), and total image artifact ($L_{1\to2} + I_{2\to2} + L_{3\to2} - I_2$) metrics for different acquisition and reconstruction methods versus number of virtual coils. The formulas for these metrics are given in Section 5.1.11. The metrics were computed using the full set of 39 slices in each time frame. From Figure 5.5a, it is clear that GRABSMACC-SP-SG has the least interslice leakage out of all the methods. The intraslice artifact shown in Figure 5.5b has approximately the same behavior in all methods, except for a differing baseline

level for each method. In Figure 5.5c, GRABSMACC-SG and GRABSMACC-SP-SG are the best performing SMS methods in terms of total image artifact. For all three artifact metrics, SENSE reconstruction of spiral SMS data had values reasonably similar to the ones for SENSE reconstruction of concentric ring data.

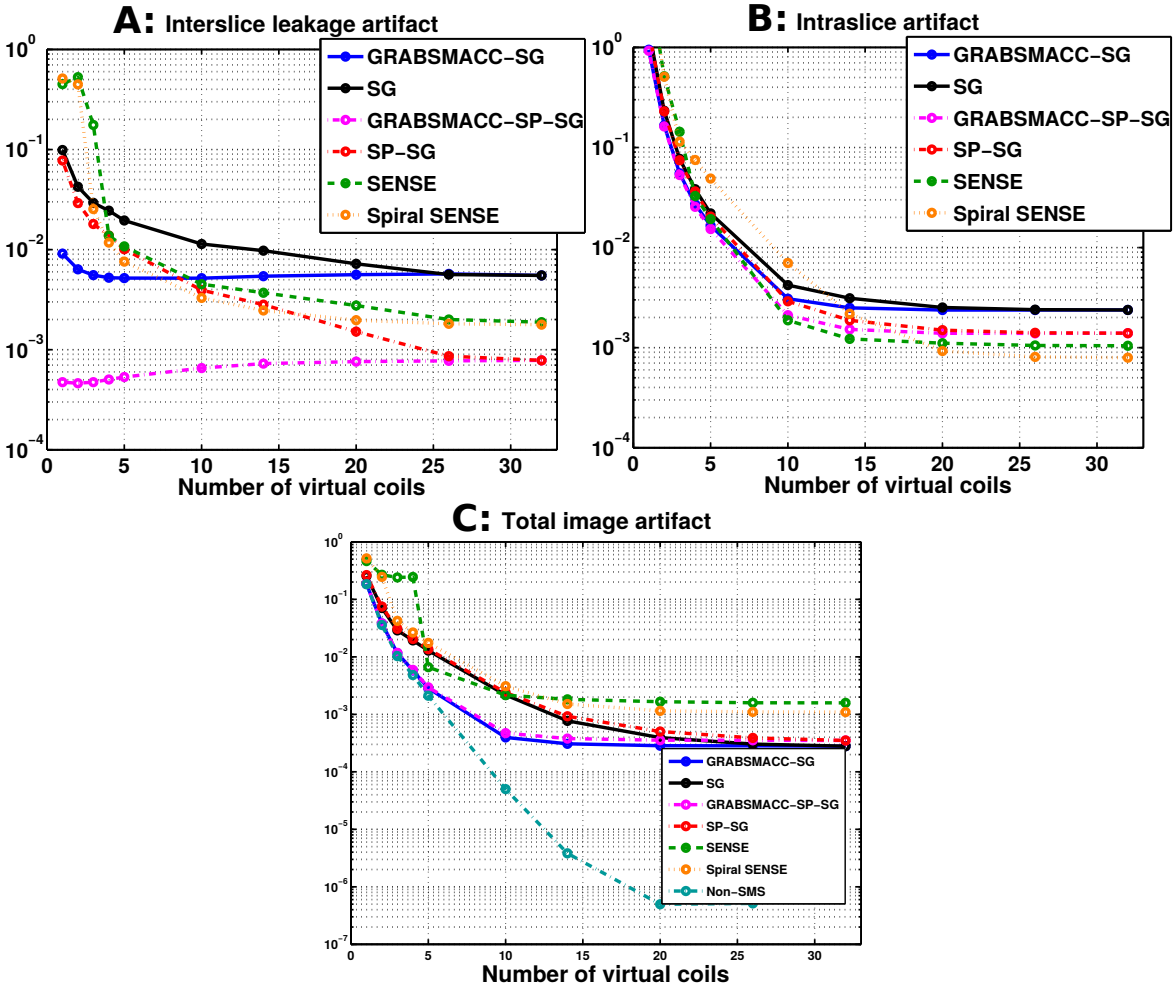

Figure 5.5: (a) Interslice leakage artifact metric ($L_{2\to1} + L_{2\to3}$), (b) intraslice artifact metric ($I_{2\to2} - I_2$), and (c) total image artifact metric ($L_{1\to2} + I_{2\to2} + L_{3\to2} - I_2$) for the middle slices of a 3-simultaneous-slice-acquired volume of 39 total axial slices. All methods used a concentric ring trajectory except for the "Spiral SENSE" method.

Figure 5.6 shows the actual interslice leakage and intraslice artifact maps for the 3 simultaneously acquired slices labeled as "Truth" on the right side. These images parallel the results in Figure 5.5; GRABSMACC-SP-SG has the least overall interslice

leakage, with similar intraslice artifact behavior in all SMS methods. The intraslice artifact in GRABSMACC-SP-SG is larger than in SENSE, but the intraslice artifact in GRABSMACC-SP-SG is mostly near the eyes and not as much in the brain, which is the area that matters the most in fMRI. The artifact maps for SENSE reconstruction of spiral data were visually very similar to the SENSE reconstruction of concentric ring data.

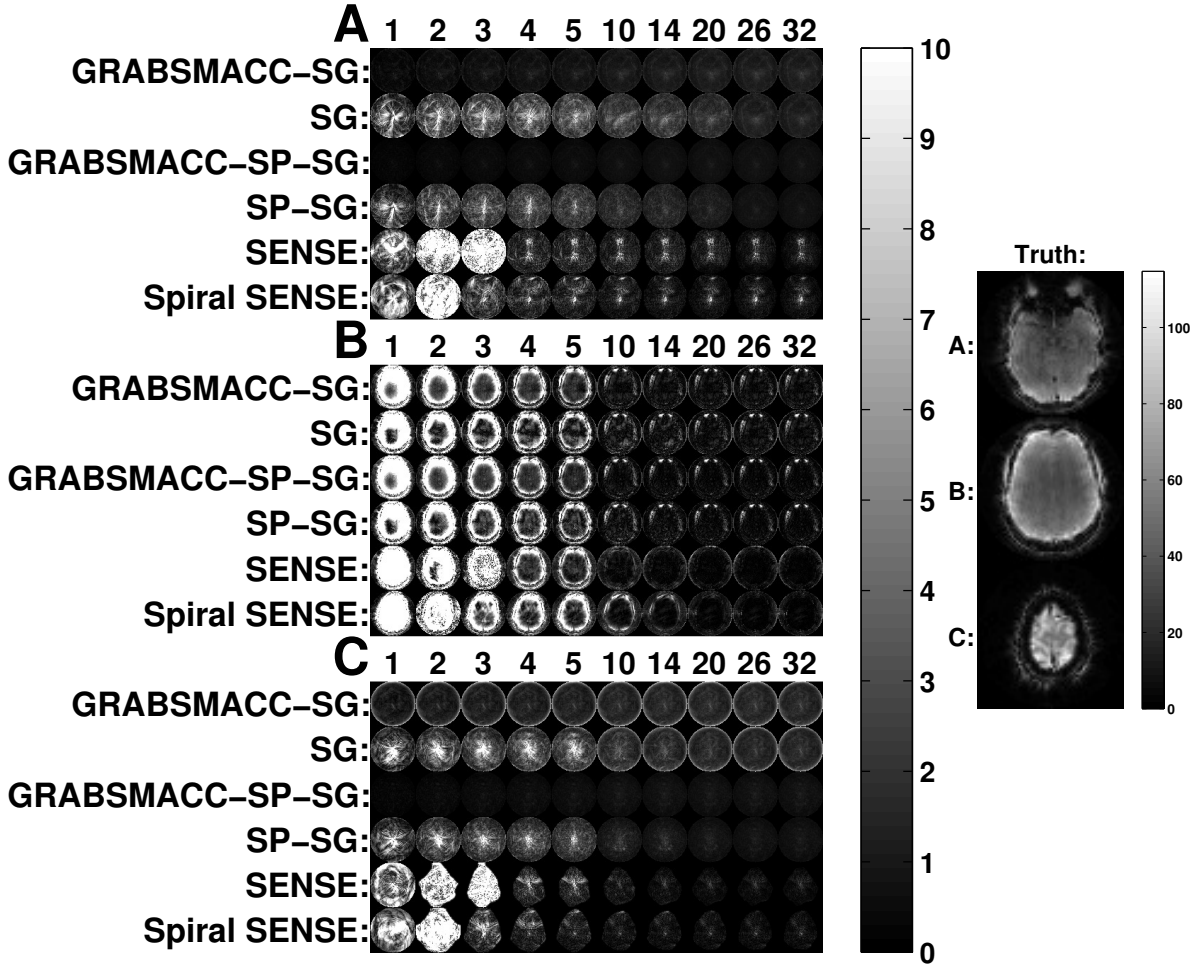

Figure 5.6: (a) Interslice leakage artifact for the inferior slice ($L_{2\to1}$), (b) intraslice artifact for the middle slice ($I_{2\to2} - I_2$), and (c) interslice leakage artifact for the superior slice ($L_{2\to3}$) from the middle slice of a 3 simultaneous slice acquisition. The image on the right shows the ground truth inferior (a), middle (b), and superior (c) slices. All methods used a concentric ring trajectory except for the "Spiral SENSE" method.

In Figure 5.5a, SP-SG exhibits less interslice leakage when compared to SG, confirming the results of Ref. [73], while SENSE falls somewhere between SG and SP-SG. Figure 5.5a clearly shows the benefit of GRABSMACC on both SG and SP-SG in terms of reduced interslice leakage artifacts with larger amounts of compression. In particular, GRABSMACC-SG and GRABSMACC-SP-SG are the only SMS reconstruction methods that do not have increased interslice leakage with larger amounts of compression. In Figures 5.6a and 5.6c, both GRABSMACC-SG and GRABSMACC-SP-SG reduce the amount of interslice leakage compared to SG and SP-SG, respectively. GRABSMACC-SP-SG does particularly well with almost no visible interslice leakage signal, especially when compared to the other 4 methods shown. In addition, Figures 5.6a and 5.6c illustrate the importance of interslice leakage on functional activation; for all methods, the leakage signal tends to concentrate more in the center of the image where brain matter is likely to be present, potentially affecting activation in the areas of most interest.

The intraslice artifact, shown in Figures 5.5b and 5.6b, is very similar between all 5 SMS reconstruction methods, and particularly so between SG and GRABSMACC-SG and between SP-SG and GRABSMACC-SP-SG. Using 20 to 32 coils, there is very little difference between SG and GRABSMACC-SG and between SP-SG and GRABSMACC-SP-SG. When going below 20 virtual coils, the GRABSMACC methods have slightly less intraslice artifact than their non-GRABSMACC counterparts. The intraslice artifact results again mirror the results in Ref. [73] in that SP-SG has reduced intraslice artifact compared to SG.

All the GRAPPA-based methods have similar total image artifact with all 32 coils, as shown in Figure 5.5c. However, SG has slightly less total image artifact compared to SP-SG, again consistent with Ref. [73], which explains that SP-SG trades off higher total image artifact for reduced leakage. Using GRABSMACC for compression reduces the total image artifact to very similar levels for both SG and SP-SG.

5.2.4 Retained SNR

Figure 5.7 shows the average retained SNR, or equivalently, average $1/g$-factor within a brain ROI that covers all 39 slices in each time frame. The GRABSMACC-SG and GRABSMACC-SP-SG plots behave the most similarly to the non-SMS plot; all three have constant SNR until around 5 virtual coils. The SNR using all 32 coils for SENSE starts out at a higher level than non-SMS, but begins to fall earlier around 14 virtual coils. The SNR for SENSE reconstruction of spiral data behaves almost identically to the SENSE reconstruction of concentric ring data. The plots for SG and SP-SG are almost the same, with an increase in SNR with 20 and 14 virtual coils. In general, the GRAPPA-based methods have a baseline retained SNR of around 0.8 to 0.85. Figure 5.8 shows retained SNR maps of the same 3 simultaneous slices used in Figure 5.6.

As mentioned in Section 4.1.7, for both SG and SP-SG, SMS acquisitions taken at non-z-isocenter locations need to be demodulated prior to the entire slice separation and reconstruction process. If this demodulation is not performed, acquisitions further away from z-isocenter will suffer an SNR loss compared to the isocenter acquisition. Figure 5.9a shows the retained SNR using SP-SG without demodulating the phase of the non-isocenter acquisitions prior to reconstruction. Each column of 3 images is a retained SNR map of the simultaneously acquired set of 3 slices from a single acquisition, and the number at the top of the images in Figure 5.9 indicates the acquisition number for that column, where acquisition 7 is at z-isocenter and acquisitions 1 and 13 are the furthest from isocenter. Figure 5.9b shows the retained SNR using SP-SG with demodulation prior to reconstruction. Note the roll-off or decrease in retained SNR in Figure 5.9a as the acquisitions move further away from isocenter. In Figure 5.9b, this does not happen and the retained SNR is more uniform; acquisitions taken at slice locations far away from isocenter still have SNR similar to the isocenter acquisition.

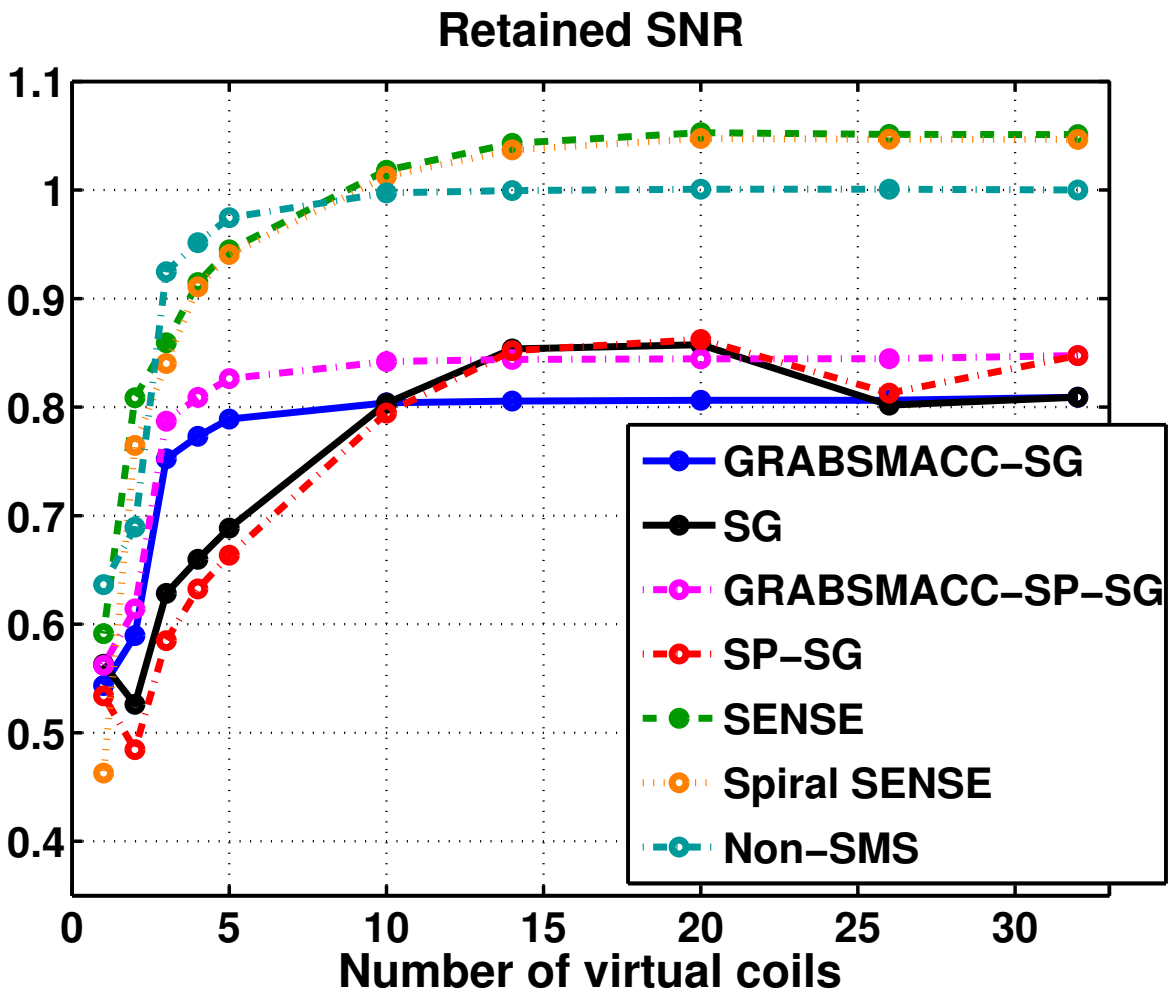

Figure 5.7: Average retained SNR, or equivalently, average $1/g$-factor within brain voxels. All methods used a concentric ring trajectory except for the "Spiral SENSE" method.

5.2.5 Computational Speed

Figure 5.10 shows the time needed for a single computer with an Intel Xeon E3-1230 3.20 GHz processor to reconstruct the first time frame of fMRI runs of subject 5, and includes the time needed for coil compression. The times for SG and SP-SG were virtually identical, as were the times for GRABSMACC-SG and GRABSMACC-SP-SG, so each of the pairs were combined into a single plot, as shown in the legend of Figure 5.10. Construction of field maps, sensitivity maps, and GRAPPA kernels

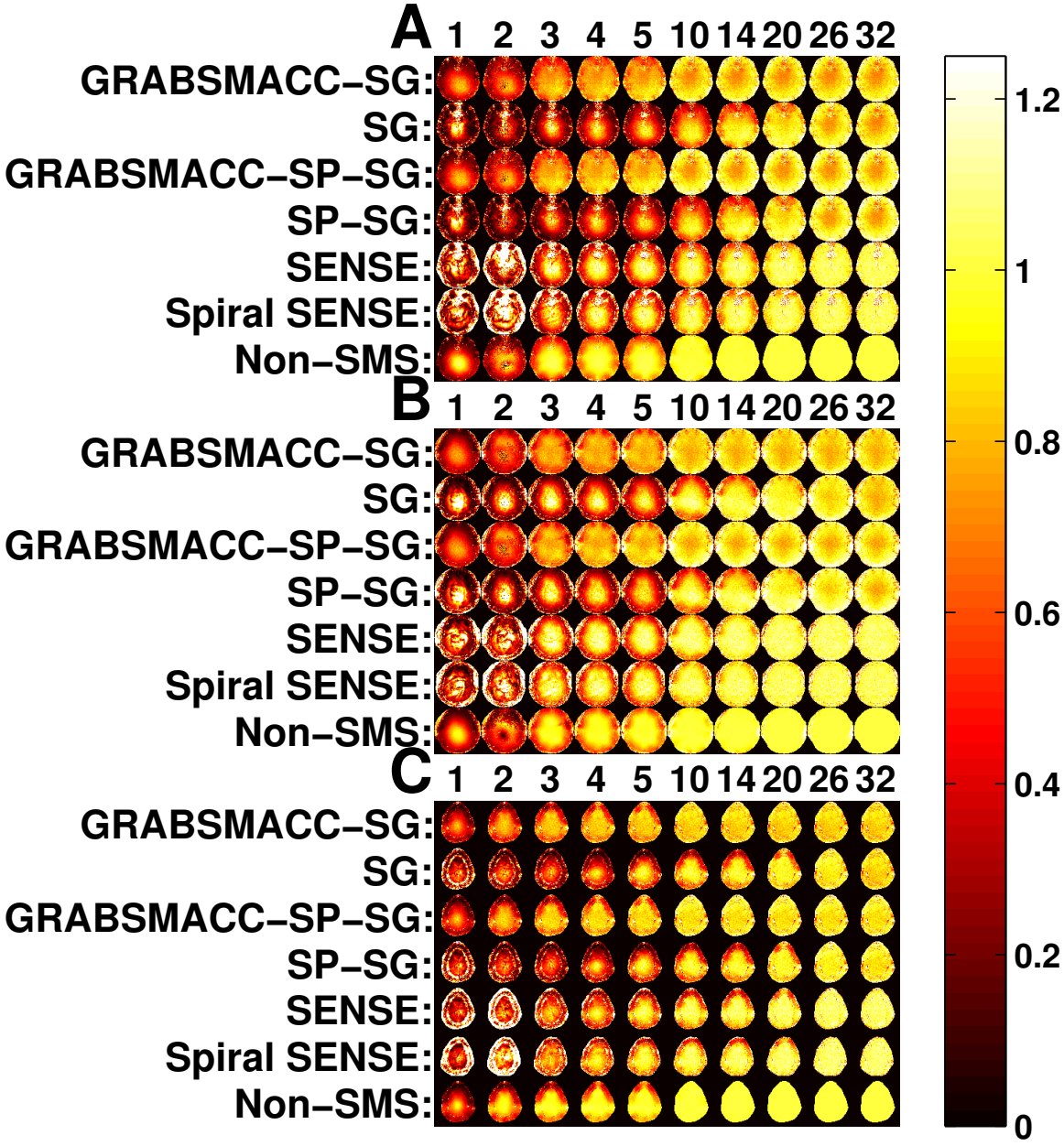

Figure 5.8: Maps of retained SNR, or equivalently, $1/g$-factor of the same slices used in Figure 5.6. (a) Inferior slice, (b) middle slice, and (c) superior slice. All methods used a concentric ring trajectory except for the "Spiral SENSE" method.

are only done once per fMRI scan, so they were not included in the times. While not insignificant, the time needed for them does not contribute as much relative to the overall time needed for reconstruction of the entire fMRI scan. In all methods,

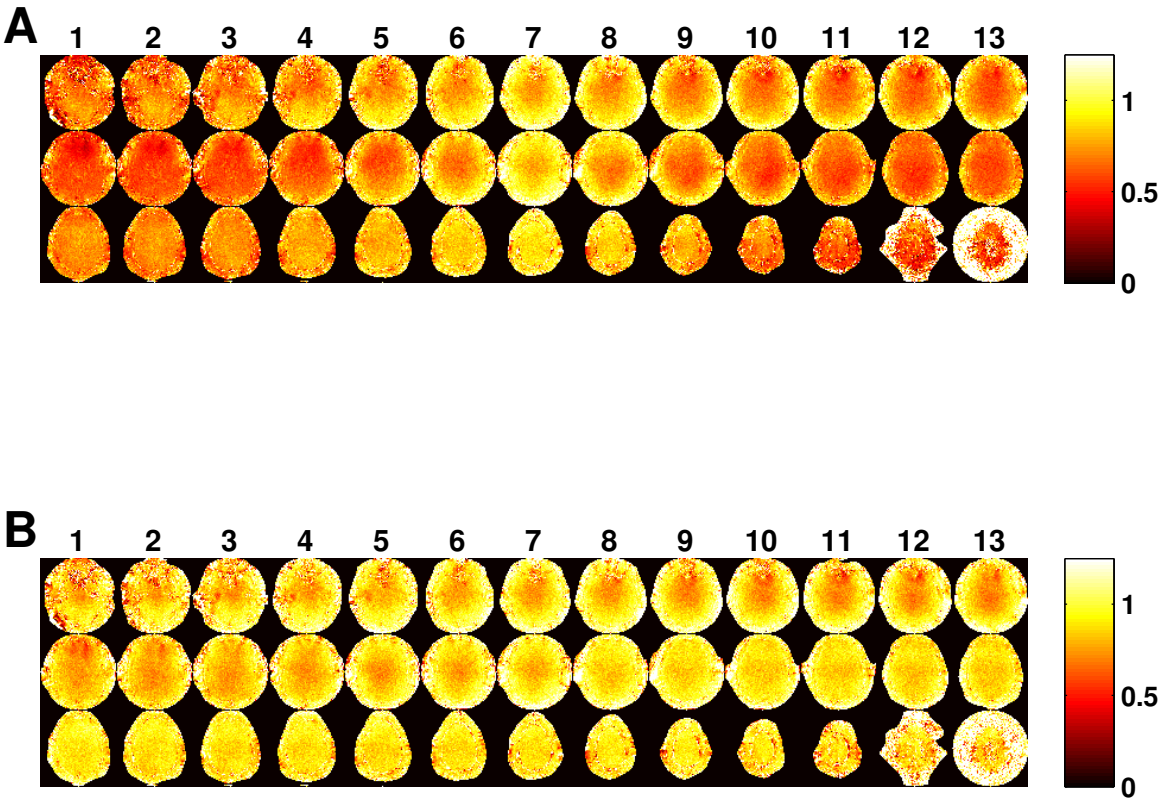

Figure 5.9: (a) Maps of retained SNR, or equivalently, $1/g$-factor without demodulating non-z-isocenter acquisitions prior to SP-SG reconstruction (with no coil compression). Each column of 3 images is the retained SNR map for a single acquisition of 3 simultaneous slices. The number at the top of each column indicates the acquisition number, where acquisition 7 is at z-isocenter and acquisition 1 and 13 are the furthest from isocenter. (b) Maps of retained SNR with appropriate demodulation prior to SP-SG reconstruction (with no coil compression).

the reconstruction time increases linearly with the number of virtual coils used. The time needed for kernel computation was around 100 seconds and 256 seconds for GRABSMACC-SG and GRABSMACC-SP-SG, respectively, regardless of the number of virtual coils used. The time needed for kernel computation ranged linearly from 4 to 100 seconds in SG, and linearly from 11 to 256 seconds in SP-SG as the number of virtual coils increased from 1 to 32.

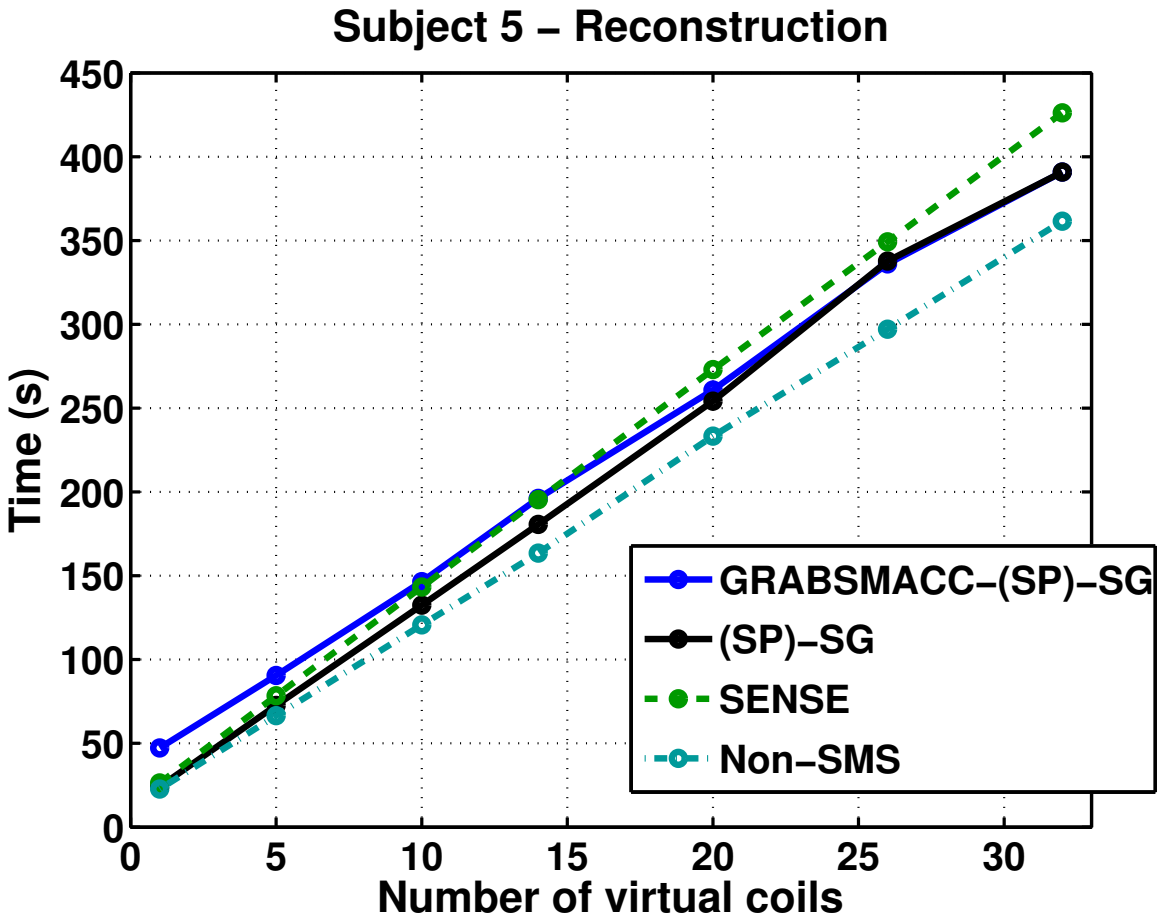

Figure 5.10: Reconstruction times of the first time frame of fMRI scans of subject 5. The time needed for field map, sensitivity map, and GRAPPA kernel generation is not included in these reconstruction times. The time needed for coil compression is included.

5.3 Discussion

5.3.1 Image Acquisition and Reconstruction

The concentric ring trajectory provides better sampling regularity for GRAPPA than a spiral, but is longer: the readout length for the same FOV and image size using a typical spiral-in is around 20.224 ms, whereas the readout length of the proposed concentric ring trajectory was 26.044 ms. The increase in length is mainly caused by the need to sample k-space with shorter intervals along the trajectory right before

and after the ring transitions, as shown in Figure 4.3b, in order to satisfy maximum gradient slew rate constraints. In addition, each ring is sampled fully along the entire circle before transitioning to the next smaller ring. Potential time savings could be had if one were to start the transition before reaching the end of the full circle, although at decrease in sampling regularity for the GRAPPA kernel. However, this readout time increase does not prevent the use of a suitable TE for BOLD imaging.

Unlike a simple FOV shift obtained with blipped-CAIPI EPI, blips using concentric rings result in a blur, as shown in Figure 4.22. Qualitatively, when compared with blipped-CAIPI, there is potentially less signal overlap of simultaneous slices because the signal is blurred throughout the entire FOV, whereas in blipped-CAIPI, there is a discrete shift. Less overlap potentially results in a better g-factor. However, using GRAPPA with non-Cartesian trajectories inevitably introduces certain distortions in the reconstruction due to the Cartesian approximation of a non-Cartesian trajectory that occurs when unwrapping the constant angular velocity rings into Cartesian grids. In Ref. [40], the $1/g$ maps for blipped-CAIPI spin-echo-EPI with 3 simultaneous slices averaged around 0.997, whereas the non-blipped version averaged around 0.68. Using our blipped concentric rings, GRABSMACC-SP-SG resulted in an average $1/g$ of around 0.85, which is not as high as the blipped-CAIPI results in Ref. [40], but still higher than non-blipped SMS. Using SENSE resulted in an average $1/g$ of over 1 using our blipped concentric rings, possibly because the conjugate gradient algorithm was not run quite to convergence, which could result in slight smoothing not obvious visually. Thus, it is likely that the Cartesian approximation in the GRAPPA-based methods reduced the retained SNR. The retained SNR, a measure of thermal noise, is not the only metric that should be considered when evaluating a method for fMRI. While the decrease in $1/g$ is not insignificant, Ref. [54] argues that physiological noise and not thermal noise dominates in many studies. As shown in Figure 5.5a, GRABSMACC-SP-SG results in less interslice leakage compared to SENSE, with

fewer false activations in neighboring simultaneous slices. In addition, signal recovery in the presence of in-plane susceptibility-induced gradients may show that the concentric-ring-in trajectory may have utility when imaging in inferior regions of the brain.

In this work, a concentric ring trajectory was chosen to enhance sampling regularity for GRAPPA compared to non-Cartesian trajectories such as spirals. Another benefit of concentric rings is that they are amenable to in-plane acceleration using GRAPPA. Single-shot acquisitions can easily be constructed for higher sampling density, while multishot acquisitions would better match B_0 phase evolution. If multiple interleaves are acquired, gross movement or physiological motion between excitations can easily degrade the quality of the calibration, although recent work has reduced the sensitivity losses from these issues in accelerated parallel EPI [86].

5.3.2 Functional Activation and Image Artifacts

Comparing the activation counts of SG and GRABSMACC-SG in Figure 5.2a, SG appears to outperform GRABSMACC-SG since the count for SG increases as the number of virtual coils is decreased from 32. One explanation is that autocorrelation in the data for SG increased as the number of virtual coils initially decreased from 32, resulting in a reduction in the effective degrees of freedom and a difference in the actual t-score significance threshold. Since the threshold was fixed at $t > 6$, this resulted in an artificially increased number of activated voxels for SG. Comparing SP-SG and GRABSMACC-SP-SG in Figure 5.2a and 5.2c, GRABSMACC-SP-SG is clearly superior to SP-SG in both true and false activation counts. The false activation behavior seems to be strongly related to the interslice leakage artifact results in Figures 5.5a, 5.6a, and 5.6c, since activation from one slice can leak into another.

Although interslice leakage can affect the false activation, intraslice artifacts also

contribute. For example, in Figure 5.2c, GRABSMACC-SG exhibits less false activation than SP-SG at all levels of compression, while in Figure 5.5a, GRABSMACC-SG has a higher amount of interslice leakage than SP-SG for ≥ 10 virtual coils. However, the total image artifact shown in Figure 5.5c, which contains both interslice and intraslice artifacts, shows that GRABSMACC-SG has less total artifact than SP-SG for all levels of compression, similar to the false activation results. It should also be mentioned that the false activation in Figure 5.2c is computed from all 39 slices, whereas the artifact results in Figure 5.5 are not computed from all the slices; in Figure 5.5a the interslice leakage is from the middle block of 13 slices out to the superior and inferior blocks of 13, Figure 5.5b displays the intraslice leakage for just the middle block of 13 slices, and Figure 5.5c contains interslice leakage from the superior and inferior blocks into the middle block of 13, along with intraslice leakage for the middle block.

Also of importance is the general trend of false activation for each method in Figure 5.2c. With GRABSMACC-SG and GRABSMACC-SP-SG, it is reassuring that activation results will likely not be falsely elevated with coil compression. Excessive amounts of compression will likely hinder GRABSMACC's ability to detect true activation, but it does not seem to cause false activation and lead to false positive conclusions on brain function. On the other hand, SG, SP-SG, and SENSE all result in increased false activation with increasing compression. Also interesting is how similar the shape of the curves for GRABSMACC-SG and GRABSMACC-SP-SG are to the shape of the curve for non-SMS in Figures 5.2a and 5.2c. In this respect, GRABSMACC mimics the non-SMS ideal much better than the other SMS reconstruction methods.

In Figure 5.5a, the interslice leakage mostly increases with a decreasing number of virtual coils, but this is not the case for GRABSMACC-SG and GRABSMACC-SP-SG, both of which exhibit a very slight decrease in interslice leakage when the number

of virtual coils is very low. As explained by Ref. [73], there is a trade off between interslice and intraslice artifacts for SMS imaging. Compared to SP-SG, SG trades off higher interslice error for lower total artifact error, whereas SP-SG trades off higher total artifact error for lower interslice error. Furthermore, the interslice and intraslice error trade off can be tuned with weighting parameters in SP-SG. In Figure 5.5a, the very slight decrease in interslice leakage with lower numbers of virtual coils in GRABSMACC-SG and GRABSMACC-SP-SG are likely coming at the expense of increased intraslice error. The monotonically increasing total image artifact with decreasing coils shown in Figure 5.5c confirms this effect for all methods. Perhaps the virtual coil sensitivities created by the GRABSMACC methods at low numbers of virtual coils exhibit very good variation in the through-plane direction, but not as adequately in-plane, which generates better slice separation but worse intraslice artifact.

5.3.3 SNR

In general, the SNR plots in Figure 5.7 behave similarly to the activation count plots in Figure 5.2a. Perhaps the most surprising feature of the SNR plots is that the SNR for SG and SP-SG is higher at 14 and 20 virtual coils when compared to using all 32 coils. The SNR for SENSE also increases slightly at 20 virtual coils, although to a lesser extent than SG and SP-SG. This behavior is perhaps explained by the interslice leakage of these methods. It is possible that the increased interslice leakage artifact for these methods creates an artificial, "stationary" signal in the images, resulting in a higher signal with the same level of standard deviation and hence a higher calculated SNR. However, once the number of virtual coils is reduced below 14, the overall degradation in the underlying image begins to outweigh any of the artificial changes that the interslice leakage produced. Notice that GRABSMACC-SG and GRABSMACC-SP-SG exhibit no increases in interslice leakage from 32 to

5 coils, and so the SNR remains almost constant from 32 to 5 coils. In particular, note that non-SMS has absolutely no interslice leakage, and the shape of the SNR plot for non-SMS in Figure 5.7 is very similar to the shape of the SNR plots for GRABSMACC-SG and GRABSMACC-SP-SG.

5.3.4 Demodulation of Non-isocenter Slices

The retained SNR behavior shown in Figure 5.9a can be explained by examining the phase imparted by the readout blipped z-gradient for both isocenter and non-isocenter SMS acquisitions. For illustration, assume that each ring has a total magnitude of 1, and that the phase of each ring is solely dependent on the readout z-gradient and the slice location. The phase imparted by the z-gradient is just $2\pi z_v k_z(t)$, where z_v is the distance of the slice to z-isocenter and $k_z(t) = \frac{\gamma}{2\pi}\int_0^t g_z(\tau)\,\mathrm{d}\tau$. For $n_{\mathrm{slc}} = 3$ simultaneous slices, $k_z(t)$ for each ring cycles through $\Delta k_z = \frac{1}{\mathrm{FOV}_z} = \frac{1}{n_{\mathrm{slc}} n_{\mathrm{acq}} d_{\mathrm{slc}}}$, $-\Delta k_z$, 0, then back through again. Numbering consecutive slices in the $n_{\mathrm{slc}} n_{\mathrm{acq}} = 39$ slice volume 1 through 39, the isocenter SMS acquisition includes slices 7, 20, and 33, where slice 20 is at isocenter. For slice 7, the outermost ring has a complex value of $e^{i2\pi z_v/(n_{\mathrm{slc}} n_{\mathrm{acq}} d_{\mathrm{slc}})} = e^{i2\pi(20-7)/(3\cdot 13)} = e^{i2\pi\frac{1}{3}}$. The next consecutive ring has a complex value of $e^{i2\pi(-1)(20-7)/(3\cdot 13)} = e^{-i2\pi\frac{1}{3}}$. Finally, the third ring from the outside has a value of $e^{i0} = 1$ since $k_z(t) = 0$ for the third ring. Slice 20 is at z-isocenter, so the value for each ring is just 1. For slice 33, the outer ring is $e^{i2\pi z_v/(n_{\mathrm{slc}} n_{\mathrm{acq}} d_{\mathrm{slc}})} = e^{i2\pi(20-33)/(3\cdot 13)} = e^{-i2\pi\frac{1}{3}}$, the next ring is $e^{i2\pi(-1)(20-33)/(3\cdot 13)} = e^{i2\pi\frac{1}{3}}$, and the third ring is again 1. The sum across the 3 rings is 0, 3, and 0 for slices 7, 20, and 33, respectively. Therefore, for the isocenter acquisition, there is substantial cancellation of signals from the outer slices, making it easier to suppress these slices. Table 5.2 shows the same calculation for acquisition 1, which consists of slices 1, 14, and 27. With this non-isocenter acquisition, there is much less cancellation in the outer slices, making the slice separation process more poorly conditioned.

	Slice 1	Slice 14	Slice 27
Ring 1:	$e^{i2\pi 19/39}$	$e^{i2\pi 6/39}$	$e^{-i2\pi 7/39}$
Ring 2:	$e^{-i2\pi 19/39}$	$e^{-i2\pi 6/39}$	$e^{i2\pi 7/39}$
Ring 3:	e^{i0}	e^{i0}	e^{i0}
Sum:	-0.994	2.136	1.857

Table 5.2: Assuming that each ring has a total magnitude of 1, and that the phase for each ring is only dependent on g_z and the slice location, this table plots the complex value for each ring and slice for acquisition 1, which is the furthest away from z-isocenter and consists of slices 1, 14, and 27. The sum across the 3 rings is also shown for each slice.

Figure 5.11 plots the complex sum across rings for all $n_{\text{acq}} = 13$ acquisitions. For acquisition 7 at isocenter, the sum for the middle slice is 3 and the inferior and superior slices are both 0. As the acquisition moves away from isocenter, one of either the inferior or superior slices has a value much closer to that for the middle slice. This makes it more difficult to separate the middle slice from the closer of the other 2 slices, which causes errors in the slice separation process, leading to lower SNR. As the acquisitions move further and further away from isocenter, the value between the middle slice and either the inferior or superior slice gets closer, which is why the retained SNR decreases as the acquisitions move further away from isocenter in Figure 5.9a. In addition, the signal cancellation in the outer slices becomes less as the acquisitions move further away from isocenter, which makes the conditioning for separation worse and worse.

Note that both the inferior and superior slices are 0 for the isocenter acquisition, which could potentially imply that it would be difficult to separate them. However, the inferior and superior slices are twice as far apart from each other as they are to the middle slice, which enables the difference in coil sensitivities to cleanly separate them, even if they have very similar values. Because of the coil configuration, the difference in value between the middle and either the inferior or superior slice is more important for separation.

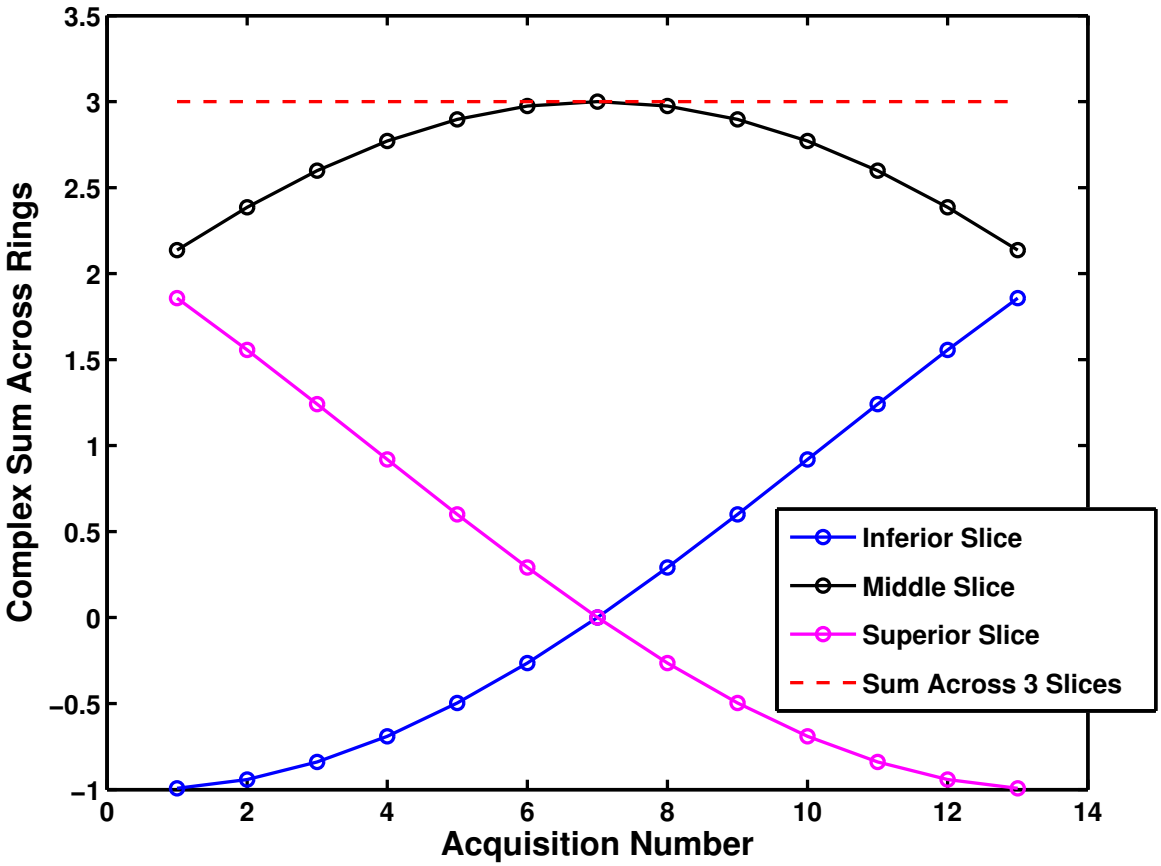

Figure 5.11: This plot displays the complex sum across $n_{\text{slc}} = 3$ consecutive rings, assuming each ring has a total magnitude of 1 and the phase of each ring only depends on the blipped readout z-gradient and the slice location. Acquisition 7 occurs with the middle slice at z-isocenter, and acquisitions 1 and 13 are the furthest away from isocenter. For each acquisition, the sum across the $n_{\text{slc}} = 3$ simultaneous slices is also plotted and is equal to 3. Note that for acquisition 7 at z-isocenter, the middle slice has a value the furthest away from the inferior and superior slices.

Fortunately, there is an easy fix for this behavior. Simply demodulate the k-space data prior to kernel weight computation and reconstruction as described in Section 4.1.7, and the complex value of the middle slice will be maximally different from the other 2 slices for all acquisitions. After demodulating the non-isocenter data, all $n_{\text{acq}} = 13$ acquisitions will have a similar complex sum as acquisition 7 in Figure 5.11. This preserves the retained SNR for non-isocenter locations, as shown in Figure 5.9b.

5.3.5 Enhanced Compression Performance with GRABSMACC

The results in Table 5.1 indicate a significant improvement in coil compression activation performance with GRABSMACC when compared to either SENSE, SG, or SP-SG. SENSE requires at least 2 to 3 times as many virtual coils as either GRABSMACC-SG or GRABSMACC-SP-SG for an equivalent activated voxel count degradation. Although SG and SP-SG perform better than SENSE, the addition of GRABSMACC to these methods further increases their performance. The better preservation of activation using GRABSMACC allows higher levels of compression to be used, which significantly decreases the reconstruction time.

Taking into account all the results, GRABSMACC-SP-SG likely has the best preservation of activation out of all the SMS reconstruction methods for the purposes of most fMRI studies. SG, SP-SG, and SENSE exhibit worrying false activation and increased interslice leakage with compression. GRABSMACC-SP-SG has the least interslice leakage, which is perhaps the most important out of all the artifacts since it has the most potential for generating erroneous activation. In terms of SNR, SENSE comes out on top. However, the amount of SNR that GRABSMACC-SP-SG does possess is clearly enough to detect activation in a normal functional study. Furthermore, the SNR is better preserved with higher amounts of compression when compared to SENSE.

The better compression for GRABSMACC and non-SMS can be explained from the $\boldsymbol{V}_{\text{comp}}$ matrices. With these two methods, a different $\boldsymbol{V}_{\text{comp}}$ matrix is computed for each of the $n_{\text{tot}} = n_{\text{slc}} n_{\text{acq}}$ number of individual slices. The SVD selects the best possible set of linear combinations of coils to use for each individual slice, in fact tailoring the compression for each target solution. However, with SENSE, SG, and SP-SG, only n_{acq} number of $\boldsymbol{V}_{\text{comp}}$ matrices are used, which amounts to one $\boldsymbol{V}_{\text{comp}}$ matrix for each set of $n_{\text{slc}} = 3$ individual slices. The $\boldsymbol{V}_{\text{comp}}$ matrices are computed

from "source" data consisting of the sum of 3 slices, which may not result in the best set of linear combinations to use for the individual target slices. In SMS imaging, the $n_{\text{slc}} = 3$ simultaneously acquired slices are separated from each other by some distance in the through-plane direction for decreased geometry factor. This separation in space results in an SMS signal that is the sum of 3 very different objects, as shown in Figure 5.12.

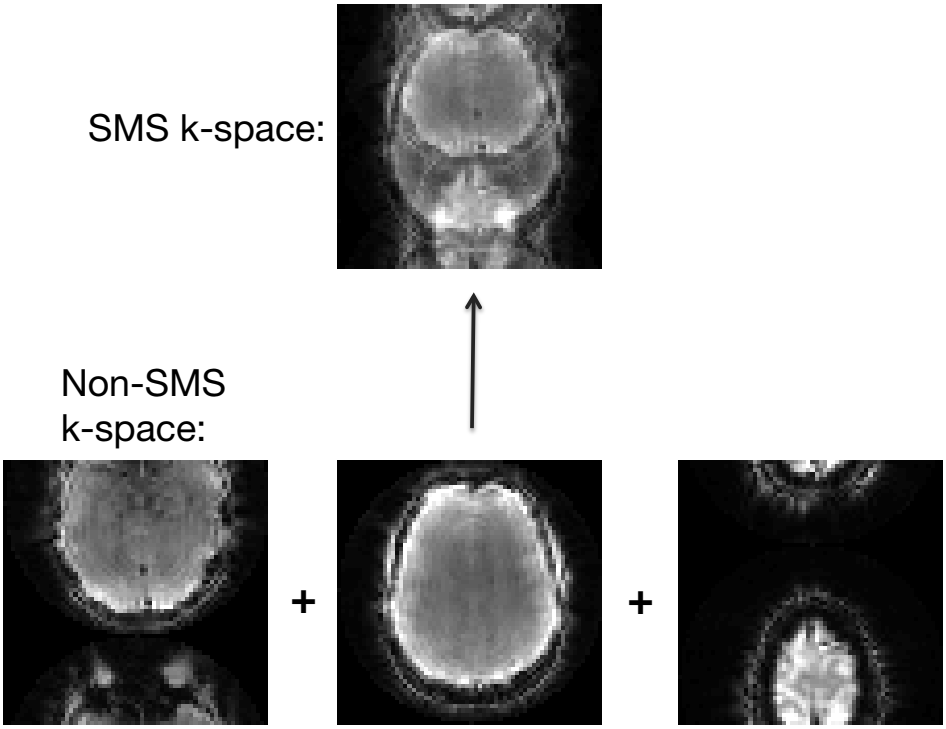

Figure 5.12: In conventional coil compression, $\boldsymbol{V}_{\text{comp}}$ is computed from the SMS k-space data, which is the sum of 3 slices spatially separated far apart from each other. Before sensitivity maps are computed or kernel calibration is performed, each non-SMS slice is compressed using the *same* $\boldsymbol{V}_{\text{comp}}$. In GRABSMACC, $\boldsymbol{V}_{\text{comp}}$ is computed from the *non*-SMS k-space data. For sensitivity maps or kernel calibration, each non-SMS slice is compressed using a *different* $\boldsymbol{V}_{\text{comp}}$ that is tailored for that specific slice.

5.3.6 Data Storage

Although GRABSMACC outperforms standard coil compression in SMS reconstruction, it does not decrease the amount of storage needed for raw data archival, if desired. The full set of original 32 coils are used in GRABSMACC to reconstruct images in a virtual coil basis, so the raw k-space data cannot be compressed and saved at a smaller size for later reconstruction. On the other hand, with standard coil compression, raw data can be compressed and saved, but the standard process is still a form of lossy compression. If enough of the signal of interest is not maintained, it cannot be recovered once the original data is deleted.

5.3.7 Reconstruction Speed

The reconstruction times for GRABSMACC shown in Figure 5.10 do not differ much from SG and SP-SG at 26 and 32 coils, and actually increase slightly above the times needed for SG and SP-SG as the number of virtual coils is reduced below 26. This is because the $\boldsymbol{W}$ matrix has bigger dimensions in GRABSMACC than in standard coil compression, resulting in slightly slower k-space separation. However, the $\boldsymbol{W}$ matrix only needs to be determined once per fMRI run or once for the entire fMRI study. The main bottleneck for image reconstruction in GRABSMACC, SG, and SP-SG is the iterative conjugate gradient routine that transforms separated k-space data into the image domain, and not the k-space domain slice separation process using the kernels in W, which is just a simple matrix vector multiplication. For example, in GRABSMACC-SP-SG with all 32 coils using a single computer with an Intel Xeon E3-1230 3.20 GHz processor, the kernel convolution step takes a total of around 21 seconds for 1 time frame, and the remaining 370 seconds is used for multiple conjugate gradient routines transforming k-space data for each coil into the image domain. Therefore, at each matching virtual coil position in Figure 5.10, GRABSMACC takes

longer than SG and SP-SG, but not by much compared to the total time needed. On the other hand, unlike the GRAPPA-based methods, SENSE uses conjugate gradient once, albeit on a larger problem, to separate the slices directly into the image domain. For this reason, GRABSMACC becomes ever so slightly slower than SENSE at 14 virtual coils and below. We also note that while non-Cartesian SENSE most likely requires the use of an iterative reconstruction, GRABSMACC can easily be implemented with a non-iterative reconstruction like the conjugate phase reconstruction [87], which would substantially decrease the reconstruction time even further.

The main benefit of GRABSMACC over standard coil compression in SG, SP-SG, and SENSE is better preservation of activation with the reduction in number of virtual coils. Since activation is preserved so much better in GRABSMACC versus the other methods, a much smaller number of virtual coils can be used in GRABSMACC with equivalent activation performance but less computational burden. For example, GRABSMACC-SP-SG with 10 virtual coils results in essentially the same activation as with all 32 coils, no increase in false activation, no increase in interslice leakage, no decrease in SNR and negligible increase in intraslice and total image artifact. For SENSE, one would need 20 virtual coils for activation and SNR to remain unaffected compared to using all 32 coils, although the interslice leakage is increased. From Figure 5.10, GRABSMACC-SP-SG with 10 virtual coils takes about 54% as long as SENSE with 20 virtual coils, which translates to time savings on the order of several hours when reconstructing multiple fMRI studies. A similar argument can be made when comparing GRABSMACC-SP-SG to SP-SG, with the added fact that SP-SG has even more interslice leakage when compared to using 32 coils, and likely more false activation as well.

5.4 Conclusions

Coil compression is frequently used to reduce the computational time and memory required to reconstruct parallel imaging data and becomes increasingly beneficial as the number of coils increases. GRABSMACC is a practical method for coil compression in SMS fMRI and retains functional activation better than standard coil compression techniques used with SMS imaging and reconstruction. Experiments presented indicate that SMS fMRI scans using 32 receive coils and 3 simultaneous slices can be compressed down to approximately 31% of their original size without any significant loss of functional activity.

CHAPTER 6

Conclusions

SMS imaging can be an effective method to accelerate fMRI and improve the temporal or spatial resolution of the data. Once the data is acquired, the problem becomes one of separating the slices. In this work, both non-parallel SMS fMRI and parallel SMS fMRI was explored using efficient non-Cartesian k-space trajectories. These methods use different techniques to distinguish simultaneous slices so that subsequent separation is easier. Hadamard-encoding, the non-parallel method examined in this work, distinguishes simultaneous slices in the temporal frequency domain. Parallel SMS imaging methods distinguish slices spatially. Each of these methods has their advantages and disadvantages.

6.1 Hadamard-encoded fMRI

In fMRI, activation is detected using temporal fluctuations in the images. Hadamard-encoding introduces an additional temporal fluctuation into the data as the sole means of differentiating one slice from another. This can be problematic since there are many sources, both known and unknown, of undesired temporal fluctuations during fMRI. Physiological noise is one such source that can be monitored during scanning and potentially removed. However, no physiological noise correction method is guaranteed to remove the noise entirely, and the leftover fluctuations not only corrupt the activation as in conventional fMRI, but also produce errors during slice separation. It does

show some potential benefit as a way to reduce signal dropout from through-plane dephasing, but as an acceleration method for increased temporal resolution, the gains are modest since a temporal low-pass filter is required for slice separation. In fact, the temporal resolution gain can never be greater than a factor of two, no matter how many slices are acquired simultaneously. For these reasons, Hadamard-encoded fMRI did not show much benefit over conventional non-SMS fMRI in this work.

6.2 Non-Cartesian Parallel SMS fMRI

Parallel SMS imaging, on the other hand, distinguishes between slices by taking advantage of their differences in location. This group of methods relies heavily on the coil configuration since the difference in sensitivity profiles is the only thing differentiating one simultaneous slice from another. For this reason, a readout z-gradient is typically used to provide additional encoding in the through-plane direction. However, this merely converts the through-plane undersampling problem into an in-plane one; even with a readout z-gradient, there still needs to be sensitivity variation in-plane for clean slice separation. The temporal resolution increase is much greater than what is possible with Hadamard-encoding since data from only a single time frame is used for reconstruction of that frame. However, the expense and availability of parallel receive hardware is obviously needed. In addition, parallel SMS imaging also suffers from increasing RF energy deposition with larger acceleration factors. This is currently an area of active research and deserves future work.

6.3 GRABSMACC

Another disadvantage of parallel SMS fMRI over non-parallel ones such as Hadamard-encoding is the factor of d increase in computational effort, where d is the number of receive coils used. Although computation has become less expensive, the factor of 32

increase in data from the concentric ring SMS fMRI scans done in this work is not trivial. Depending on the acceleration factor used, not all 32 coils may be required for good slice separation. For this reason, coil compression methods can greatly improve the efficiency of reconstruction. In this work, GRABSMACC was presented. GRABSMACC does not reduce the number of coils in the raw data used in reconstruction, but only reduces the number of coils in the separated k-space slices. Although this may not seem like it would reduce computational efficiency, it was shown that GRABSMACC was able to retain activation performance at larger compression factors than conventional coil compression used in either SENSE or GRAPPA-based methods. As the benefits of iterative algorithms have become more widely known, the k-space to object domain transformation process has become the bulk of the computational effort during reconstruction. Therefore, a reduction in coils of separated k-space data has the potential to greatly accelerate reconstruction, especially if a fewer number of coils are needed to preserve activation when compared to conventional compression methods.

6.4 Contributions

6.4.1 Hadamard-encoded fMRI

This work explored the use of Hadamard-encoded SMS as a method for reduced signal dropout. It was determined that separating subslices first, then recombining them afterwards results in more recovered signal in regions with through-plane dephasing when compared to the incoherent sum method from Ref. [30]. An SNR analysis was performed using both thermal and physiologic noise sources and determined to depend on both the temporal low-pass filter cutoff and the amount of through-plane dephasing, which was not accounted for in Ref. [30].

The possibility of using Hadamard-encoded SMS as a non-parallel method for

accelerating fMRI and providing an increased temporal resolution was also explored. Since Hadamard-encoding introduces a temporal fluctuation in the time series data occurring at the Nyquist frequency, a RETROICOR-based method was developed to correct for physiological noise while preserving the desired Hadamard-encoding. An objective comparison of activation test-retest reliability between Hadamard-encoded SMS fMRI and conventional non-SMS fMRI was provided. Although Hadamard-encoded fMRI proved not to be a reliable way to increase temporal resolution, it was important to establish this to prevent future misuse.

6.4.2 Non-Cartesian Parallel SMS fMRI

This work developed a novel blipped concentric ring trajectory that increases the usability of GRAPPA-based reconstruction methods for non-Cartesian SMS fMRI. Due to the similarity between concentric ring and spiral trajectories, the concentric ring trajectory shares many of the same benefits that spirals have over Cartesian single-shot imaging such as EPI. A numerical algorithm based on ideas in Ref. [71] was created to generate the gradient waveforms for the blipped concentric ring trajectory and provides the flexibility of designing blipped concentric ring trajectories for an arbitrary number of simultaneous slices and in-plane resolution.

This work developed the concept of a modulation PSF, which is an objective way to determine the performance of the readout z-gradient waveform used in SMS imaging. This concept provides an intuitive way to understand why some waveforms, such as the sinusoid used in this work for spiral SMS imaging, do not work as well as others, such as a properly blipped waveform. The novel blipped concentric ring trajectory was also shown to have a superior modulation PSF when compared to blipped spirals, which results in less image overlap with SMS acquisitions and better slice separation.

A novel non-Cartesian slice-GRAPPA method based on Ref. [72] was also de-

veloped and shown to provide low RMSE compared to SENSE, along with good subjective visual appearance in the reconstructed images. The feasibility of accelerated fMRI using non-Cartesian GRAPPA-based reconstruction of SMS imaging was also demonstrated.

For SENSE reconstructions of SMS imaging, a novel regularization method was introduced that uses different regularization parameters for different slices, redistributing noise in the reconstruction and providing better subjective image quality.

6.4.3 Coil Compression in Parallel SMS fMRI

GRABSMACC, a novel coil compression method for either non-Cartesian or Cartesian SMS fMRI, was developed and shown to be a practical method that has better performance with greater amounts of compression compared to conventional coil compression methods in SMS imaging. Detailed statistical analysis of activation performance on multiple subjects was performed and compared with the activation performance using conventional coil compression in SMS imaging. In addition, the interslice leakage, intraslice, and total image artifacts were examined using GRABSMACC and all competing methods with numerous levels of compression. The better performance of GRABSMACC also illustrates the importance of being able to use GRAPPA-based reconstruction on non-Cartesian SMS imaging and therefore increases the importance of blipped concentric rings for high quality SMS imaging with fast reconstruction.

The coil compression performance in conventional, non-SMS fMRI was also examined and compared with GRABSMACC and conventional coil compression in SMS fMRI. Therefore, in addition to validating GRABSMACC, this work provides useful information for the vast majority of fMRI practitioners who continue to use conventional non-SMS imaging.

6.5 Future Work

6.5.1 Readout z-gradient Optimization in SMS Imaging

The modulation PSF concept developed in Section 4.2.1 provides a powerful way to evaluate and perhaps design readout z-gradient waveforms for use in SMS imaging. In Section 4.2.1, the modulation PSF was defined as the $\boldsymbol{q}$ such that

$$\boldsymbol{Qq} = \boldsymbol{MQe}_j, \tag{6.1}$$

where $\boldsymbol{Q}$ is the Fourier transform operator, $\boldsymbol{M}$ is a diagonal matrix containing the phase modulation imparted by the z-gradient, and $\boldsymbol{e}_j$ is the point. Since $\boldsymbol{M}$ is diagonal, Equation (6.1) can be written as

$$\boldsymbol{Qq} = \text{diag}\{\boldsymbol{Qe}_j\}\boldsymbol{m}, \tag{6.2}$$

where diag$\{\boldsymbol{x}\}$ is a function that creates a diagonal matrix using the entries of the vector $\boldsymbol{x}$ as the diagonal entries, and $\boldsymbol{m}$ is a vector consisting of the diagonal entries in $\boldsymbol{M}$. Solving for $\boldsymbol{m}$, we have

$$\boldsymbol{m} = \text{diag}\{\boldsymbol{Qe}_j\}^{-1}\boldsymbol{Qq}. \tag{6.3}$$

Note that diag$\{\boldsymbol{Qe}_j\}$ is easily invertible since it is diagonal. From Equation (2.20),

$$\boldsymbol{m} = \exp(-i2\pi\gamma z_v \boldsymbol{Lg}\Delta t), \tag{6.4}$$

where $\boldsymbol{L}$ is a lower triangular matrix of ones that performs a cumulative sum, $\boldsymbol{g}$ is a vector containing the discretized readout z-gradient, Δt is the time between each discrete z-gradient sample, and z_v is the distance between the slice in $\boldsymbol{q}$ and

z-isocenter. Using Equations (6.3) and (6.4), we have

$$-i2\pi\gamma z_v \Delta t \boldsymbol{L}\boldsymbol{g} = \log(\mathrm{diag}\{\boldsymbol{Q}\boldsymbol{e}_j\}^{-1}\boldsymbol{Q}\boldsymbol{q}). \tag{6.5}$$

Therefore, for 3 simultaneous slices located at positions z_1, z_2, and z_3 away from isocenter, we have the relation

$$-i2\pi\gamma\Delta t \begin{bmatrix} z_1\boldsymbol{L} \\ z_2\boldsymbol{L} \\ z_3\boldsymbol{L} \end{bmatrix} \boldsymbol{g} = \begin{bmatrix} \log(\mathrm{diag}\{\boldsymbol{Q}\boldsymbol{e}_j\}^{-1}\boldsymbol{Q}\boldsymbol{q}_1) \\ \log(\mathrm{diag}\{\boldsymbol{Q}\boldsymbol{e}_j\}^{-1}\boldsymbol{Q}\boldsymbol{q}_2) \\ \log(\mathrm{diag}\{\boldsymbol{Q}\boldsymbol{e}_j\}^{-1}\boldsymbol{Q}\boldsymbol{q}_3) \end{bmatrix} \tag{6.6}$$

for modulation PSFs $\boldsymbol{q}_1$, $\boldsymbol{q}_2$, and $\boldsymbol{q}_3$, respectively.

To design a suitable z-gradient waveform given desired modulation PSFs $\boldsymbol{q}_1$, $\boldsymbol{q}_2$, and $\boldsymbol{q}_3$, one simply solves Equation (6.6) for $\boldsymbol{g}$ subject to $\max\{\boldsymbol{g}\} \leq$ the scanner's maximum gradient amplitude, $\boldsymbol{D}\boldsymbol{g} \leq$ the maximum slew rate, $\mathrm{sum}\{\boldsymbol{g}\} = 0$ to have the trajectory end at the k-space origin, and a constraint forcing the cumulative running sum of the entries in $\boldsymbol{g}$ to periodically go to 0 to reduce through-plane dephasing. Here, $\boldsymbol{D}$ is a matrix that computes the difference of neighboring entries in a vector. Of course, the difficulty with this approach is making sure a solution $\boldsymbol{g}$ satisfies all the previously mentioned constraints.

Instead of using a point for $\boldsymbol{e}_j$, one could optimize the z-gradient for brain images by using a brain object for $\boldsymbol{e}_j$. Furthermore, since each slice in a 3 simultaneous slice acquisition has a different size as shown in Figure 4.22 for example, each of these different slices could be used for the separate positions z_1, z_2, and z_3. Equation (6.6) becomes

$$-i2\pi\gamma\Delta t \begin{bmatrix} z_1\boldsymbol{L} \\ z_2\boldsymbol{L} \\ z_3\boldsymbol{L} \end{bmatrix} \boldsymbol{g} = \begin{bmatrix} \log(\mathrm{diag}\{\boldsymbol{Q}\boldsymbol{x}_1\}^{-1}\boldsymbol{Q}\boldsymbol{q}_1) \\ \log(\mathrm{diag}\{\boldsymbol{Q}\boldsymbol{x}_2\}^{-1}\boldsymbol{Q}\boldsymbol{q}_2) \\ \log(\mathrm{diag}\{\boldsymbol{Q}\boldsymbol{x}_3\}^{-1}\boldsymbol{Q}\boldsymbol{q}_3) \end{bmatrix}, \tag{6.7}$$

where slices 7, 20, and 33 in Figure 4.22 are used for $\boldsymbol{x}_1$, $\boldsymbol{x}_2$, and $\boldsymbol{x}_3$, respectively.

6.5.2 Alternative Regularization Method in SENSE Reconstruction

The alternative regularization method for SENSE reconstruction of SMS data given by Equation (4.2) showed promise with blipped spiral SMS imaging. It would be interesting and informative to perform this type of SENSE reconstruction on the concentric ring fMRI data used in Chapter 5 and compare not only the image quality, but the activation performance, image artifact behavior, and SNR with that for the other SMS reconstruction methods. In addition, it would be useful to perform a PSF analysis similar to what was done in Section 2.2.2 to determine a proper value for the regularization parameter. This would verify claims that the subjectively better appearance of the resulting images is not a result of oversmoothing.

6.5.3 GRABSMACC

Buehrer et al. [78] proposed a coil compression method that uses Principle Component Analysis on coil sensitivities to compute compression matrices that reduce reconstructed image noise. Their method requires the formation of coil sensitivities for superimposed voxels, which is easily done for undersampled Cartesian trajectories. However, with a concentric ring and blipped z-gradient readout, the aliasing pattern is not a trivial shift in some direction, but a blur in many directions. This makes it impractical to use their method to reduce image noise in our case. On the other hand, GRABSMACC can be easily used with Cartesian SMS fMRI. Future work may involve comparing the activation performance of GRABSMACC with other noise reducing compression methods, as well as investigating the compression performance of GRABSMACC using different numbers of simultaneous slices.

The general reason why GRABSMACC performs better at greater coil reduction

factors is because the problem has been set up to allow the SVD to tailor the compression matrices for the individual slices instead of the combined, slice-aliased data. In addition to optimizing the compression for slices, tailoring the compression for coil geometry could also be done to potentially further increase the performance. One possible way is to compress groups of coils which are closest together in physical location so that each virtual coil is a representation of a different physical area. For example, using the 32-channel sensitivities shown in Figure 4.15, compression matrices for each set of 4 consecutive coils can be computed since each of these sets is closely related in profile. This would result in 8 virtual coils sensitivities each representing a different area in the volume. It remains as future work as to whether this approach would outperform an SVD on all 32 coils at once.

GRABSMACC clearly benefited from the use of non-SMS calibration data for compression matrix computation. With the way SENSE reconstruction is formulated in Equation (4.1), it is impossible to use distinct compression matrices for each of the separated slices in SENSE. However, a slight alteration to the k-space trajectory can potentially allow this to happen.

At the end of Section 4.3, an alternative reconstruction method was proposed that uses a one-dimensional inverse Fourier transform in the through-plane direction to separate slices. This one-dimensional transform was performed after either in-plane SENSE or in-plane GRAPPA. However, if it was possible to perform the inverse Fourier transform *before* SENSE, distinct compression matrices computed from non-SMS data could be used.

For example, if the one-dimensional inverse transform is performed first, the SMS k-space data would be separated into a hybrid (k_x, k_y, z) space. Each k_x-k_y platter in this hybrid space is for a distinct z-location matching the z-locations of the non-SMS calibration data used to compute coil sensitivities. Therefore, each k_x-k_y platter in this hybrid (k_x, k_y, z) space can be compressed using a distinct compression matrix

computed from the corresponding non-SMS slice. Once the data is compressed, in-plane SENSE is performed on the (k_x, k_y, z) space to produce the final images.

The reason why the inverse Fourier transform could not be performed first with the blipped concentric ring trajectory in Figure 4.4 created by the waveforms depicted in Figure 4.5 is because each k_x-k_y platter has a different set of undersampled rings. This happens because the radius of the rings decreases with each z-gradient blip. Therefore, the solution is to create a similar blipped concentric ring trajectory that has the same set of undersampled rings in each k_x-k_y platter. This is done for a 3 simultaneous slice acquisition by tracing out 3 rings with the same radius, transitioning past the two consecutively smaller ring positions, and tracing out another 3 rings with the same radius, and so on. This creates a factor of 3 undersampling in each k_x-k_y platter with the same set of ring locations for each platter.

One drawback of this approach, however, is that the timing of the concentric ring acquisitions for all k_x-k_y platters will not match up exactly with the timing of the non-SMS scan used to compute field maps or sensitivity maps. For a 3 simultaneous slice acquisition, one of the platters will match up, but the other 2 will not. However, the timing differences may be minimal enough so that reconstruction quality is not affected.

The alternative to this modified-trajectory approach is of course to reformulate Equation (4.1) into something that allows the use of distinct compression matrices computed from non-SMS data. However, one needs to be careful not to create a matrix equation with dimensions so large that the computational speed benefit of coil compression is negated by the larger problem.

6.5.4 Further Comparisons with Conventional Non-SMS fMRI

Overall, SMS imaging is a promising method to accelerate fMRI since a minimum bound on the TE is required for adequate contrast in fMRI. However, as with any method, the acceleration comes at a price; slices can easily be corrupted in the slice separation process, transferring or corrupting areas of activation. There is a clear temporal resolution benefit in SMS fMRI, but this advantage needs to be carefully considered against slice leakage and SNR issues in fMRI. Before widespread adoption occurs, detailed comparisons with conventional, non-accelerated fMRI need to be performed to determine which applications benefit from SMS imaging and which do not. If, for example, it is desired to measure lag times of the hemodynamic response function in different areas of the brain, SMS is helpful since conventional non-accelerated fMRI may not be able to provide a high enough temporal resolution for a given spatial coverage. On the other hand, if the objective is just to map out activation using simple block paradigm task scans on healthy volunteers, there may not be much benefit when using SMS imaging over conventional imaging. As with any advanced tool, it is essential that SMS imaging is used in the proper application in order to realize its benefits.

BIBLIOGRAPHY

[1] S. Ogawa, T. M. Lee, A. R. Kay, and D. W. Tank. Brain magnetic resonance imaging with contrast dependent on blood oxygenation. *Proc. Natl. Acad. Sci. U. S. A.*, 87(24):9868–9872, 1990.

[2] P. T. Fox and M. E. Raichle. Focal physiological uncoupling of cerebral blood flow and oxidative metabolism during somatosensory stimulation in human subjects. *Proc. Natl. Acad. Sci. U. S. A.*, 83(4):1140–1144, 1986.

[3] P. T. Fox, M. E. Raichle, M. A. Mintun, and C. Dence. Nonoxidative glucose consumption during focal physiologic neural activity. *Science*, 241(4864):462–464, 1988.

[4] P. A. Bandettini, E. C. Wong, R. S. Hinks, R. S. Tikofsky, and J. S. Hyde. Time course EPI of human brain function during task activation. *Magn. Reson. Med.*, 25(2):390–397, 1992.

[5] S. Ogawa, D. W. Tank, R. Menon, J. M. Ellermann, S. G. Kim, H. Merkle, and K. Ugurbil. Intrinsic signal changes accompanying sensory stimulation: functional brain mapping with magnetic resonance imaging. *Proc. Natl. Acad. Sci. U. S. A.*, 89(13):5951–5955, 1992.

[6] J. Frahm, H. Bruhn, K. D. Merboldt, and W. Hänicke. Dynamic MR imaging of human brain oxygenation during rest and photic stimulation. *J. Magn. Reson. Imaging*, 2(5):501–505, 1992.

[7] K. K. Kwong, J. W. Belliveau, D. A. Chesler, I. E. Goldberg, R. M. Weisskoff, B. P. Poncelet, D. N. Kennedy, B. E. Hoppel, M. S. Cohen, and R. Turner. Dynamic magnetic resonance imaging of human brain activity during primary sensory stimulation. *Proc. Natl. Acad. Sci. U. S. A.*, 89(12):5675–5679, 1992.

[8] P. Jezzard, D. LeBihan, C. Cuenod, L. Pannier, A. Prinster, and R. Turner. An investigation of the contribution of physiological noise in human functional MRI studies at 1.5 Tesla and 4 Tesla. In *Proceedings of the Annual Meeting of ISMRM*, p. 1392. New York, US, 1993.

[9] R. M. Weisskoff, J. Baker, J. Belliveau, T. L. David, K. K. Kwong, M. S. Cohen, and B. R. Rosen. Power spectrum analysis of functionally-weighted MR data: What's in the noise? In *Proceedings of the Annual Meeting of ISMRM*, p. 7. New York, US, 1993.

[10] D. C. Noll and W. Schneider. Respiration artifacts in functional brain imaging: sources of signal variation and compensation strategies. In *Proceedings of the Annual Meeting of ISMRM*, p. 647. San Francisco, US, 1994.

[11] D. C. Noll and W. Schneider. Theory, simulation, and compensation of physiological motion artifacts in functional MRI. In *Proc. IEEE Int. Conf. Image Process.*, volume 3, pp. 40–44. IEEE Comput. Soc. Press, 1994.

[12] X. Hu and S. G. Kim. Reduction of signal fluctuation in functional MRI using navigator echoes. *Magn. Reson. Med.*, 31(5):495–503, 1994.

[13] X. Hu, T. H. Le, T. Parrish, and P. Erhard. Retrospective estimation and correction of physiological fluctuation in functional MRI. *Magn. Reson. Med.*, 34(2):201–212, 1995.

[14] B. Biswal, E. A. DeYoe, and J. S. Hyde. Reduction of physiological fluctuations in fMRI using digital filters. *Magn. Reson. Med.*, 35(1):107–113, 1996.

[15] B. Wowk, M. C. McIntyre, and J. K. Saunders. k-space detection and correction of physiological artifacts in fMRI. *Magn. Reson. Med.*, 38(6):1029–1034, 1997.

[16] G. H. Glover, T. Q. Li, and D. Ress. Image-based method for retrospective correction of physiological motion effects in fMRI: RETROICOR. *Magn. Reson. Med.*, 44(1):162–167, 2000.

[17] G. H. Glover and S. Lai. Self-navigated spiral fMRI: interleaved versus single-shot. *Magn. Reson. Med.*, 39(3):361–368, 1998.

[18] R. M. Birn, M. A. Smith, T. B. Jones, and P. A. Bandettini. The respiration response function: the temporal dynamics of fMRI signal fluctuations related to changes in respiration. *Neuroimage*, 40(2):644–654, 2008.

[19] C. Chang, J. P. Cunningham, and G. H. Glover. Influence of heart rate on the BOLD signal: the cardiac response function. *Neuroimage*, 44(3):857–869, 2009.

[20] D. A. Feinberg and E. Yacoub. The rapid development of high speed, resolution and precision in fMRI. *Neuroimage*, 62(2):720–725, 2012.

[21] K. P. Pruessmann, M. Weiger, M. B. Scheidegger, and P. Boesiger. SENSE: sensitivity encoding for fast MRI. *Magn. Reson. Med.*, 42(5):952–962, 1999.

[22] M. A. Griswold, P. M. Jakob, R. M. Heidemann, M. Nittka, V. Jellus, J. Wang, B. Kiefer, and A. Haase. Generalized autocalibrating partially parallel acquisitions (GRAPPA). *Magn. Reson. Med.*, 47(6):1202–1210, 2002.

[23] M. Lustig and J. M. Pauly. SPIRiT: iterative self-consistent parallel imaging reconstruction from arbitrary k-space. *Magn. Reson. Med.*, 64(2):457–471, 2010.

[24] P. Mansfield, A. M. Howseman, and R. J. Ordidge. Volumar imaging using NMR spin echoes: echo-volumar imaging (EVI) at 0.1 T. *J. Phys. E.*, 22(5):324–330, 1989.

[25] A. W. Song, E. C. Wong, and J. S. Hyde. Echo-volume imaging. *Magn. Reson. Med.*, 32(5):668–671, 1994.

[26] P. Mansfield, R. Coxon, and J. Hykin. Echo-volumar imaging (EVI) of the brain at 3.0 T: first normal volunteer and functional imaging results. *J. Comput. Assist. Tomogr.*, 19(6):847–852, 1995.

[27] D. Hoult. The solution of the bloch equations in the presence of a varying B1 field–an approach to selective pulse analysis. *J. Magn. Reson.*, 35(1):69–86, 1979.

[28] W. S. Hinshaw and A. H. Lent. An introduction to NMR imaging: from the Bloch equation to the imaging equation. *Proc. IEEE*, 71(3):338–350, 1983.

[29] S. P. Souza, J. Szumowski, C. L. Dumoulin, D. P. Plewes, and G. Glover. SIMA: simultaneous multislice acquisition of MR images by Hadamard-encoded excitation. *J. Comput. Assist. Tomogr.*, 12(6):1026–1030, 1988.

[30] G. H. Glover and C. Chang. Hadamard-encoded sub-slice fMRI for reduced signal dropout. *Magn. Reson. Imaging*, 30(1):1–8, 2012.

[31] J. B. Weaver. Simultaneous multislice acquisition of MR images. *Magn. Reson. Med.*, 8(3):275–284, 1988.

[32] G. H. Glover. Phase-offset multiplanar (POMP) volume imaging: a new technique. *J. Magn. Reson. Imaging*, 1(4):457–461, 1991.

[33] D. C. Noll, S. J. Peltier, and F. E. Boada. Simultaneous multislice acquisition using rosette trajectories (SMART): a new imaging method for functional MRI. *Magn. Reson. Med.*, 39(5):709–716, 1998.

[34] D. A. Feinberg, T. G. Reese, and V. J. Wedeen. Simultaneous echo refocusing in EPI. *Magn. Reson. Med.*, 48(1):1–5, 2002.

[35] J. A. Fessler and B. P. Sutton. Nonuniform fast Fourier transforms using min-max interpolation. *IEEE Trans. Signal Process.*, 51(2):560–574, 2003.

[36] B. P. Sutton, D. C. Noll, and J. A. Fessler. Fast, iterative image reconstruction for MRI in the presence of field inhomogeneities. *IEEE Trans. Med. Imaging*, 22(2):178–188, 2003.

[37] D. J. Larkman, J. V. Hajnal, A. H. Herlihy, G. A. Coutts, I. R. Young, and G. Ehnholm. Use of multicoil arrays for separation of signal from multiple slices simultaneously excited. *J. Magn. Reson. Imaging*, 13(2):313–317, 2001.

[38] F. A. Breuer, M. Blaimer, R. M. Heidemann, M. F. Mueller, M. A. Griswold, and P. M. Jakob. Controlled aliasing in parallel imaging results in higher acceleration (CAIPIRINHA) for multi-slice imaging. *Magn. Reson. Med.*, 53(3):684–691, 2005.

[39] R. G. Nunes, J. V. Hajnal, X. Golay, and D. J. Larkman. Simultaneous slice excitation and reconstruction for single shot EPI. In *Proceedings of the Annual Meeting of ISMRM*, p. 293. Seattle, US, 2006.

[40] K. Setsompop, B. A. Gagoski, J. R. Polimeni, T. Witzel, V. J. Wedeen, and L. L. Wald. Blipped-controlled aliasing in parallel imaging for simultaneous multislice echo planar imaging with reduced g-factor penalty. *Magn. Reson. Med.*, 67(5):1210–1224, 2012.

[41] B. Zahneisen, B. A. Poser, T. Ernst, and V. A. Stenger. Three-dimensional Fourier encoding of simultaneously excited slices: generalized acquisition and reconstruction framework. *Magn. Reson. Med.*, 71(6):2071–2081, 2014.

[42] M. R. Hestenes and E. Stiefel. Methods of conjugate gradients for solving linear systems. *J. Res. Natl. Bur. Stand.*, 49(6):409–436, 1952.

[43] J. A. Fessler. Image reconstruction toolbox. Accessed 2013-10-22.
URL http://web.eecs.umich.edu/~fessler/code/index.html

[44] K. Sekihara, S. Matsui, and H. Kohno. NMR imaging for magnets with large nonuniformities. *IEEE Trans. Med. Imaging*, 4(4):193–199, 1985.

[45] M. Uecker, P. Lai, M. J. Murphy, P. Virtue, M. Elad, J. M. Pauly, S. S. Vasanawala, and M. Lustig. ESPIRiT–an eigenvalue approach to autocalibrating parallel MRI: where SENSE meets GRAPPA. *Magn. Reson. Med.*, 71(3):990–1001, 2014.

[46] S. Moeller, E. Yacoub, C. A. Olman, E. Auerbach, J. Strupp, N. Harel, and K. Uurbil. Multiband multislice GE-EPI at 7 tesla, with 16-fold acceleration using partial parallel imaging with application to high spatial and temporal whole-brain fMRI. *Magn. Reson. Med.*, 63(5):1144–1153, 2010.

[47] M. Blaimer, F. A. Breuer, N. Seiberlich, M. F. Mueller, R. M. Heidemann, V. Jellus, G. Wiggins, L. L. Wald, M. A. Griswold, and P. M. Jakob. Accelerated volumetric MRI with a SENSE/GRAPPA combination. *J. Magn. Reson. Imaging*, 24(2):444–450, 2006.

[48] B. Zahneisen, B. A. Poser, T. Ernst, and V. A. Stenger. Simultaneous multi-slice fMRI using spiral trajectories. *Neuroimage*, 92:8–18, 2014.

[49] G. H. Glover. Spiral imaging in fMRI. *Neuroimage*, 62(2):706–712, 2012.

[50] P. Börnert, B. Aldefeld, and H. Eggers. Reversed spiral MR imaging. *Magn. Reson. Med.*, 44(3):479–484, 2000.

[51] Y. Yang, G. H. Glover, P. van Gelderen, A. C. Patel, V. S. Mattay, J. A. Frank, and J. H. Duyn. A comparison of fast MR scan techniques for cerebral activation studies at 1.5 Tesla. *Magn. Reson. Med.*, 39(1):61–67, 1998.

[52] A. Chu, J.-F. Nielsen, S. J. Peltier, and D. C. Noll. Increased SNR and activation in Hadamard-encoded fMRI through physiological noise removal and phase correction. In *Proceedings of the Annual Meeting of ISMRM*, p. 3634. Montreal, CA, 2011.

[53] A. Chu, J.-F. Nielsen, and D. C. Noll. Increased temporal resolution in fMRI using Hadamard-encoding with phase correction and physiological noise removal. In *Proceedings of the Annual Meeting of ISMRM*, p. 2858. Melbourne, AU, 2012.

[54] G. Kruger and G. H. Glover. Physiological noise in oxygenation-sensitive magnetic resonance imaging. *Magn. Reson. Med.*, 46(4):631–637, 2001.

[55] J. Pfeuffer, P.-F. Van de Moortele, K. Ugurbil, X. Hu, and G. H. Glover. Correction of physiologically induced global off-resonance effects in dynamic echo-planar and spiral functional imaging. *Magn. Reson. Med.*, 47(2):344–353, 2002.

[56] T. Parks and J. McClellan. Chebyshev approximation for nonrecursive digital filters with linear phase. *IEEE Trans. Circuit Theory*, 19(2):189–194, 1972.

[57] R. R. Ernst and W. A. Anderson. Application of Fourier transform spectroscopy to magnetic resonance. *Rev. Sci. Instrum.*, 37(1):93–102, 1966.

[58] K. J. Friston, A. P. Holmes, J. B. Poline, P. J. Grasby, S. C. Williams, R. S. Frackowiak, and R. Turner. Analysis of fMRI time-series revisited. *Neuroimage*, 2(1):45–53, 1995.

[59] K. J. Worsley and K. J. Friston. Analysis of fMRI time-series revisited–again. *Neuroimage*, 2(3):173–181, 1995.

[60] C. R. Genovese, D. C. Noll, and W. F. Eddy. Estimating test-retest reliability in functional MR imaging I: statistical methodology. *Magn. Reson. Med.*, 38(3):497–507, 1997.

[61] D. C. Noll, C. R. Genovese, L. E. Nystrom, A. L. Vazquez, S. D. Forman, W. F. Eddy, and J. D. Cohen. Estimating test-retest reliability in functional MR imaging II: application to motor and cognitive activation studies. *Magn. Reson. Med.*, 38(3):508–517, 1997.

[62] Fmincon - MathWorks. Accessed 2015-12-24.
URL http://www.mathworks.com/help/optim/ug/fmincon.html

[63] J. Nocedal and S. Wright. *Numerical optimization*. Springer Series in Operations Research and Financial Engineering. Springer-Verlag New York, 2nd edition, 2006.

[64] J. W. Tukey. Comparing individual means in the analysis of variance. *Biometrics*, 5(2):99–114, 1949.

[65] D. C. Noll, J. D. Cohen, C. H. Meyer, and W. Schneider. Spiral k-space MR imaging of cortical activation. *J. Magn. Reson. Imaging*, 5(1):49–56, 1995.

[66] P.-F. Van de Moortele, J. Pfeuffer, G. H. Glover, K. Ugurbil, and X. Hu. Respiration-induced B0 fluctuations and their spatial distribution in the human brain at 7 Tesla. *Magn. Reson. Med.*, 47(5):888–895, 2002.

[67] A. Chu and D. C. Noll. Simultaneous multislice spiral imaging using z-gradient modulation and parallel receive coils. In *Proceedings of the Annual Meeting of ISMRM*, p. 3317. Salt Lake City, US, 2013.

[68] A. Chu and D. C. Noll. GRAPPA-based simultaneous multislice reconstruction using concentric ring k-space. In *Proceedings of the Annual Meeting of ISMRM*, p. 1540. Milan, IT, 2014.

[69] A. Chu and D. C. Noll. Coil compression in simultaneous multislice functional MRI with concentric ring slice-GRAPPA and SENSE. *Magn. Reson. Med.*, 2015. doi:10.1002/mrm.26032.

[70] Y. Yang, H. Gu, W. Zhan, S. Xu, D. A. Silbersweig, and E. Stern. Simultaneous perfusion and BOLD imaging using reverse spiral scanning at 3T: characterization of functional contrast and susceptibility artifacts. *Magn. Reson. Med.*, 48(2):278–289, 2002.

[71] J. G. Pipe and N. R. Zwart. Spiral trajectory design: a flexible numerical algorithm and base analytical equations. *Magn. Reson. Med.*, 71(1):278–285, 2014.

[72] R. M. Heidemann, M. A. Griswold, N. Seiberlich, G. Kruger, S. A. R. Kannengiesser, B. Kiefer, G. Wiggins, L. L. Wald, and P. M. Jakob. Direct parallel image reconstructions for spiral trajectories using GRAPPA. *Magn. Reson. Med.*, 56(2):317–326, 2006.

[73] S. F. Cauley, J. R. Polimeni, H. Bhat, L. L. Wald, and K. Setsompop. Interslice leakage artifact reduction technique for simultaneous multislice acquisitions. *Magn. Reson. Med.*, 72(1):93–102, 2014.

[74] T. Zhang, J. M. Pauly, S. S. Vasanawala, and M. Lustig. Coil compression for accelerated imaging with Cartesian sampling. *Magn. Reson. Med.*, 69(2):571–582, 2013.

[75] A. Chu and D. C. Noll. The effects of coil compression on simultaneous multislice and conventional fMRI. In *Proceedings of the Annual Meeting of ISMRM*, p. 2062. Toronto, CA, 2015.

[76] S. B. King, S. M. Varosi, F. Huang, and G. R. Duensing. The MRI eigencoil: 2N-channel SNR with N-receivers. In *Proceedings of the Annual Meeting of ISMRM*, p. 712. Toronto, CA, 2003.

[77] S. B. King, S. M. Varosi, and G. R. Duensing. Optimum SNR data compression in hardware using an eigencoil array. *Magn. Reson. Med.*, 63(5):1346–1356, 2010.

[78] M. Buehrer, K. P. Pruessmann, P. Boesiger, and S. Kozerke. Array compression for MRI with large coil arrays. *Magn. Reson. Med.*, 57(6):1131–1139, 2007.

[79] F. Huang, S. Vijayakumar, Y. Li, S. Hertel, and G. R. Duensing. A software channel compression technique for faster reconstruction with many channels. *Magn. Reson. Imaging*, 26(1):133–141, 2008.

[80] S. F. Cauley, B. Bilgic, J. R. Polimeni, H. Bhat, L. L. Wald, and K. Setsompop. A general hierarchical mapping framework (HMF) for coil compression. In *Proceedings of the Annual Meeting of ISMRM*, p. 4393. Milan, IT, 2014.

[81] P. J. Beatty, S. Chang, J. H. Holmes, K. Wang, A. C. S. Brau, S. B. Reeder, and J. H. Brittain. Design of k-space channel combination kernels and integration with parallel imaging. *Magn. Reson. Med.*, 71(6):2139–2154, 2014.

[82] M. A. Lindquist, J. Meng Loh, L. Y. Atlas, and T. D. Wager. Modeling the hemodynamic response function in fMRI: efficiency, bias and mis-modeling. *Neuroimage*, 45(1 Suppl):S187–S198, 2009.

[83] J. A. Fessler and W. L. Rogers. Spatial resolution properties of penalized-likelihood image reconstruction: space-invariant tomographs. *IEEE Trans. Image Process.*, 5(9):1346–1358, 1996.

[84] P. M. Robson, A. K. Grant, A. J. Madhuranthakam, R. Lattanzi, D. K. Sodickson, and C. A. McKenzie. Comprehensive quantification of signal-to-noise ratio and g-factor for image-based and k-space-based parallel imaging reconstructions. *Magn. Reson. Med.*, 60(4):895–907, 2008.

[85] C. W. Dunnett. A multiple comparison procedure for comparing several treatments with a control. *J. Am. Stat. Assoc.*, 50(272):1096–1121, 1955.

[86] J. R. Polimeni, H. Bhat, T. Witzel, T. Benner, T. Feiweier, S. J. Inati, V. Renvall, K. Heberlein, and L. L. Wald. Reducing sensitivity losses due to respiration and motion in accelerated echo planar imaging by reordering the autocalibration data acquisition. *Magn. Reson. Med.*, 2015. doi:10.1002/mrm.25628.

[87] D. C. Noll, C. H. Meyer, J. M. Pauly, D. G. Nishimura, and A. Macovski. A homogeneity correction method for magnetic resonance imaging with time-varying gradients. *IEEE Trans. Med. Imaging*, 10(4):629–637, 1991.